High Efficiency Pulse Motor Drive for Robotic Propulsion
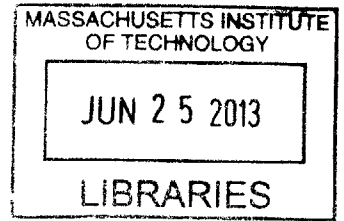
by

Zhen Sun

Bachelor of Mechanical Engineering, University of Minnesota, twin
cities (2011)

Submitted to the Department of Mechanical Engineering
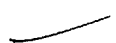in partial fulfillment of the requirements for the degree of

Master of Science in Mechanical Engineering

at the

MASSACHUSETTS INSTITUTE OF TECHNOLOGY

June 2013

Author ....
Department of Mechanical Engineering
May 10, 2013

Certified by ....
David L. Trumper
Professor of Mechanical Engineering
Thesis Supervisor

Accepted by ....
David E. Hardt
Department Committee on Graduate Students

High Efficiency Pulse Motor Drive for Robotic Propulsion

by

Zhen Sun

Abstract

The goal of this research is to improve the power efficiency of robotic locomotion through the use of series elastic actuation, with a focus on swimming motion. To achieve high efficiency, electromechanical drives need to be actuated at high speed and low torque. However, in many robots, the drives are actuated in a low speed and high torque mode, resulting in lower efficiency. Implementing gear trains is one option to rise the input speed and lower the input torque. However gear trains have their own loss which are particularly severe at high gear ratios, and are not back drivable in some cases.

In this thesis, we envision and design a new pulse drive type of series elastic electromechanical actuators that seeks to break such tradeoffs and improve overall robotic propulsion drive efficiency. An energy storage element, such as a spring, is installed between the EM actuator and the load. In the fast actuation phase, a pulse displacement/torque trajectory is applied to the actuator shaft so that the spring is rapidly charged with potential energy. In the slow driving phase, the actuator shaft is locked by a low power mechanical latch and the spring slowly transfers energy into the load. We analytically determine that the most efficient pulse condition is reached when the frequency of the pulse trajectory is close to the natural frequency of the actuator inertia-spring system.

Our first low power hardware demonstration without the gearbox transmission shows that the pulse drive achieves an energy efficiency of 80% compared to an efficiency of 50% achieved in the conventional direct drive where an electromechanical actuator is driving a viscous load equal to its own motor constant. Another low power hardware demonstration using gearmotors at two loads, whose impedances are 10 times and 20 times as high as the driver motor constant, shows that the pulse drive using a motor with a one-stage gearbox transmission achieves an efficiency of 50%, which are approximately 20% higher than the conventional drive with either a one-stage or a two-stage gearbox transmission. An analytical study on the influence of motor size shows that the efficiency gain of the pulse drive becomes larger at smaller motors and that the best option for the pulse drive is to use a motor with a one-stage gearbox. In a third hardware demonstration, we scale up the power level to match that of a small

robotic fish, and use a real viscous load. By using the same brushless motor with a one-stage gearbox, we achieve a pulse drive efficiency of 70% compared to 15% in the conventional gear drive. Some potential targets are robots with cyclical propulsions and high impedance load, e.g., tail actuation in fish-like swimming robots, wing actuation in flying robots and crawling and other motions in snake-like robots.

Thesis Supervisor: David L. Trumper
Title: Professor of Mechanical Engineering

Acknowledgments

First I would like to thank my advisor, Professor David Trumper, for patiently guiding me through the project and providing tremendous support. Among many great values that I learn from him, the most precious one is the three-dimensional thinking process. He always encourage me to think broadly about design possibilities, think deeply regarding the fundamental principles beneath observations and think thoroughly over each step towards a particular goal. I'm deeply grateful to his mentoring as it will benefit all my life. I want to thank Professor David Barrett at Franklin W. Olin College of Engineering for inspiring the idea of this great project and giving me many supports along the way. I would like to express my special gratitude to Laura Zaganjori for taking care of every logistic details. Laura's dedication has created a comfortable environment for us to focus on research and study. I can't imagine what things will look like without her.

I also want to give credits to my wonderful labmates. Mohammad Imani Nejad provides me a lot of information on motor selections which is a big part of this project and gives me many tips on machining. And it is fun to teach him Chinese from time to time. Darya Amin-Shahidi is a wonderful teacher in the Mechatronics class from whom I gained a lot of knowledge about mechatronics system integration. In the lab, he is always there answering my questions about research and helping me solve problems. Darya also has a great sense of humor that he brings a lot of laughter to the lab. Jun Young Yoon gives me a lot of useful advice at different stages of my project. He also helps me adjust to the lab environment at the beginning of my research. I also enjoy the rivalry of playing Ping-Pong with him although I can never beat him. I really enjoy working with Roberto Meléndez on the National Instrument digital control lab project. He is also very enthusiastic in organizing lab events such as Ping-Pong tournament and birthday celebrations. His passion bonds us together as a family. I want to say special thanks to Lei Zhou, who secretly prepared a birthday card for me with greetings from all labmates, which warmed my heart in the cold winter. Minkyun gives me many useful suggestions on the design details of my final

Contents

List of Figures

11

13

List of Tables

Chapter 1

Introduction

1.1 Project Motivations

This project is motivated by the need to improve the energy efficiency of robotic fish swimming propulsion. Professor David Barrett at Franklin W. Olin College of Engineering with his team has been designing and building different sizes of robotic fish to mimic the motion of marine animals such as tuna and whale [1] [11]. A photo of one of his robotic tunas is shown in Figure 1-1. The long term goal of their robotic fish project is to facilitate the study of ocean ecology and marine life in a much less invasive manner. One of the biggest challenges they are facing is to improve the overall propulsion efficiency. With the current design of using high reduction gearmotor and tendon-pulley transmission, the resulting energy efficiency is around 10%. As the robotic fish is powered independently underwater by a battery, such poor efficiency can significantly limit the operating duration and travel range, thus compromising the benefit it can bring. After several meetings with Professor Barrett and many productive discussions, we envision and design a new pulse drive type of electromechanical series elastic actuator that has the potential to significantly improve the propulsion efficiency. Figure 1-2 shows a conceptual drawing of a robotic fish integrated with such a pulse drive in the tail. This conceptual sketch is not a complete design, but is a vision of integration in the near future. The cyclical tail motions are driven by a number of the pulse drives associated with pivoting joints
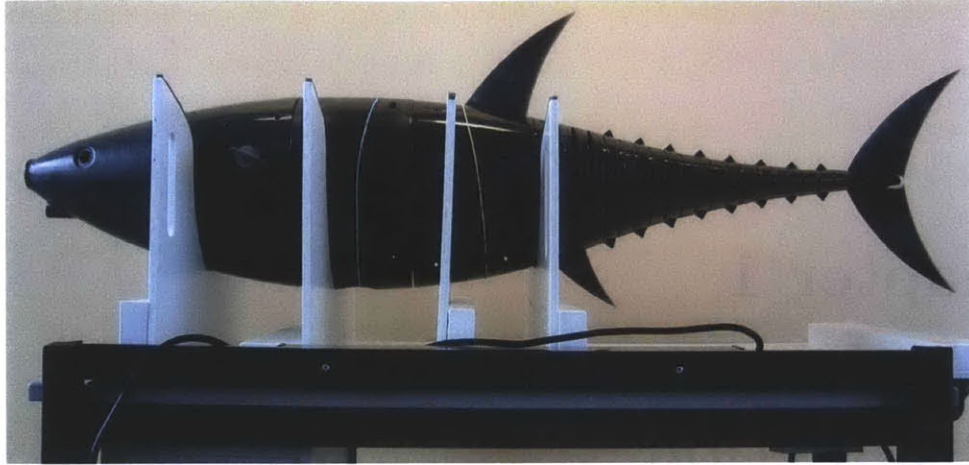
Figure 1-1: Photo of a robotic tuna fish developed by Professor David Barrett at Franklin W. Olin College of Engineering.
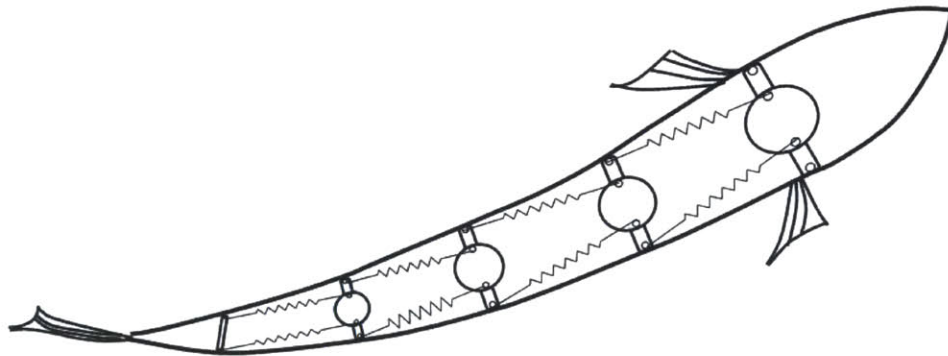
Figure 1-2: Conceptual drawing of a robotic fish integrated with the pulse drive in the tail.

in the tail. At each joint, a pair of springs is connected to a motor. The motor will rapidly rotate, storing energy by pulling one of the two springs into tension. A half cycle later, the motor rapidly rotates by π radians, pulling the opposite spring into tension. The spring thus exerts a moment on the joint of the tail, thereby driving the oscillatory swimming motion.

1.2 Key Results

In this thesis, we have designed and built a pulse drive hardware demonstration with the load power level (1 W), similar to a that in a small robotic fish. As shown in Figure 1-3, the actuator, the spring and the load are connected in series and the motion is strictly rotational. The driving actuator is a Maxon EC 22 100 W brushless motor with a one-stage gearbox of reduction ratio 4.4 [5]. It is driven by a linear servo amplifier in torque mode. A coil spring is stretched between the motor and the load encoder as the energy storage element. A glass syringe with glycerin between the piston and barrel is used to create a viscous damping load. In each work cycle, a pulse trajectory is first applied to the motor shaft so that the spring is rapidly stored with potential energy. Then the motor shaft is held fixed and the spring transfers the energy into the viscous load at a slower time scale. We study the energy efficiency of this type of pulse drive by maneuvering the load to several amplitudes at a cyclical frequency of 1 Hz, and compare the efficiency results to the drive with a stiff connection which we refer as the conventional drive. As shown in Figure 1-4, the efficiency of the pulse drive can be significantly better than the conventional gear drive using the same actuator: 70% compared to 15%. Such efficiency gain comes from the motor in the pulse drive operating in a high speed and low torque mode compared to the low speed and high torque mode of the conventional drive, such that the resistive heat loss in the motor coil is reduced. The result demonstrates that the pulse drive can operate more efficiently than the conventional drive as a stand-alone unit. We foresee that such pulse drive principles can be applied to a wide range of robotic propulsion drives to improve efficiency.

1.3 Thesis Structure Overview

The rest of this thesis is laid out as follows.

The next section in this chapter briefly reviews the prior work in series elastic actuator design.
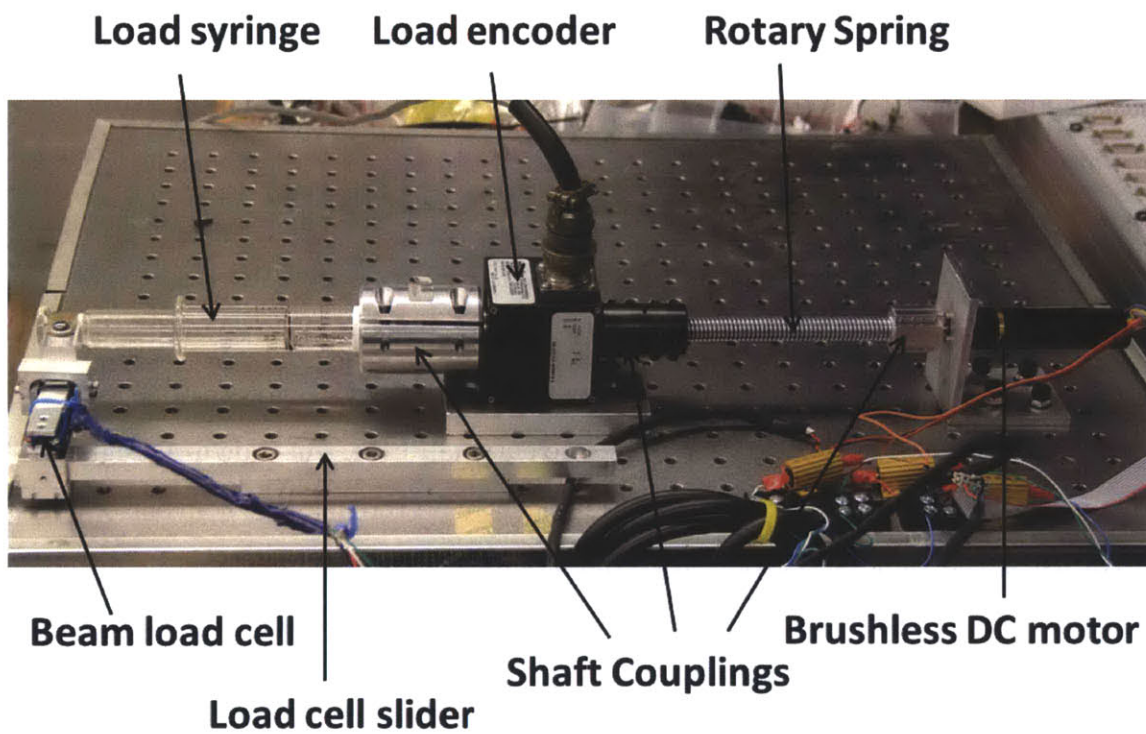
Figure 1-3: Picture of the pulse drive hardware demonstration simulating the 1 W power level of a small robotic fish.
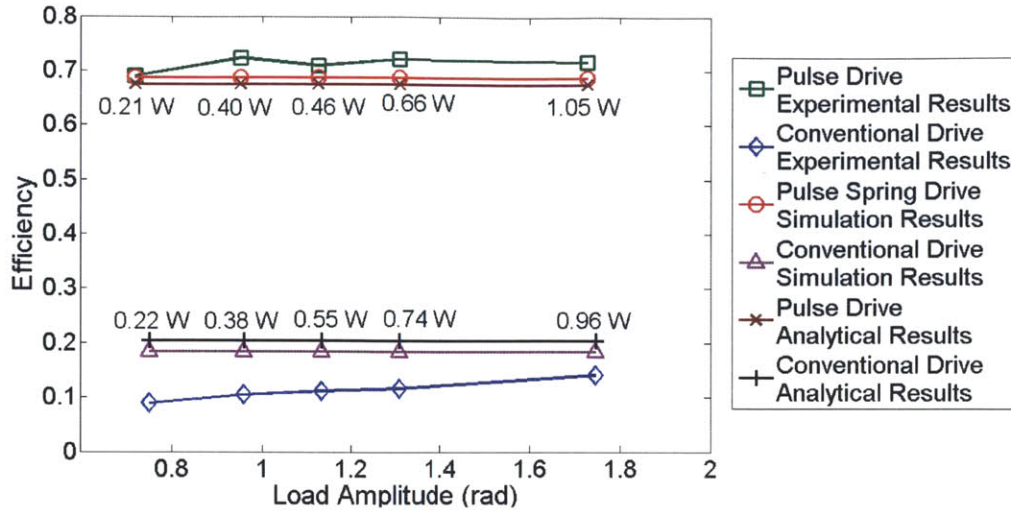
Figure 1-4: Plots of energy efficiency results for both the pulse gear drive and the conventional gear drive in experiment of Figure 1-3. The pulse gear drive achieves approximately 70% experimental energy efficiency while the measured energy efficiency of the conventional drive ranges from 10% to 15%.

Chapter 2 lays out the fundamental tradeoffs for the pulse drive. The energy efficiency of storing energy in a massless spring, in a pure mass, and a spring-mass system are discussed in detail.

Chapter 3 models the pulse drive system and derives analytical efficiency expressions. A simple conventional drive model is also constructed for efficiency comparison. The analytical results are then compared to simulation results. The effects of adding gearbox transmissions, adding a crank-shaft transmission and changing the pulse trajectory profiles are also discussed.

Chapter 4 shows a hardware demonstration for the pulse drive without any transmission. The energy efficiency is measured and compared to the efficiency of the conventional direct drive configuration.

Chapter 5 shows a hardware demonstration for the pulse drive with a planetary gearbox transmission. The energy efficiency is measured and compared to the efficiency of the conventional gear drive configuration. Gearbox efficiency is also studied experimentally.

Chapter 6 studies the effect of the motor size on pulse drive efficiency. A general guideline is also provided regarding the motor selections for a given pulse drive oper-

ation.

Chapter 7 presents a pulse drive hardware demonstration with a load power condition similar to a robotic fish. The selected gearmotor from Chapter 6 is implemented as the driving actuator. The energy efficiency is measured and compared to the conventional gear drive configuration. Some preliminary design ideas for spring packaging and latch mechanisms in actual robotic designs are also included. At the end of this chapter, we conclude this thesis and provide recommendations for future work.

1.4   Prior Art for Series Elastic Actuators

A new type of robotic drive that uses elastic elements in series with the actuator, known as "Series Elastic Actuators", has emerged over the past two decades as an alternative to the traditional "stiff" drives for force control applications. A good force source should have low reflected impedance, low stiction and high bandwidth [21]. However, traditional "stiff" drives, such as electric gear motors and hydraulic actuators, are disadvantageous in some applications because of their high reflected impedance to the load and high friction. In addition, with a "stiff" force load cell, the controller gain needs to be low to compensate for the high sensor gain, thus resulting in sluggish closed-loop performance [23]. Pratt and Williamson first proposed the idea of purposely placing a passive elastic element, such as a spring, in series with the drive transmission but before the load in association with legged locomotion [20]. The benefits of this drive configuration include high-frequency shock filtering, lowered reflected output inertia, stable force control and energy storage. Actuators with elastic element in series are particularly useful in performing accurate force control by using the elastic element as the force load cell. The force is linearly proportional to the differential position change of the elastic element. Robinson studied the closed-loop force control of series elastic actuation and observed that adding elastic elements lowered the output impedance and produced clean force tracking [23]. In addition, because of the lowered stiffness of the elastic sensor, the control gain of the system increased proportionally, resulting in better loop performance. Several tradeoffs of

the series elastic actuators are also discussed in [23], such as limited large force bandwidth.

In addition to fundamental studies, series elastic actuators have been incorporated in several real-world robotic designs. At the MIT Artificial Intelligence Lab, two bipedal walking robots M2 and Spring Flamingo have been developed with each of the active degrees of freedom controlled by an electric series elastic actuator [22]. The moving arms of the humanoid Cog, designed and constructed by Williamson, employ compliant materials and series elastic actuators at each joint for accurate force control [26]. In particular, this robot exploits the natural dynamics of each joint in actuation, such that the each actuator produces the rhythmic command by outputting an oscillating frequency close to the resonant mode of the joint. The Roboknee, a one degree of freedom exoskeleton designed by Yobotics Inc., provides human walking assistance while presenting low impedance to the wearer [21]. With the compliant spring connected between the actuator and the load and functioning as the force feedback, the actuator can amplify the wearer's intended action and generate appropriate force. The Corndog, a planar running robot designed by Krupp as part of his Master's Thesis, also includes series elastic actuators in each of the joints [16].

Another main function of the elastic element is to store and release energy. Such phenomena occurs naturally in biological locomotion. Cavagna concludes from a study on animal gait that the biological elastic elements, such as muscle and tendon, help to maintain and convert between kinetic energy and potential energy in high speed locomotion of some animals [12]. A quantitative efficiency study on the rat gastrocnemius muscle stretch-shorten cycle reveals that the series elastic element (SEE) efficiency varies from 0.02 to 0.85, and the mechanical efficiency varies from 0.43 to 0.92 [13].

Hollander et al. designed an ankle orthosis and compared the power levels and energy levels of using direct drive and using "robot tendon" [15]. The peak power reduces from 250 W to 77 W and input energy from 36 J to 21 J in the actuation cycle. In addition, the weight of the package is about seven times less. Similarly, Paluska and Herr demonstrate in a simple model that more energy can be delivered and higher instantaneous power can be reached by using a series elastic actuator than by using

direct drives in a same limited-range stroke [19]. The idea of charging and releasing spring energy in a jumping robot for power efficiency and robotic performance improvement has been explored by Scarfogliero [24]. The micro jumping robot "Grillo" is designed with the actuator connected to the springs of the legs. In continuous gait, the actuator compresses the spring during the airborne phase with power as low as 0.3 W. The spring rapidly releases the energy upon landing with power up to 5 W through a catch and release mechanism, and the robot jumps back in air. They observed that the best performance is achieved with the thrust completed just before taking off. However, no energy efficiency values were shown in the article, nor was the analytical information for tuning the actuation given. A more relevant work to my research project is the study on efficiency gain by using series elastic actuators from Sallum and Albert [9]. By placing a spring between the actuator and load and operating the actuator at the resonant mode of the spring and load inertia, an maximum efficiency gain up to 2 times is achieved with a test-stand in certain scenarios. With this overview complete, in the next chapter we examine the physics governing the pulse drive. This leads to scaling laws which can guide the design.

Chapter 2

Fundamental Efficiency Tradeoff Analysis of the Pulse Drive

2.1 Overview

In this chapter, we examine the fundamental efficiency tradeoffs for rapidly storing energy in a spring device. The analysis of charging a massless spring shows that the highest efficiency is achieved when the charging time approaches zero. Conversely, the analysis of charging a lumped mass shows that the highest efficiency is achieved when the charging time approaches infinity. These two bounding cases clarify the efficiency limits for the pulse drive. Finally, the analysis of the combined spring-mass system shows that the highest efficiency is obtained when the trajectory frequency w is slightly higher than the system's natural frequency $w_n = \sqrt{k/m}$.

2.2 Energy Efficiency of Charging a Massless Spring

Springs are commonly used mechanical energy storage devices. The change in length of a massless linear spring x is proportional to the applied force F

$$x = \frac{F}{k},\tag{2.1}$$
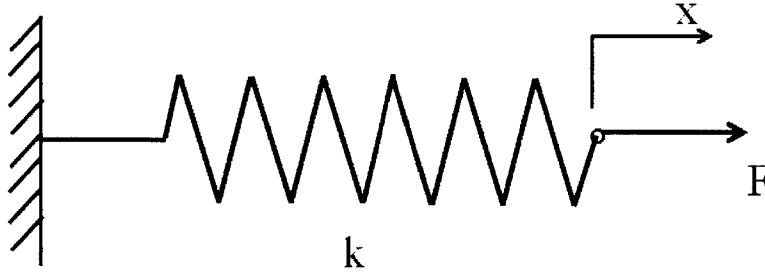
Figure 2-1: Simple massless spring system

and the stored potential energy is proportional to x^2

$$E_{spring} = \frac{1}{2}kx^2. \tag{2.2}$$

Here k is the spring constant (Figure 2-1). If we were to "charge" the spring, i.e., storing potential energy in the spring, with a ramp force starting from $F = 0$ at $t = 0$ to $F = F_0$ at $t = t_0$,

$$F = F_0\frac{t}{t_0}, \tag{2.3}$$

the displacement will follow a ramp trajectory (Figure 2-2) given by

$$x(t) = \frac{F}{k} = \frac{F_0}{k}(\frac{t}{t_0}). \tag{2.4}$$

At $t = t_0$ the potential energy stored in the spring is thus

$$E_{spring}(t_0) = \frac{1}{2}kx^2(t_0) = \frac{F_0^2}{2k}. \tag{2.5}$$

If the energy stored in the spring is considered as useful work, we would like to study the energy efficiency of the "charging" process by assuming the force is provided by an electromechanical actuator with output force F proportional to the input current i, $F = K_f i$, in which K_f is the force constant. Thus the time-dependent current expression is

$$i(t) = \frac{F}{K_f} = \frac{F_0}{K_f}\frac{t}{t_0}. \tag{2.6}$$

28
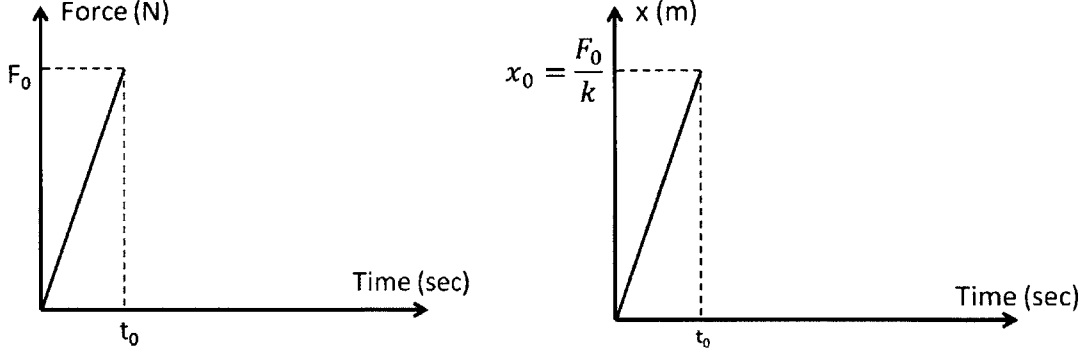
Figure 2-2: Force and displacement of the massless spring system.

The actuator is assumed to have a coil resistance R, and no internal energy storage. The instantaneous power dissipation is thus given by

$$P_{diss}(t) = i^2(t)R = \frac{R}{K_f^2}F_0^2(\frac{t}{t_0})^2.$$ (2.7)

The total energy loss in the actuator, as integrated from $t = 0$ to $t = t_0$, is

$$W_{loss}(t_0) = \int_0^{t_0} P_{diss}(t)dt = \frac{1}{3}(\frac{R}{K_f^2}F_0^2)t_0.$$ (2.8)

Note here that the energy loss is proportional to t_0 and inversely proportional to K_f^2. We define the fractional energy efficiency of the process as

$$\eta = \frac{E_{spring}(t_0)}{E_{spring}(t_0) + W_{loss}(t_0)} = \frac{\frac{F_0^2}{2k}}{\frac{F_0^2}{2k} + \frac{1}{3}(\frac{R}{K_f^2}F_0^2)t_0} = \frac{1}{1 + \frac{2}{3}k\frac{R}{K_f^2}t_0}.$$ (2.9)

Note that this ratio does not depend on F_0. For simplicity in future discussions, we define the Actuator/Motor Quality Factor Γ as the ratio between K_f^2 and R

$$\Gamma = \frac{K_f^2}{R}.$$ (2.10)

The quality factor Γ is a very useful quantity in describing the energy efficiency of typical actuators and it will appear many times in later sections. This expression is also equal to the equivalent mechanical damping of a shorted actuator, and is a good

29
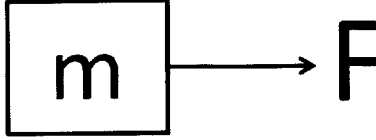
Figure 2-3: Simple mass

metric of actuator quality sometimes referred to as "stiffness". The energy efficiency thus becomes

$$\eta = \frac{E_{spring}(t_0)}{E_{spring}(t_0) + W_{loss}(t_0)} = \frac{1}{1 + \frac{2k}{3\Gamma}t_0}.$$ (2.11)

Equation (2.11) indicates that in addition to the dependency on k and Γ which are hardware parameters, the efficiency of the simple massless model is dependent on t_0, the duration of the applied force trajectory. The shorter the duration of force, the higher the efficiency will be. If we are able to rapidly charge the spring by applying a pulse force with very short duration, we may obtain high energy efficiency. In an extreme case, though not physically realistic, $\eta \to 1$ when $t_0 \to 0$. Therefore, the analysis of this simple model shows the potential of achieving high efficiency by rapidly storing energy in a spring. However, we have made the unrealistic assumption that the actuator is massless. In the next two sections we will see that the addition of the actuator mass changes the tradeoff.

2.3   Energy Efficiency of Charging a Lumped Mass

In this section, we examine the case in which a lumped mass m is actuated by a step force F (Figure 2-3). The fundamental equation is $F = ma$.   The resulting displacement profile has the shape of a parabola, as shown in Figure 2-4. The useful work is given by the stored kinetic energy of the mass W_{useful} over a period t_0

$$W_{useful}(t_0) = \frac{1}{2}m(at)^2 \mid_{t=t_0} = \frac{1}{2}\frac{F^2}{m}t_0^2.$$ (2.12)

30
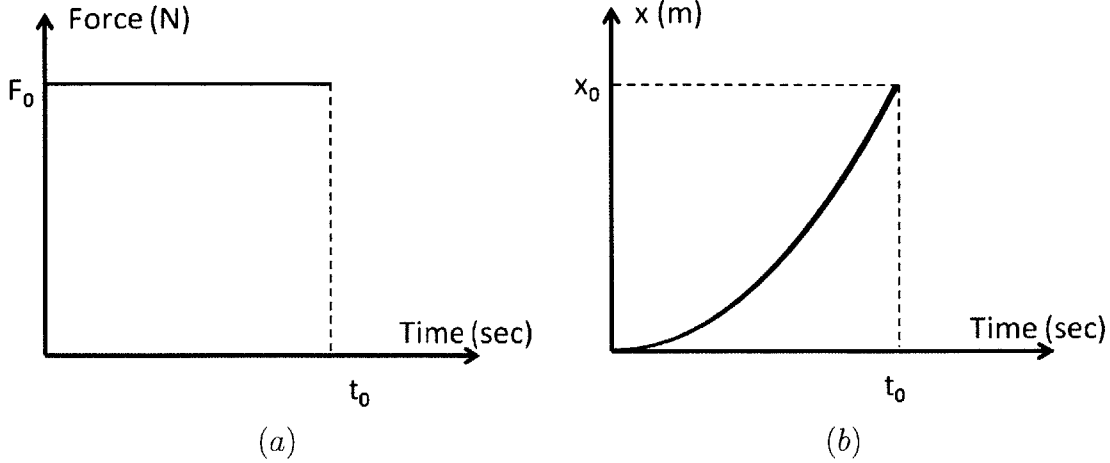
Figure 2-4: Simple mass model: (a) force, (b) displacement

Assuming the force is provided by the same actuator discussed in previous section, the electrical lost energy is

$$W_{loss}(t_0) = i^2 R t_0 = (\frac{F}{K_f})^2 R t_0. \tag{2.13}$$

As a result, the fractional energy efficiency η for mass acceleration is

$$\eta = \frac{W_{useful}(t_0)}{W_{useful}(t_0) + W_{loss}(t_0)} = \frac{1}{\frac{2m}{\Gamma}\frac{1}{t_0} + 1}. \tag{2.14}$$

Equation (2.14) shows that the efficiency is dependent on the duration of the force t_0, but not on the magnitude of the force. As opposed to charging a spring, where shorter pulses are more efficient, longer force duration will yield better energy efficiency for the mass. In the extreme case, $\eta \to 1$ when $t_0 \to \infty$. Therefore, it is undesirable to rapidly accelerate a mass with a short pulse force, as the efficiency will be low.

2.4 Energy Efficiency of a Simple Spring Mass System

We now combine the models of the previous two sections. Figure 2-5 shows the model of a one-dimensional spring-mass system with a lumped mass m and spring constant

31
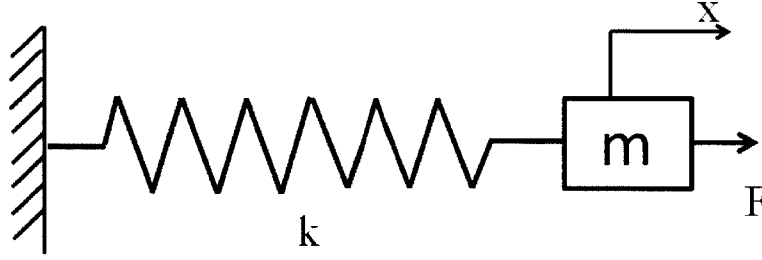
Figure 2-5: Simple spring-mass system

k. The equation of motion is

$$m\ddot{x}(t) + kx(t) = F(t), \tag{2.15}$$

where the undamped natural frequency of the system is given by $w_n = \sqrt{k/m}$. To study the effect of the pulse time on the energy efficiency, a sinusoidal pulse displacement trajectory $x(t)$ with radian frequency w is applied to the system between $0 \leq t \leq \frac{\pi}{w}$ as

$$x(t) = \frac{A}{2} - \frac{A}{2}\cos wt, \tag{2.16}$$

with velocity

$$\dot{x}(t) = \frac{A}{2}w\sin wt, \tag{2.17}$$

and acceleration

$$\ddot{x}(t) = \frac{A}{2}w^2\cos wt. \tag{2.18}$$

The initial conditions are chosen such that the initial acceleration is bounded. As a result, at the end of the pulse period $t_0 = \frac{\pi}{w}$, the mass reaches its maximum displacement $x_{max} = A$ with zero velocity. Assuming $x = 0$ corresponds with the rest position, the energy stored in the spring is

$$W_{useful} = \frac{1}{2}kA^2. \tag{2.19}$$

We still assume that the only energy loss during the pulse period is resistive heat dissipation in the actuator. The current i is proportional to the applied force which

32

is governed by Newton's Second Law as

$$i = \frac{F}{K_f} = \frac{m\ddot{x} + kx}{K_f}.$$

(2.20)

Using (2.16) and (2.18) we calculate the total energy loss as the time integration of power loss during the entire period:

$$W_{loss} = \int_0^{\frac{\pi}{w}} i^2 R\, dt = \int_0^{\frac{\pi}{w}} \frac{R}{K_f^2} (\frac{A}{2})^2 [mw^2 \cos wt + k(1 - \cos wt)]^2\, dt$$
$$= \frac{\pi R}{2K_f^2} (\frac{A}{2})^2 (m^2 w^3 - 2mwk + \frac{3k^2}{w}).$$

(2.21)

Thus the efficiency is calculated using the same equation described in previous sections

$$\eta = \frac{W_{useful}}{W_{useful} + W_{loss}} = \frac{\frac{1}{2}kA^2}{\frac{1}{2}kA^2 + \frac{\pi R}{2K_f^2}(\frac{A}{2})^2(m^2 w^3 - 2mwk + \frac{3k^2}{w})}$$
$$= \frac{1}{\frac{\pi R}{2K_f^2}[\frac{m^2 w^3}{2k} - mw + \frac{3k}{2w}] + 1}.$$

(2.22)

Equation (2.22) indicates that the efficiency is a function of the pulse frequency w. At the two extremes $w \to 0$ and $w \to \infty$, $\eta \to 0$ due to the low efficiency of moving the spring over a long period, and of moving the mass in a short period, respectively. To find the optimal efficiency, we define function $f(w)$ which is the part of the denominator of (2.22) that contains variable w. Equation (2.22) reaches its maximum when $f(w)$ is at its minimum value.

$$f(w) = \frac{m^2 w^3}{2k} - mw + \frac{3k}{2w}.$$

(2.23)

To find the maximum/minimum of $f(w)$, we take the derivative of $f(w)$ and set it equal to zero.

$$f'(w) = \frac{3m^2}{2k}w^2 - m - \frac{3k}{2}\frac{1}{w^2} = 0.$$

(2.24)

33

The only positive rational root of Equation 2.24, which happens to make $f(w)$ at its global minimum, is

$$w_{optimal} = \sqrt{\frac{2 + \sqrt{40}}{6} \frac{k}{m}} = 1.178 w_n.$$ (2.25)

Therefore, the optimal efficiency is

$$\eta_{optimal} = \frac{1}{0.9127 \frac{\pi R}{2K_f^2} \sqrt{km} + 1} = \frac{1}{\frac{1.434\sqrt{km}}{\Gamma} + 1}.$$ (2.26)

Equation (2.25) and (2.26) lay out the fundamental energy efficiency tradeoff of the spring-mass system, which forms the basis of this thesis. We have discovered that in the presence of inertia, the best way to store energy in the spring is to pulse drive the spring-mass system with a trajectory frequency slightly higher than the system's undamped natural frequency. The optimal efficiency is a function of the spring constant, motor inertia and the motor quality factor. As the inertia of the actuator approaches zero, the pulse frequency approaches infinity and the efficiency approaches unity, which resembles results from the massless spring analysis. The efficiency will also increase with the actuator quality factor. Therefore, the pulse drive has the potential to achieve high energy efficiency by using an actuator with high quality factor and low inertia. However, as the pulse time is shortened, the instantaneous power increases and raises the requirements to the actuator. Actuator and amplifier actuation will thus bound the minimum time. Moreover, the efficiency can be also improved by using a spring with lower stiffness. However, lowering the stiffness of the spring decreases w_n and thus increases the maneuver time of the load, which may be undesirable in some applications. As a final note, recall that our simple model assumes that the load is approximately fixed during the charging cycle. More detailed simulations will take account of the load movement later in this thesis. The successive chapters will discuss the efficiency of pulse drive with a viscous load and address the associated challenges and tradeoffs in more detail.

2.5 Summary of the Chapter

- The most efficient way to "charge" a massless spring is to apply a pulse force/torque with an infinitely small period while the most efficient way to "charge" a pure inertia is to apply the force/torque over an infinitely long period.

- The most efficient way to store energy in a spring in the presence of actuator inertia is to apply a pulse displacement trajectory with pulse frequency close to the natural frequency of the spring-inertia system.

- To achieve high efficiency of such a pulse drive, we need to use an actuator with high quality factor and low inertia.

Chapter 3

Modeling and Simulation of the Pulse Drive System

3.1 Overview

In this chapter, we first model the pulse drive system in a simple one-dimensional linear translation form with lumped parameters. The effects of adding transmissions or using different trajectory profiles are examined in later sections. The analytical calculation results are compared to simulation results in a case study with numeric parameters.

3.2 Model of Simple Pulse Drive with Direct Connection

3.2.1 Modeling and Assumptions

Figure 3-1 shows a schematic of the pulse drive system model. Even though our hardware prototype is a rotational system, we model the system in the translational domain for the sake of simplicity and clarity. The actuator of the system is modeled as an ideal linear DC motor with lumped mass m_d. The input force $F(t)$ is proportional to input current $i(t)$ with a gain of K_f. The load is modeled as a viscous damper
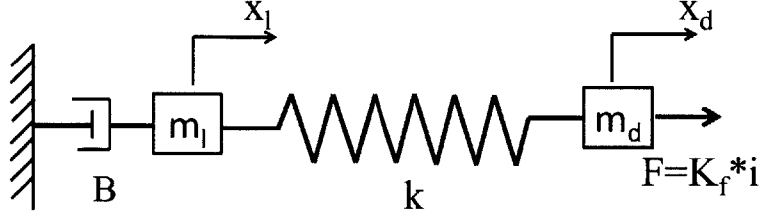
Figure 3-1: Simple modeling of the pulse drive system in translational motion. The EM actuator is modeled as a mass m_d with an input force F proportional to the input current i. The load is modeled as a mass m_l and a damper B.

with constant damping value B and a lumped mass m_l. The actuator and the load are connected through an ideal spring with Hooke's constant k. The displacement of the actuator and the load are $x_d(t)$ and $x_l(t)$, respectively. The equations of motion are

$$m_d \ddot{x}_d(t) + k(x_d(t) - x_l(t)) = F(t) = K_f i(t), \tag{3.1}$$

$$m_l \ddot{x}_l(t) + B \dot{x}_l(t) = k(x_d(t) - x_l(t)). \tag{3.2}$$

In a half work cycle, a half period sinusoidal displacement trajectory pulse described by (2.16) with radian frequency $w = 1.178\sqrt{k/m_d}$ is first actuated on m_d. During this period, the actuator displacement will be much larger than the load displacement, $x_d \gg x_l$, due to the high viscous damping force generated by the load. Such motion results in a rapid expansion of the spring where the kinetic energy of m_d is converted into the potential energy in the spring. When the actuator reaches its maximum position x_{dmax} and $\dot{x}_d = 0$, we assume that a latch mechanism, which is not included in this model, latches m_d at position x_{dmax}. The spring then transfers energy to the viscous load over a longer time scale. A preliminary sketch of the displacement in the half work cycle is shown in Figure 3-2. Once the spring returns to near its unstressed position, m_d is unlatched and the next half work cycle begins. Alternating trajectory pulses can be applied to maneuver the load in a periodic motion. With such a design, (2.26) is applicable to estimate the efficiency of the half work cycle, because under our assumption, m_l remains almost stationary when the pulse force is being applied. One

38
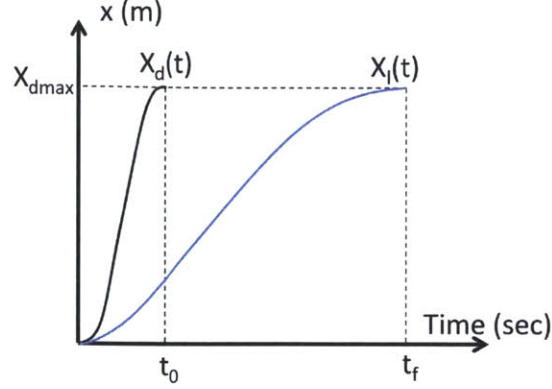
Figure 3-2: Half work cycle of the pulse drive showing input position $x_d(t)$ and load position $x_l(t)$. Under a rapid expansion, $x_d(t)$ reaches final position x_{dmax} at $t = t_0$ and is locked at that position while x_l converges to x_{dmax} over a longer time scale at $t = t_f$.

additional assumption we make in the model is that resistive power dissipation by the actuator coil is the dominant form of energy loss. The power dissipation by bearing friction, the latch mechanism, and any other sources are neglected in the analysis.

3.2.2 Simple Model of the Conventional Drive with a Direct Stiff Connection

To compare the pulse drive model with the conventional drive train design, a simple translational direct drive model with the same characteristics is constructed as shown in Figure 3-3. Instead of using a spring connection, a rigid rod is connected between m_d and m_l so that $x_d(t) = x_l(t)$. The equation of motion is thus

$$(m_d + m_l)\ddot{x}_d(t) + B\dot{x}_d(t) = F(t) = K_f i(t). \tag{3.3}$$

Since we are more interested in the energy consumption and the end-to-end position of the load than the actual displacement profile at this point, we simplify this preliminary analysis by applying a sinusoidal input current $i(t) = A\sin(\omega t)$ to achieve a sinusoidal displacement at steady state. To calculate the steady state displacement profile, we

39
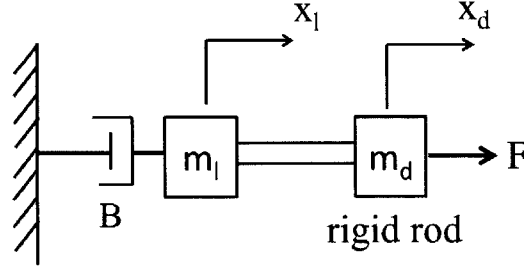
Figure 3-3: The direct drive model where the spring is replaced by a rigid rod.

find the transfer function of $X_d(s)/I(s)$

$$\frac{X_d(s)}{I(s)} = \frac{K_f}{(m_d + m_l)s^2 + Bs}. \tag{3.4}$$

At input frequency $s = jw$, the amplitude ratio between $X_d(s)$ and $I(s)$ is

$$\left|\frac{X_d(jw)}{I(jw)}\right| = \frac{K_f}{\sqrt{(m_d + m_l)^2 w^4 + B^2 w^2}}. \tag{3.5}$$

Thus the steady state time response of the displacement is

$$x_l(t) = x_d(t) = \frac{AK_f}{\sqrt{(m_d + m_l)^2 w^4 + B^2 w^2}} \sin(wt + \phi) \tag{3.6}$$

where ϕ is the phase lag relative to the input current. And the velocity profile $\dot{x}_d(t)$ is

$$\dot{x}_d(t) = \frac{AK_f w}{\sqrt{(m_d + m_l)^2 w^4 + B^2 w^2}} \cos(wt + \phi). \tag{3.7}$$

In one cycle, the power dissipation as heat in the actuator coil is

$$W_{loss} = \int_0^{\frac{2\pi}{w}} i(t)^2 R dt = \int_0^{\frac{2\pi}{w}} A^2 \sin^2(wt + \phi) dt = \frac{\pi A^2 R}{w}. \tag{3.8}$$

40

The useful work is given by

$$W_{useful} = \int_0^{\frac{2\pi}{w}} B\dot{x}_d^2(t)dt = \int_0^{\frac{2\pi}{w}} B\frac{A^2K_f^2w^2}{(m_d+m_l)^2w^4 + B^2w^2}\cos^2(wt+\phi)dt$$

$$= \frac{A^2K_f^2B}{(m_d+m_l)w^2 + B^2}\frac{\pi}{w}.$$

(3.9)

Therefore the fractional energy efficiency of the direct drive is calculated to be

$$\eta_{direct\ drive} = \frac{W_{useful}}{W_{useful}+W_{loss}} = \frac{\frac{\pi BA^2K_f^2}{w(B^2+(m_d+m_l)^2w^2)}}{\frac{\pi BA^2K_f^2}{w(B^2+(m_d+m_l)^2w^2)} + \frac{\pi A^2R}{w}}$$

$$= \frac{1}{\frac{1}{\Gamma}(B + \frac{(m_d+m_l)^2w^2}{B}) + 1}.$$

(3.10)

This result is utilized in the comparisons which follow.

3.2.3 Efficiency Comparison

The analytical efficiency expression of the conventional direct drive model (3.10) shows that the efficiency depends on several parameters. It is inversely proportional to the load damping B, the square of the system inertia $(m_d + m_l)^2$ and the square of the operating frequency w^2. Thus the efficiency will drop as the load damping, the system inertia or the operating frequency become larger. Moreover, in the case of a relatively large damping load, which is our target operating condition, we can approximate the efficiency by omitting the term $\frac{(m_d+m_l)^2w^2}{B}$, yielding

$$\eta_{direct\ drive} \approx \frac{1}{\frac{B}{\Gamma} + 1}$$

(3.11)

Thus, in this case the efficiency is inversely proportional to the ratio of the load damping value to the actuator quality factor $\frac{B}{\Gamma}$. In contrast, the efficiency of the pulse drive model in (2.26) shows that the efficiency is independent of the load damping value or the load inertia. However, if we were to have the spring maneuvering different loads to similar amplitude over the same time scale, the time constant defined by $\tau = \frac{k}{B}$ needs to be kept roughly constant. Thus the chosen spring constant needs to

41

be proportional to B. By replacing $k = \tau B$ into (2.26), we obtain

$$\eta_{pulse\ drive} = \frac{1}{\frac{1.434\sqrt{\tau B m_d}}{\Gamma} + 1} \tag{3.12}$$

Hence the pulse drive efficiency is inversely proportional to the ratio of $\frac{\sqrt{B m_d}}{\Gamma}$. We compare the two efficiency expressions from two perspectives. On the driver side, an actuator with a high actuator quality factor is desired to achieve high efficiency in the conventional drive whereas the ideal actuator for the pulse drive is one with not only a high actuator quality factor but also a low inertia. On the load side, the load damping plays a less significant role on the pulse drive efficiency, which is on the order of $\sqrt{B}$, compared to the conventional drive efficiency, which is on the order of B. As the load increases, the efficiency of the pulse drive decreases at a slower rate than the efficiency of the conventional drive. Therefore, by choosing an actuator with a high motor quality factor and a low inertia, our new pulse drive has the potential to achieve higher efficiency than the conventional drive with a high impedance load. A case study with simulation results is shown in the following section which shows these tradeoffs.

3.2.4   Case Study and Simulation Results

Simulation Methodology

We construct a Simulink model (Figure 3-4) to simulate the dynamics of the pulse drive based on (3.1) and (3.2). The actuator is modeled based on the specifications of the MAXON RE 25 permanent magnet brushed DC Motor with part number 118745. The specifications are summarized in Table 3.1. The same DC motor is also used in our first hardware demonstration described in Chapter 4. Four load damping values are chosen in which the lowest one is equal to the motor quality factor K_f^2/R, and the highest one is eight times as large. The overall cycle frequency f and load amplitude A_{load} are selected to be 1 Hz and $\frac{\pi}{2}$ to mimic actual robotic fish movements. As we have pointed out from the previous section, under the same time constraint, the spring
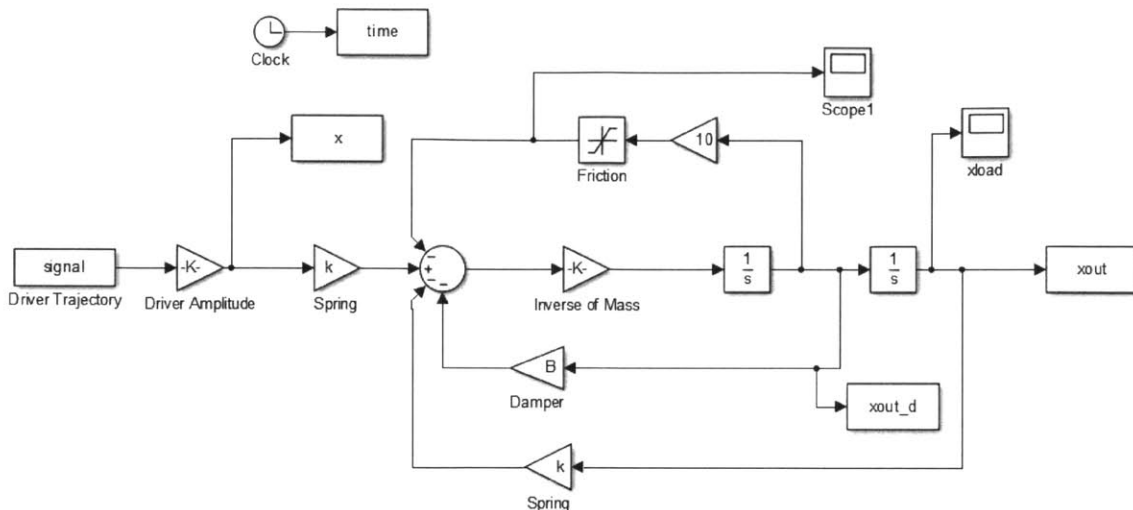
Figure 3-4: Simulink diagram for pulse drive.

Made	Model	P_r (W)	K_t (Nm/A)	R (Ω)	J (kgm^2)	Γ (Nms/rad)
Maxon	118745	10	0.0357	5	1×10^{-6}	2.55×10^{-4}

Table 3.1: Maxon RE 25 brushed permanent magnet DC motor specifications. The notation P_r stands for rated output power.

constants are proportional to load damping value. After some preliminary trials, the spring constant for the four cases are selected as 0.0011 Nm/rad, 0.0022 Nm/rad, 0.0044 Nm/rad and 0.0088 Nm/rad.

We also wrote a Matlab script to numerically simulate the direct drive process with the ODE 45 solver based on (3.3). The same driver motor , load values and operation conditions are incorporated in the simulation. The simulation parameters are summarized in Table 3.2.

Cases	k (Nm/rad)	B	A_{load} (rad)	w (rad/s)	w/w_n	f (Hz)
1	0.0011	Γ	$\pi/2$	36.5	1.1	1
2	0.0022	2Γ	$\pi/2$	36.5	1.1	1
3	0.0044	4Γ	$\pi/2$	36.5	1.1	1
4	0.0088	8Γ	$\pi/2$	36.5	1.1	1

Table 3.2: Simulation parameters for the pulse direct drive and the conventional direct drive. Four cases with different load damping values are simulated with the lowest damping value equal to the driver motor quality factor Γ. The spring constants increase proportionally with damping values to match up the time constant.

43

Results and Discussion

Figure 3-5 shows a comparison between the theoretical and simulated pulse drive efficiencies of Case 1 at different normalized pulse speeds $\frac{w}{w_n}$ in which the theoretical efficiencies are calculated from (2.22). Both results show similar behaviors where the efficiency reaches a maximum value at a pulse speed close to the natural frequency of the spring-inertia system. The simulated efficiency has a peak of 87% at $w = 1.1w_n$ while the analytical expression predicts the peak to be 84% at $w = 1.2w_n$. Overall, the optimal pulse speed simulation validates the usefulness of (2.22) and (2.26) in predicting the pulse drive efficiencies. We postulate that the slight shift of the optimal pulse speed and the small gain of efficiency in the simulation results might be the combined consequences of the dynamics of the damper at the beginning of each actuation cycle and the spring recovery energy from previous cycles which are not modeled in the theoretical analysis.

To verify this hypothesis, we carried out two additional simulations. In the first simulation, we keep the load equal to Γ but change the overall cycle frequency to 0.1 Hz so that the load displacement eventually catches the driver displacement and the recovery energy from the spring is minimal. In the second simulation, we change the load to 2Γ along with a cycle frequency of 0.1 Hz, so that the dynamics of the damper during the pulse period are reduced. The displacement profiles and the efficiency results for the two cases are shown in Figures 3-6 and 3-7, respectively. Without the recovery energy from the spring, the difference between the simulated peak efficiency and the analytical calculation is within 1%. Moreover, with the increased damping, the simulated efficiency profile more closely resembles the analytical profile.

Upon verifying the relation between the efficiency and the pulse speed in simulation, we simulate the pulse drive process at the simulated optimal pulse speed $w = 1.1w_n$ and the conventional direct drive at the same cycle frequency. A sample displacement profile of one operating cycle in Case 1 is shown in Figure 3-8. The efficiency results are summarized in Table 3.3 and visualized in Figure 3-9. In the table, P_P is the average mechanical output power for the pulse drive and P_D is the average mechan-
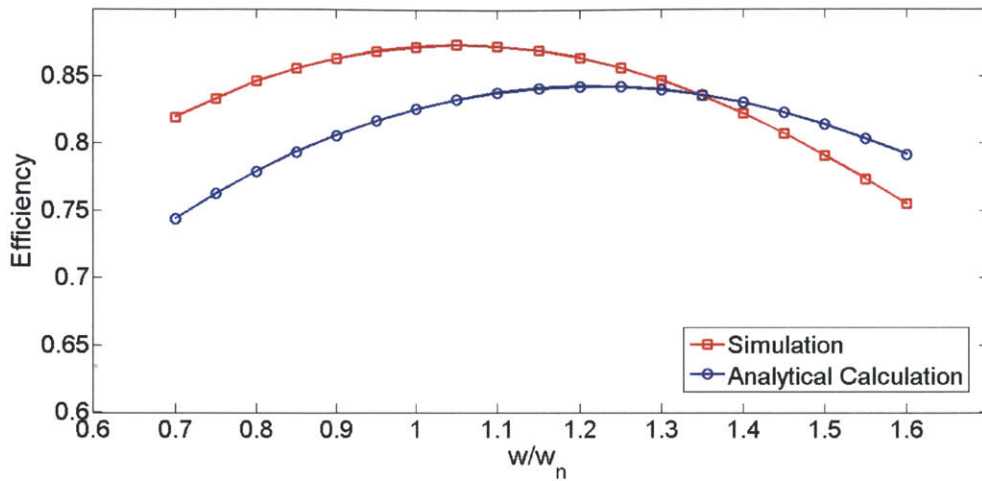
Figure 3-5: Plots of the pulse drive efficiency at different normalized pulse speeds w/w_n. The simulation indicates a peak efficiency of 87% at $w = 1.1w_n$ while the analytical derivation predicts the peak efficiency to be 84% at $w = 1.2w_n$.
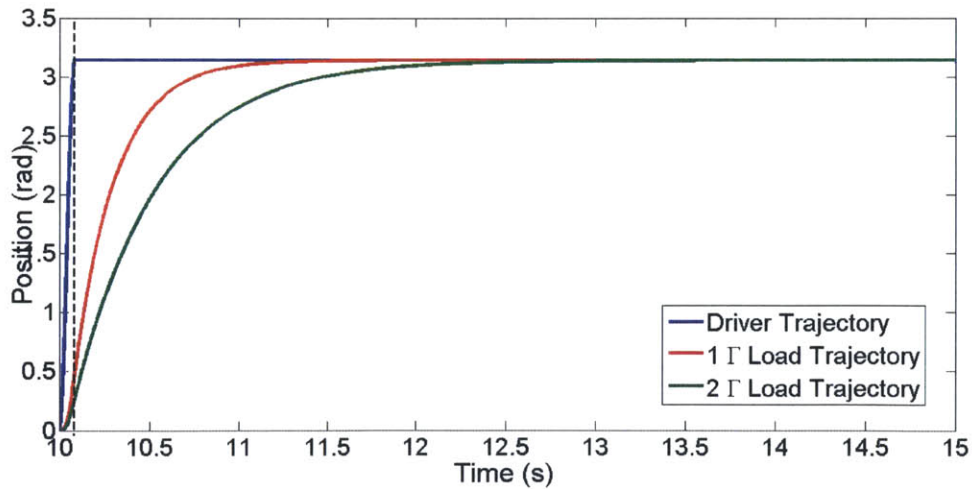
Figure 3-6: Plots of the displacement profile at 0.1 Hz cycle frequency for loads of 1 Γ and 2 Γ. With the same spring, a larger load yields a slower time response. In addition, the initial load movement during the pulse phase is reduced at the larger load.
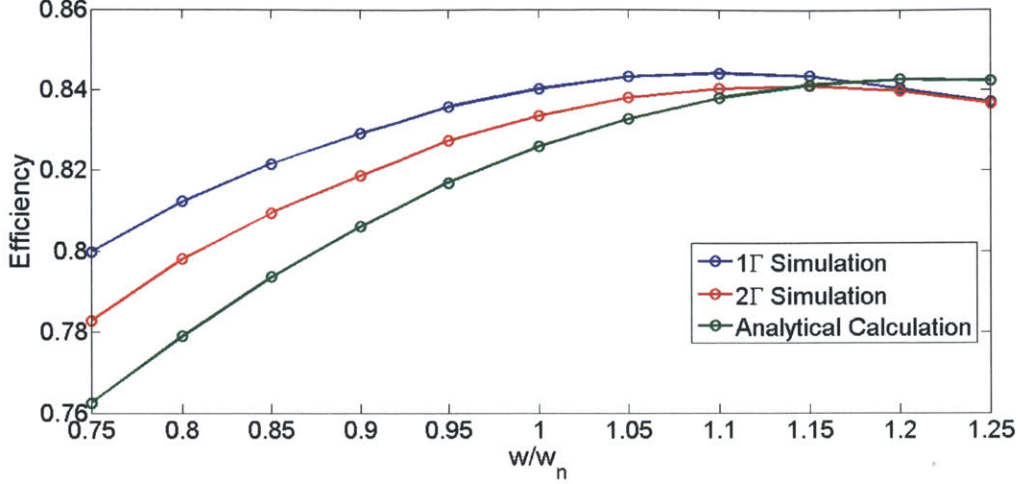
Figure 3-7: Plots of the pulse drive efficiency at 0.1 Hz cycle frequency. With such low cycle frequency, the effect of recovery energy at the beginning of each cycle is minimized, thus the simulated efficiency results are closer to the analytical predictions. Moreover, the simulated efficiency results with larger load are closer to the analytical predictions because of the reduced effect of load dynamics during the pulse phase.

ical output power for the conventional direct drive. The subscript notation P, D, t and s respectively represent for the pulse drive, the conventional direct drive, the theoretical results and the simulation results. In each case, the output power levels are similar for both drive cases, demonstrating that the pulse drive is able to produce a similar propulsion power to the load.

Overall the simulated efficiency results confirm previous analytical calculations. The simulated efficiencies for the pulse drive are only 3% higher than the analytical in all

Case	$P_P(W)$	$P_D(W)$	$\eta_{P,t}$	$\eta_{P,s}$	$\eta_{D,t}$	$\eta_{D,s}$
1	0.0139	0.0127	84.27 %	87.25 %	49.95%	49.93%
2	0.0284	0.0254	79.12 %	82.49 %	33.33%	33.32%
3	0.0580	0.0510	72.82%	76.41%	20.00%	20.00%
4	0.1176	0.1017	65.46 %	69.00 %	11.11%	11.11%

Table 3.3: Simulated power level and efficiency comparison of the pulse direct drive and the conventional direct drive for different loads. Here P_p is the output power for the pulse drive and P_D is the output power for the conventional direct drive. The subscript notation P, D, t and s respectively represent for the pulse drive, the conventional direct drive, the theoretical results and simulation results. In each case, the power level is similar for both drive cases. The efficiency is also plotted in Figure 3-9.

46
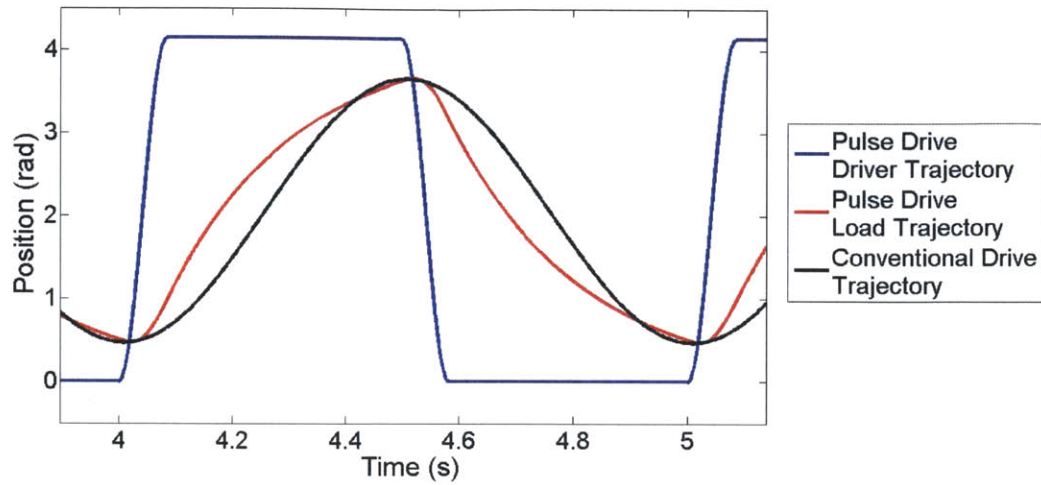
Figure 3-8: Plots of simulated trajectories of the pulse direct drive and the conventional direct drive in Case 1. The peak-to-peak load displacement of the two drive cases are both approximately π radians.
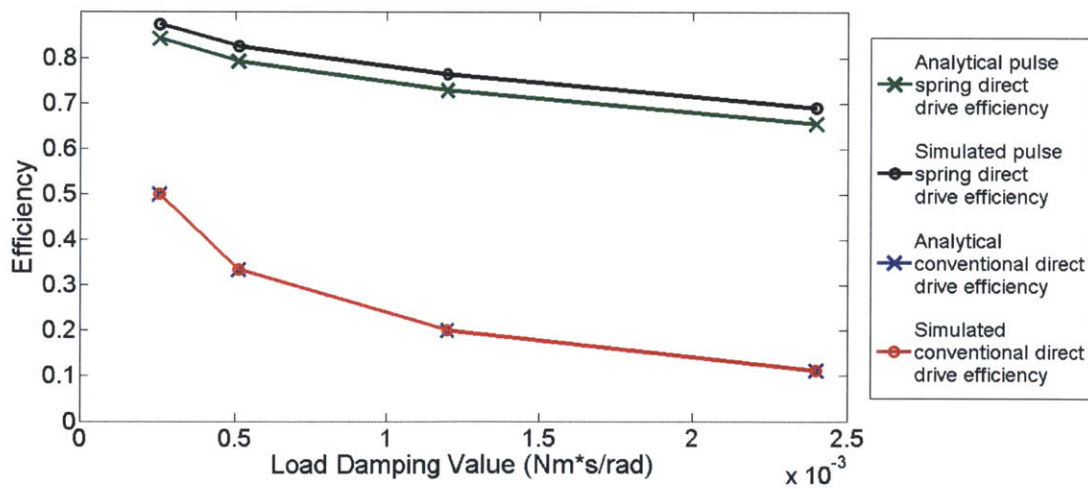
Figure 3-9: Efficiency comparison of the pulse direct drive and conventional direct drive at different load damping values. For both drives, the efficiency drops as the load increases. The pulse direct drive shows a significant efficiency gain over the direct drive in all cases. The efficiency improves from 50% to 85% at the lowest load and from 10% to 65% at the largest load.

cases while the conventional drive results remain very close. In each case with similar load amplitude and load power level, we observe significant efficiency gain by choosing the pulse drive over the conventional drive. In addition, the efficiency loss due to an increased load is less significant for the pulse drive than the conventional drive. Such observations can be explained by comparing the two efficiency expressions of (3.12) and (3.11) in Section 3.2.3. With the same motor specs and cycling frequency, the pulse drive efficiency is decreasing at the rate of $\sqrt{B}$ while the conventional direct drive efficiency is decreasing at the rate of B. Therefore, the efficiency of the pulse drive drops more slowly with B than the conventional drive.

3.2.5 Short Summary

We model and simulate the pulse drive with direct connection as well as the conventional direct drive. The simulated efficiency results agree well with analytical calculations. The pulse drive efficiencies are at least 30% higher than the conventional direct drive in the chosen simulation scenarios. We also conclude that the pulse drive efficiencies are less sensitive to load variations so that it might be more power efficient for large damping load maneuvering tasks.

3.3 Effects of Adding Gearbox Transmission

3.3.1 Gearbox Modeling

Gearbox transmissions are widely used to change the input to output speed, torque ratio and rotational directions. They usually consist of several rotational and/or stationary gears meshing, as well as with lubrication added. A common application in robotics is to magnify the output torque by reducing the output speed. With a total gear ratio of N, input speed w_{in} and output speed w_{out} have the relationship $\frac{w_{in}}{w_{out}} = N$. Assuming a single value estimated power efficiency, the power transfer equation is $\eta_g P_{in} = P_{out}$, where $0 < \eta_g < 1$. Thus, with power being the multiplication

of rotational speed and torque, the instantaneous torque transfer equation is

$$T_{out} = \eta_g T_{in} \frac{w_{in}}{w_{out}} = \eta_g N T_{in}. \tag{3.13}$$

3.3.2 Literature Search on Gearbox Efficiency

The efficiency of gears and gearboxes has been studied extensively. For example, Dudley's gear handbook lists gearbox loss from three sources, the gear meshing loss P_t, the bearing loss P_b, and the windage loss P_w [25] (Chapter 12.5). The percent power loss P_t due to the gear meshing is given as

$$P_t = \frac{50f}{\cos\phi}\left(\frac{H_s^2 + H_t^2}{H_s + H_t}\right), \tag{3.14}$$

where f is the average coefficient of friction, ϕ is the pressure angle, H_s is the specific sliding velocity at start of approach action and H_t is the specific sliding velocity at end of recess action. Both H_s and H_t are proportional to the rotating velocity. As a result, P_t is proportional to the rotational velocity. The bearing loss P_b is proportional to the rotational speed which is given as

$$P_b = \frac{Tn}{63000} \tag{3.15}$$

where P_b is in the unit of horsepower, T is the torque loss per bearing in the unit of lb-in and n is the rotational speed in the unit of rev/min. The windage loss P_w is proportional to the third order of rotational speed which is given as

$$P_w = \frac{n^3 D^5 L^{0.5}}{10^{17}}, \tag{3.16}$$

where P_w is in the unit of horsepower, n is the rotational speed in the unit of rev/min, D is the diameter of rotating element and L is the length of the rotating element. Such result shows that the gearbox loss is velocity dependent. Michaelis et al studies the gearbox efficiency for automotive applications and identifies four sources of power loss: gears, bearings, seals and auxiliaries [17]. The loss from gears and bearings

49

can be further categorized as no-load power loss and load-dependent power loss. The power loss in the gears also depends on the immerse depths of the lubrication.

For the efficiencies of commercial gearboxes, most manufacturers, such as Maxon and Faulhaber only provide a single gearbox efficiency value which is the maximum efficiency measured during testing as a reference [5][4]. However, under different operating conditions, the efficiency can vary. A study on the gearhead efficiency using 16 mm planetary gears with a reduction ratio of 134:1 shows that the gearhead efficiency rapidly drops to near zero at very low load torque [14]. As the torque increases, the gearhead efficiency increases and approaches to a maximum efficiency of about 70% [14]. Similar results are obtained from a study conducted by Neugart which is a company specialized in servo gearhead manufacturing [2]. The study also shows that with the same output torque and same input speed, the gearhead efficiency decreases as the gear ratio increases.

As a short conclusion from the literature search, we find that there are several sources of loss in the gearbox, and the losses depend on many factors such as speed and output torque. However, due to the complex nature of the gearbox system and various designs by different manufacturers, we are unable to find any established complete model for the gearbox efficiency. Therefore, in our analytical derivation and simulation, we use the single maximum efficiency value as a starting point. In later chapters with experimental data, we fit a simple gearbox torque model and calculate the corresponding efficiency.

3.3.3 Analytical Efficiency Expression for the Pulse Gear Drive

We adopt the same linear translation model and actuation method described in Section 3.2 to derive the efficiency expression with gearbox transmission. We assume that x_{in} is the displacement at the output end of the gearbox. Thus the displacement at the gearbox input (motor input) is Nx_{in} as a result of the gear ratio N. Here $N > 1$ indicates a speed reduction from input to output. In the rapid pulsing period,

50

the force balance becomes the following

$$\eta_g(K_f i - mN\ddot{x}_{in}) = \frac{kx_{in}}{N}, \tag{3.17}$$

where η_g is the gearbox efficiency. As before, we assume that the load rotation is fixed during the pulse actuation due to a large damping. By substituting the displacement profile from (2.16), the current is calculated as

$$i = \frac{1}{K_f}(\frac{A}{2}mNw^2\cos wt + \frac{\frac{A}{2}(1-\cos wt)k}{\eta_g N}). \tag{3.18}$$

The energy loss due to actuator coil resistive heat loss is integrated to be

$$W_{loss} = \int_0^{\frac{w}{\pi}} i^2R\ dt = \frac{R}{K_f^2}(\frac{A}{2})^2[\frac{\pi}{2}m^2N^2w^3 - \frac{\pi mkw}{\eta_g} + \frac{3\pi k^2}{2N^2\eta_g^2 w}]. \tag{3.19}$$

Therefore, the pulse drive fractional energy efficiency with the gearbox becomes

$$\eta = \frac{W_{useful}}{W_{useful} + W_{loss}} = \frac{1}{\frac{\pi R}{2K_f^2}[\frac{m^2N^2w^3}{2k} - \frac{mw}{\eta_g} + \frac{3k}{2N^2\eta_g^2 w}] + \frac{1}{\eta_g}}. \tag{3.20}$$

Note that the efficiency has a similar relationship with w compared to (2.22). By going through the same process of finding the global minimum of the denominator, we determine the optimal trajectory speed to be

$$w_{optimal} = 1.178\frac{w_n}{N\sqrt{\eta_g}}, \tag{3.21}$$

and the optimal efficiency is

$$\eta_{optimal} = \frac{1}{0.9127\frac{\pi R}{2K_f^2}\frac{1}{N(\sqrt{\eta_g})^3}\sqrt{km} + \frac{1}{\eta_g}}. \tag{3.22}$$

Equation (3.22) indicates that with the gearbox transmissions added, the efficiency also depends on the gear ratio N and the gearbox efficiency η_g. Higher N increases $\eta_{optimal}$. However, the gearbox efficiency η_g will decrease at higher N which can lower

51

the overall efficiency. In addition, higher N also reduces $w_{optimal}$ which will make pulse drive inapplicable in some cases due to the slow pulse trajectory frequency. Therefore, there are tradeoffs for the gear ratios which will be explored further with simulations in Section 3.3.5 and with hardware experiments in Chapter 5.

3.3.4 Analytical Efficiency Expression for the Conventional Gear Drive

To compare the efficiency of the pulse gear drive to the conventional gear drive, we add the gearbox transmission to the direct drive model presented in Section 3.2.2 and derive the corresponding efficiency expression. With a gear ratio of N, the equations of motion become

$$\eta_g(K_f i - N\ddot{\theta}J) = \frac{B\dot{\theta}}{N}. \tag{3.23}$$

The heat dissipation due to current in the motor coil is

$$W_{loss} = \int_0^{\frac{w}{\pi}} i^2 R\ dt = \frac{A^2}{2\Gamma}\left(\frac{\pi}{2}N^2 w J^2 + \frac{\pi B^2}{N^2 \eta_g{}^2}\right). \tag{3.24}$$

The useful work done by the load damper is

$$W_{useful} = \int_0^{\frac{w}{\pi}} B\dot{\theta}^2\ dt = \frac{\pi A^2 B}{8w}. \tag{3.25}$$

Therefore the efficiency is calculated as

$$\eta = \frac{W_{useful}}{W_{loss} + \frac{W_{useful}}{\eta_g}} = \frac{1}{\frac{1}{\Gamma}\left(\frac{N^2 w^2 J^2}{B} + \frac{B}{N^2 \eta_g}\right) + \frac{1}{\eta_g}}. \tag{3.26}$$

The efficiency expression for the conventional gear drive has the same tradeoff with (3.10), with the damping B being scaled down by a factor of N^2.

No. of Stages	Typical N	Typical Listed Efficiency	Chosen Efficiency
1	$2 \sim 5$	$85\% \sim 90\%$	85%
2	$6 \sim 25$	$70\% \sim 80\%$	70%
3	$26 \sim 125$	$60\% \sim 70\%$	60%

Table 3.4: Typical planetary gearbox efficiency values and range of gear ratios for each stage by Maxon and Faulhaber [5][4].

3.3.5   Simulation Results

Gear Efficiency Assumptions

Since it is not easy to accurately model the gearbox efficiency in terms of speed and load, we use the single figure maximum gear efficiency specified by the manufacturers as the efficiency value in the simulation. The typical efficiency values and range of gear ratios for one-stage to three-stage planetary gearboxes from manufacturers such as Maxon and Faulhaber are summarized in Table 3.4 [5][4]. Note that the cut off gear ratio between each stage is conveniently chosen for our simulation purpose and the actual gear ratios in each stage can vary depending on individual design. The lower end of the efficiency range is picked as the efficiency value used in simulation for two reasons. One reason is that we want to be conservative in the simulation and the other reason is that the actual gearbox efficiency will be lower than its maximum efficiency at different loads and speeds.

Preliminary Results on Efficiency Tradeoffs

As mentioned in Section 3.3.1, a higher gear ratio N don't necessarily lead to higher efficiency for the pulse gear drive. Longer pulse period and lower gear efficiency will compromise the overall performance. To explore the tradeoff, we scale (3.22) using the Maxon 118745 DC brushed motor specifications and calculate the efficiency and the pulse period under various load damping values and gear ratios. The pulse period is calculated as $t_{pulse} = \pi/w$. The load damping value B is varied from 1Γ to 16Γ and the gear ratio N from 1 to 25. Note the case of $N = 1$ corresponds to no gearbox. The results are summarized in Figure 3-10. At the smallest load, the highest efficiency is obtained with the direct connection as it is not affected by the gearbox efficiency. At

53

larger load, the highest efficiencies are obtained with the highest gear ratio of one-stage gearbox. Efficiencies with two-stage gearbox in all cases are limited by the 70% gearbox efficiency. Time wise, we consider 0.2 s as the upper limit of pulse applying period if we are to maneuver a load at 1 Hz as might be the case in robotic fish tail actuation. The majority of a one-stage gearbox cases satisfy the time constraint except for a few cases with small load. For two-stage gearboxes, only the cases with lower gear ratios and larger load fall into the range. However, the efficiencies in those cases are much lower than the corresponding one-stage gearbox cases. In a short conclusion, we learn from the preliminary results that one-stage gearboxes with the highest gear ratio are better options for the pulse gear drive and the corresponding efficiencies are higher than those with no gearbox or two-stage gearboxes.

Simulation Results with One-Stage Gearbox

We modify the Simulink model shown in Figure 3-4 to simulate the pulse drive process with the gearbox transmission. The driver motor is modeled using the Maxon 118745 DC motor specifications. The gear ratio is set at $N = 5$ which is the maximum one-stage gearbox ratio specified in Table 3.4. The simulation covers a wide range of load damping value B from 4Γ to 32Γ where Γ is the actuator quality factor of the driver motor and the spring constant k is chosen accordingly to match the spring damper time constant. The pulse speed is chosen to be $0.95\ w_{eq}$ based on the optimal pulse speed analysis presented in Figure 3-11. Here w_{eq} is defined as the equivalent natural frequency of the spring and the gearmotor inertia that it is scaled down by the gear ratio

$$w_{eq} = \frac{1}{N}\sqrt{\frac{k}{J}}. \tag{3.27}$$

The overall cycle frequency is kept at $f = 1$ Hz. We also simulate the conventional gear drive process (no spring) with the same operating conditions at $N = 5$ for one-stage gearbox and $N = 25$ for two-stage gearbox with the ODE 45 solver. The simulation parameters are summarized in Table 3.5. Figure 3-11 shows the optimal pulse speed analysis for Case 1. The simulation results indicate that the maximum

54

(a)

(b)
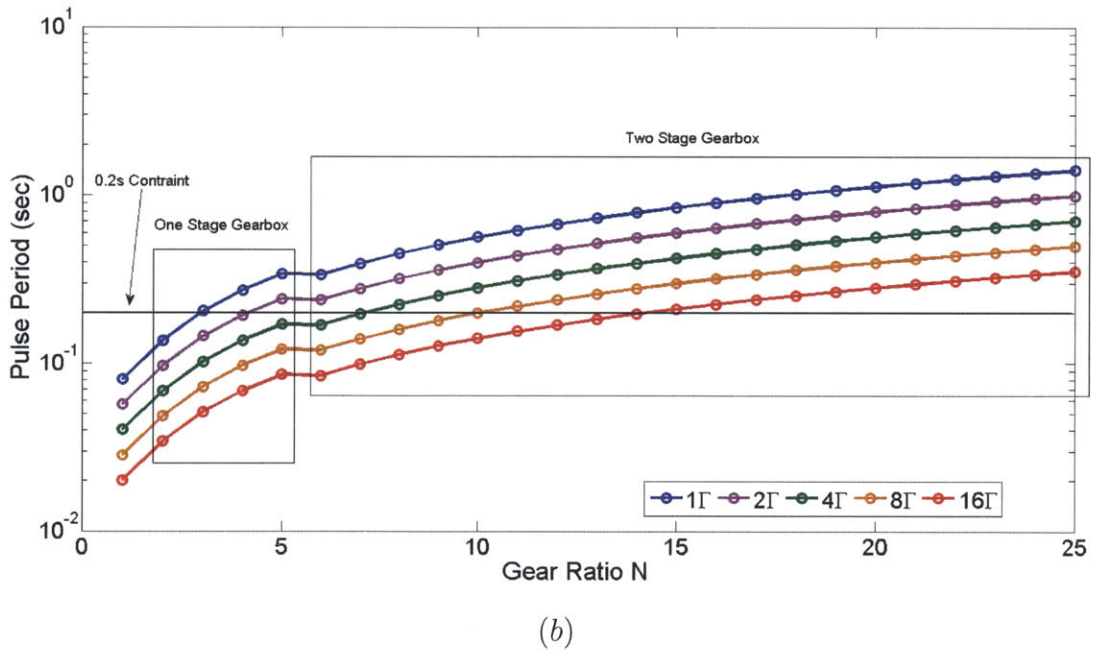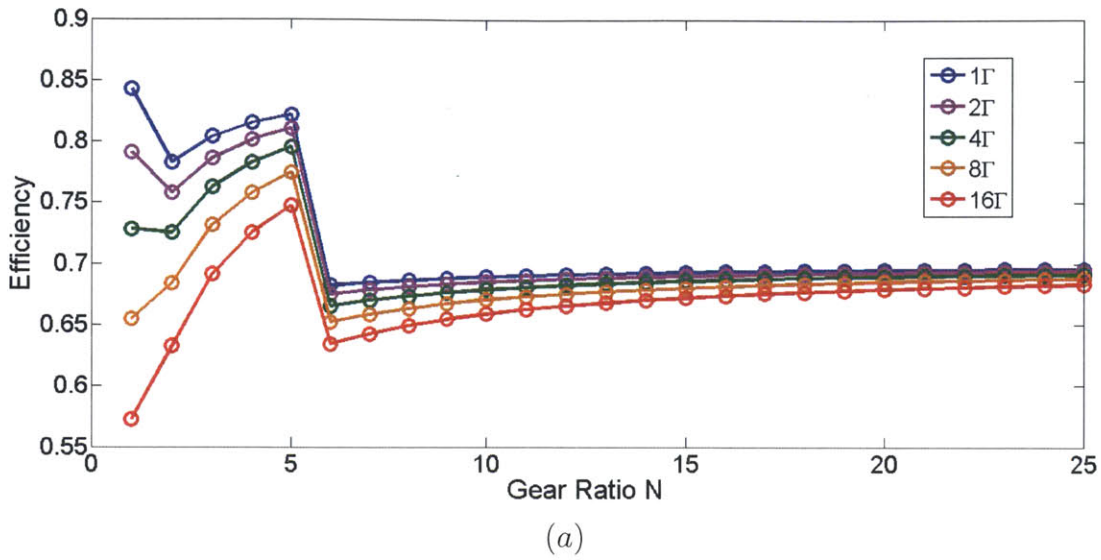
Figure 3-10: Plots of (a) the pulse gear drive efficiency and (b) the pulse period, at various load damping values and gear ratios. Note that the efficiency drops at $N = 2$ and $N = 6$ correspond to the change in gear efficiency from no gearbox to one-stage gearbox, and from one-stage gearbox to two-stage gearbox. At 1Γ load, the highest energy efficiency is obtained with direct connection while for larger load the highest energy efficiencies are achieved with the highest gear ratio of the one-stage gearbox.

Cases	B	k (Nm/rad)	A_{load}	w/w_{eq}	f (Hz)	N_{pulse}	$N_{conventional}$
1	4Γ	0.0044	$\frac{\pi}{2}$	0.95	1	5	5 and 25
2	8Γ	0.0088	$\frac{\pi}{2}$	0.95	1	5	5 and 25
3	16Γ	0.0176	$\frac{\pi}{2}$	0.95	1	5	5 and 25
4	32Γ	0.0352	$\frac{\pi}{2}$	0.95	1	5	5 and 25

Table 3.5: Simulation parameters for the pulse drive and the conventional gear drive. The pulse drive is simulated with both direct connection and with a one-stage gearbox $N = 5$. The conventional gear drive is simulated with both one-stage gearbox $N = 5$ and two-stage gearbox $N = 25$. Four loads are selected with damping ranging from 4Γ to 32Γ where Γ is the driver motor quality factor.
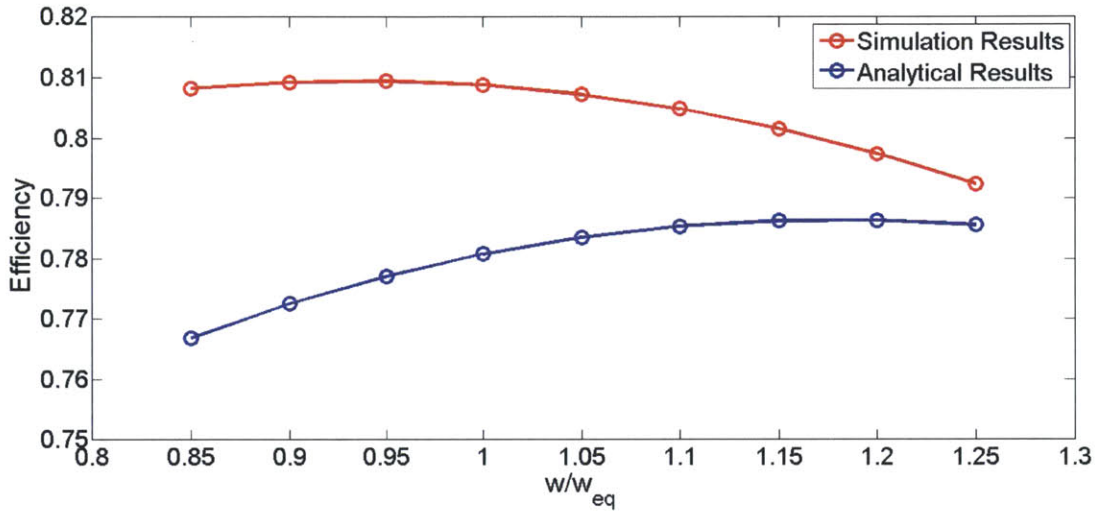
Figure 3-11: Plots of energy efficiency of the pulse gear drive with one-stage gearbox N = 5 and a load of 4Γ at different normalized pulse speeds w/w_{eq}. The simulation shows that the maximum efficiency 81% is achieved at $w = 0.95w_{eq}$ while the analytical derivation indicates that the maximum efficiency 79% is obtained at $w = 1.15w_{eq}$.

efficiency is obtained with $w = 0.95w_{eq}$, 15% lower than the analytically obtained optimal speed $w = 1.15w_{eq}$. The maximum efficiency in simulation is approximately 2% higher than the analytical calculations. Overall we consider that the simulation agrees with the analytical calculation and that the discrepancy is likely due to the combined results of the dynamics of the damper and the recovery energy of the spring.

Figure 3-12 summarizes the efficiency results for the pulse gear drive, the pulse direct drive and the conventional gear drive at different loads. For each set of data, the simulation efficiency matches the analytical calculations within a difference of about
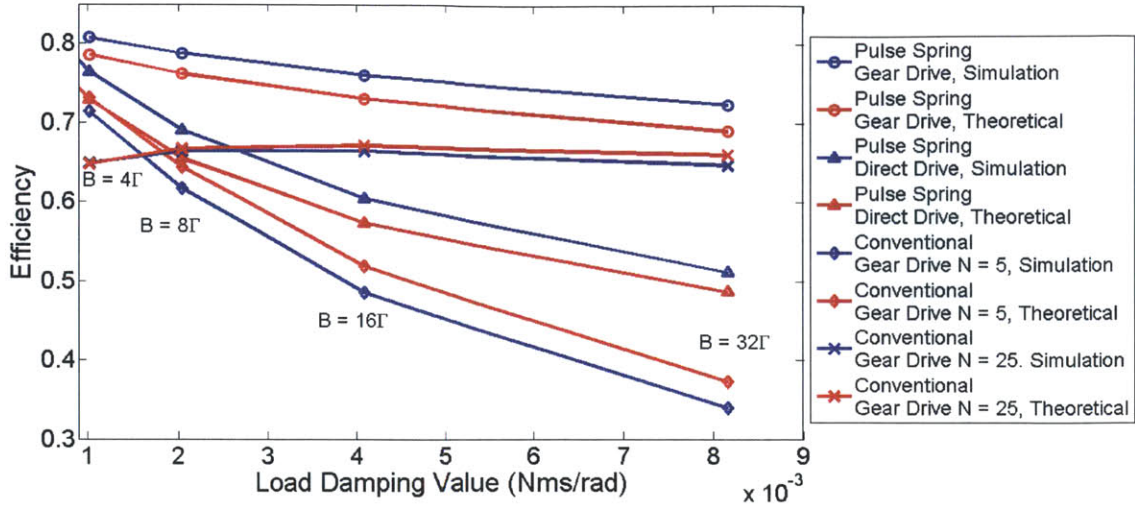
Figure 3-12: Plots of energy efficiency at different loads for the pulse direct drive, the pulse gear drive with one-stage gearbox $N = 5$, the conventional gear drive with one-stage gearbox $N = 5$ and the conventional gear drive with two-stage gearbox $N = 25$. For each set of data, the simulated results match with the analytical predictions within 3% in value. We observe that the pulse gear drive is the most efficient drive for all loads.

3% in value. For all load levels, the pulse gear drive has the highest efficiency. With the same one-stage gearbox, the pulse gear drive is only 6% more energy efficient than the conventional gear drive at the smallest load of $B = 4\Gamma$. But the efficiency gain increases with B. At $B = 32\Gamma$, the efficiency gain becomes as large as 35%. Similar to the case of no gearbox, the efficiency for the pulse gear drive drops at the rate of $\sqrt{B}$ whereas the efficiency for the conventional gear drive drops at the rate of B. It is also worth noting that the pulse direct drive efficiency is still slightly better than the one-stage conventional gear drive in all scenarios. However, in the cases with the second-stage gearbox, the efficiency of the conventional gear drive stays at almost a constant level of 66%, which is only 5% lower than the pulse gear drive efficiency at the highest load level.

3.3.6 Short Summary

We model and simulate the pulse drive process with a gearbox transmission added as well as the conventional gear drive process. The simulation results indicate that a one-

stage gearbox transmission is the best option for the pulse drive. It can achieve higher efficiency than the pulse direct drive. However, with the assumption made in this simulation, the pulse gear drive is only slightly more efficient than the conventional gear drive, as the conventional drive with one-stage gearbox is relatively efficient at lower load levels, and the conventional drive with a two-stage gearbox is relatively efficient at higher load levels.

3.4 Effects of Adding Crank-Shaft Transmission

3.4.1 Purpose of Adding Crank-Shaft Transmission

An important assumption we have made in previous sections is that we assume a perfect active latch mechanism which can hold the driver shaft without energy dissipation during the spring to output work cycle. However any form of active latch requires some supplied energy in the real world. In addition it will take extra effort to design such a latch and integrate it into the system. Thus we explore the possibility of designing a passive latch mechanism with no energy consumption. The crank-shaft transmission presented below is one possible design.

3.4.2 Modeling and Assumptions

Figure 3-13 is a schematic of the crank-shaft transmission design. The center of the crank arm is attached to the actuator shaft while the end point C is connected with the linear spring. At the lowest point C' and the highest point C''', the moment of the spring force on the crank arm is zero because the moment arm direction is aligned with the force direction, creating two passive kinematic latch points which we can take advantage of. At those two points, the spring force is carried solely by the motor/gear bearings. In a half work cycle, the crank arm is actuated rapidly from C' to C''', causing a rapid expansion of approximately $\Delta x_{in} = 2r$ in spring. In an ideal scenario, without actuating torque, the crank arm is self-latched by the servo motor at point C''' at which point the spring gradually drives the damper in the x direction.

To analyze the efficiency with the crank-shaft transmission, we make the following assumptions:

- The damper value is large enough so that it creates a significant phase lag to the rapid spring extension;
- The motor torque is proportional to the input current $T = K_t i$;
- The length of the spring is much larger than the length of the crank arm $L \gg r$, thus the spring angle relative to the vertical axis β is approximately zero;
- The spring is massless;
- The power loss in the actuator coil is the only source of energy loss;

3.4.3 Analytical Efficiency Expressions

In this analysis, a half period sinusoidal pulse displacement trajectory is applied to the actuator shaft

$$\theta = \frac{\pi}{2} - \frac{\pi}{2}\cos wt, \tag{3.28}$$

with velocity

$$\dot{\theta} = \frac{\pi}{2}w \sin wt, \tag{3.29}$$

and acceleration

$$\ddot{\theta} = \frac{\pi}{2}w^2 \cos wt. \tag{3.30}$$

The required torque is calculated from the equation of motion

$$T = K_t i = J_{in}\ddot{\theta} + k\Delta Lr \sin \alpha, \tag{3.31}$$

where ΔL is the change in spring length. We define x_{in} as the displacement of the projection of point C along the x axis. Thus x_{in} and θ have the following relation

$$x_{in} = r - r cos\theta. \tag{3.32}$$

59
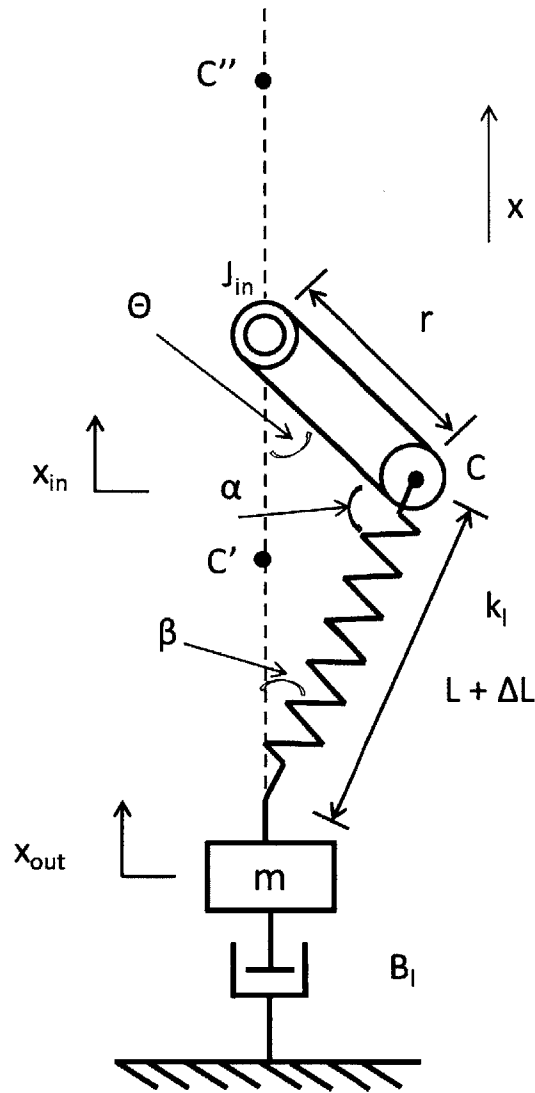
Figure 3-13: Schematic of the pulse drive with crank-shaft transmission. The lowest point C' and the highest point C'' are the two latch points where the moment of the spring force is zero. During the pulse phase, in a half cycle, the crank arm rotates rapidly from C' to C'', expanding the spring approximately $\Delta x_{in} = 2r$. Then the arm is self-locked by the servo motor at C''' and the spring transfers the energy into the load.

60

With the assumption of $L \gg r$, it is seen that $\beta \approx 0$ and $\alpha \approx \theta$. As a result we can assume $\Delta L \approx x_{in}$. By replacing ΔL with (3.32), the current has the following expression

$$i = \frac{1}{K_t}(J_{in}\ddot{\theta} + kx_{in}r\sin\theta). \tag{3.33}$$

The energy loss is calculated by integrating the power loss over the pulsing period

$$
\begin{aligned}
W_{loss} &= \int_0^{\frac{\pi}{w}} i^2 R \, dt = \frac{R}{K_t^2} \int_0^{\frac{\pi}{w}} (\frac{\pi}{2}J_{in}w^2\cos wt + k(r - r\cos\theta)r\sin\theta)^2 \, dt \\
&= \frac{R}{K_t^2}(\frac{\pi^3}{8}J_{in}{}^2w^3 - 0.4471\pi J_{in}wkr^2 + 1.3991\frac{k^2r^4}{w}).
\end{aligned}
\tag{3.34}
$$

The useful energy is given by the potential energy stored in the spring

$$W_{useful} = \frac{1}{2}k(2r)^2 = 2kr^2. \tag{3.35}$$

Therefore the fractional energy efficiency is calculated as

$$\eta = \frac{W_{useful}}{W_{loss} + W_{useful}} = \frac{1}{1 + \frac{R}{K_t^2}(1.938\frac{J^2w^3}{kr^2} - 0.702Jw + 0.700\frac{kr^2}{w})}. \tag{3.36}$$

Similar to (2.22) and (3.20), we calculate the global minimum of (3.36) and derive the optimal trajectory speed

$$w_{optimal} = 0.642\sqrt{\frac{k}{J_{in}}}r, \tag{3.37}$$

and the optimal efficiency

$$\eta_{optimal} = \frac{1}{1.15\frac{R}{K_t^2}\sqrt{kJ_{in}} + 1} = \frac{1}{\frac{1.15}{\Gamma}\sqrt{kJ_{in}} + 1}. \tag{3.38}$$

The efficiency expression is dependent on $\sqrt{k}$, $\sqrt{J_{in}}$ and $1/\Gamma$ which is quite similar to (2.26) which is the efficiency expression without the crank-shaft transmission. Thus adding the crank-shaft transmission does not alter the tradeoff among the spring, motor inertia and motor quality factor. In the next section we will simulate the

61
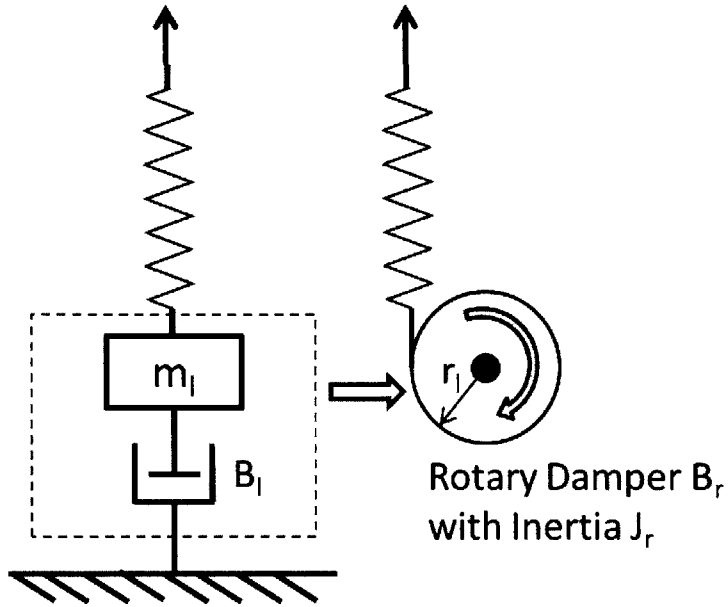
Figure 3-14: Rotary damper in a translational system. The linear damper B_l is modeled as a rotary damper B_r with a moment arm r_l.

efficiency and compare it to the efficiency of the pulse drive without transmission.

3.4.4 Simulation Results

Simulation Methodology

We modify the Simulink model shown in Figure 3-4 to simulate the dynamics of the pulse drive with the crank-shaft transmission. The driver motor is modeled with the same Maxon DC motor specifications used in Section 3.2. The length of the crank arm r is set to be 0.01 m. Since it is a translational system, we model the linear load damper B_l as a rotary damper B_r with a moment arm r_l, as shown Figure 3-14, so that it has the expression

$$B_l = \frac{B_r}{r_l^2}. \tag{3.39}$$

We choose the rotary damping B_r to have the same value as the driver motor quality factor Γ which resembles the case study of the pulse direct drive. To directly compare the pulse drive efficiency with and without the crank-shaft transmission, we need the driver motor and the load rotary damper to have the same peak displacement. In

Set	r (m)	r_l (m)	$w(\sqrt{k/J_{in}}r)$	k_l (N/m)	$\frac{L}{r}$	B_r	B_l (Ns/m)
1	0.01	0.0064	75% − 125%	156.3	10	Γ	6.23
2	0.01	0.0064	90%	156.3	1 − 100	Γ	6.23
3	0.01	0.0064	90%	27.1 − 217.1	10	$\Gamma − 8\Gamma$	6.23 − 49.80

Table 3.6: Simulation parameters for the pulse drive with a crank-shaft transmission. Three sets of experiment are carried out to study the effects of pulse speed, the $\frac{L}{r}$ ratio, and load damping on overall energy efficiency.

this case with the crank-shaft transmission, the driver motor's peak displacement is π radians and the linear damper's peak displacement is $2r$ where r is the radius of the crank shaft as shown in Figure 3-13. As a result, we need the peak rotary displacement of the rotary damper $r_{load} \times \pi$ to match $2r$. Thus r_l is calculated as

$$r_l = \frac{2r}{\pi} = 0.0064 \text{ m}. \tag{3.40}$$

Three sets of simulations are carried out. The first set is to verify the relation between the efficiency and the pulse speed. The pulse speed is varied from $75\% w_{optimal}$ to $125\% w_{optimal}$ in which $w_{optimal}$ is given by (3.37). The second set is to investigate the effects of varying the ratio $\frac{L}{r}$ on efficiency since we have made the assumption of $L \gg r$ for efficiency derivation. The third set is to compare the efficiency of the crank-shaft transmission to the efficiency of no transmission with the same load amplitude and power level conditions. The simulation parameters are summarized in Table 3.6.

Effects of Pulse Speed and $\frac{L}{r}$ Ratio

Figure 3-15 shows the efficiency results at different pulse speeds. Overall the simulation results agree well with the theoretical results. The simulation indicates a peak efficiency of 82.7% at $w = 0.57\sqrt{\frac{k}{J_{in}}}r$ which are 105% and 90% of the analytical predictions, respectively. Similar to the case without the crank-shaft transmission, we believe the difference to be from the dynamics of the damper and the recovery energy in the spring. Figure 3-16 shows the efficiency results at different $\frac{L}{r}$ ratios at the simulated optimal pulse speed. The efficiency remains almost the same with
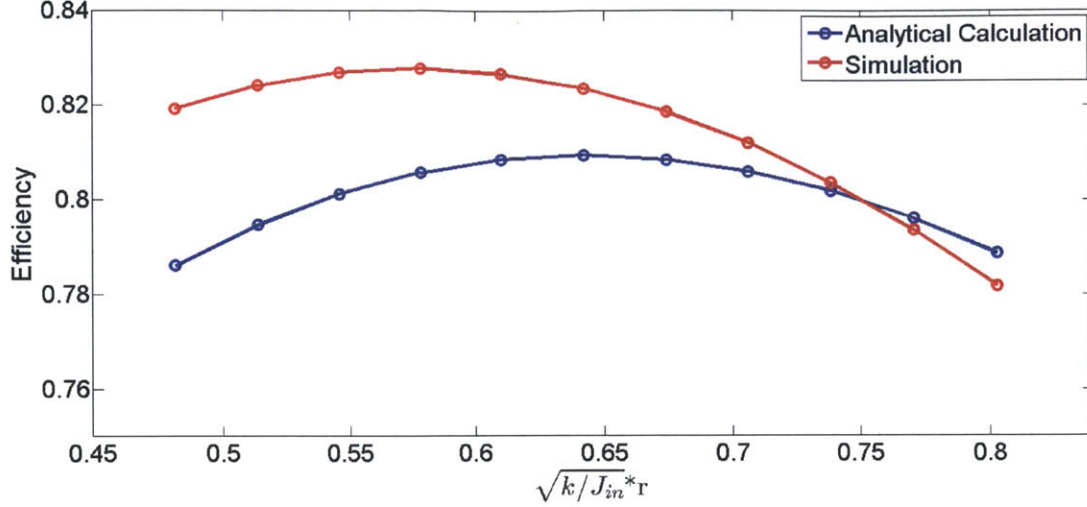
Figure 3-15: Plots of energy efficiency of pulse drive with crank-shaft transmission at different pulse speed. The maximum efficiency by simulation is 82.7% at $w = 0.57\sqrt{\frac{k}{J_{in}}}r$. The maximum efficiency by analytical derivation is 81.8% at $w = 0.64\sqrt{\frac{k}{J_{in}}}r$.

the ratio beyond 2. At the ratio of 1, the simulated efficiency only drops by 2.3%. Therefore, we conclude from the first and second sets of experiments that even with the assumption of $L \gg r$, (3.37) is sufficient to predict the efficiency of the pulse drive with crank-shaft transmission.

Efficiency Comparison and Discussion

We simulate the pulse drive process both with the crank-shaft transmission in Figure 3-13 and without the transmission in Figure 3-1 at the four load damper values described in Section 3.2.4. The driver amplitude for no-transmission pulse drive is chosen as π in order to match the crank-shaft transmission case. The load displacement profiles for the two cases are almost identical, as shown in Figure 3-17, indicating that we can compare the efficiency results directly. As seen from Figure 3-18, the efficiency with crank-shaft transmission are consistently lower, from 4.5% lower at $B = \Gamma$ to 6.5% lower at $B = 8\Gamma$. To qualitatively understand the cause for the drop in efficiency, we analyze the simulated current, voltage and power in both cases with $B = \Gamma$ (Figure 3-19) and discover two possible causes. The root-mean-square current
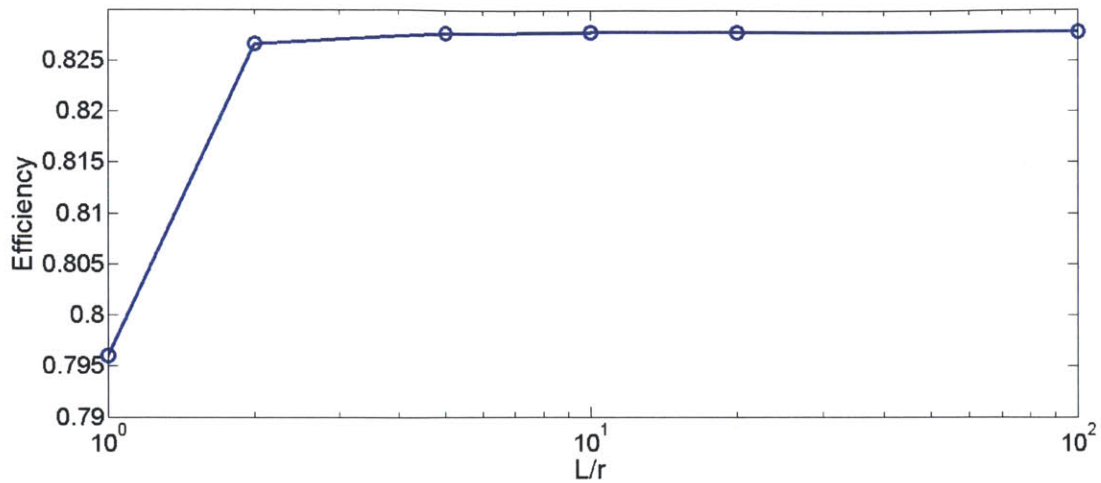
Figure 3-16: Plots of simulated energy efficiency of pulse drive with crank-shaft transmission at different L/r ratios. The efficiency remains almost the same with the ratio beyond 2. At the ratio of 1, the simulated efficiency only drops by 2.3%.

for the crank-shaft transmission case is 0.0184 A, 20% higher than 0.0153 A for the no transmission case, meaning that adding a crank-shaft transmission increases the torque level required to deliver the same amount of energy, and thus increases the resistive heat dissipation. It is also noticed that braking current is present with the crank-shaft transmission case, indicating that the torque by the linear spring at the end of the pulse is insufficient to slow down the motor inertia. Even though we count the recovered kinetic energy as useful energy, the additional negative current input leads to extra resistive heat loss.

3.4.5 Short Summary

We model and analyze a crank-shaft transmission design for the pulse drive. The simulation efficiency results confirm the analytical modeling. The crank-shaft transmission efficiencies are then compared to the no transmission efficiencies at the same load amplitude and power level. Even though adding such transmission lowers the efficiency because of a higher torque level and additional breaking current, such design has the advantage of a passive latch mechanism which eliminates the need for a separate latch. In addition, if we count the energy loss on a separate latch mechanism,
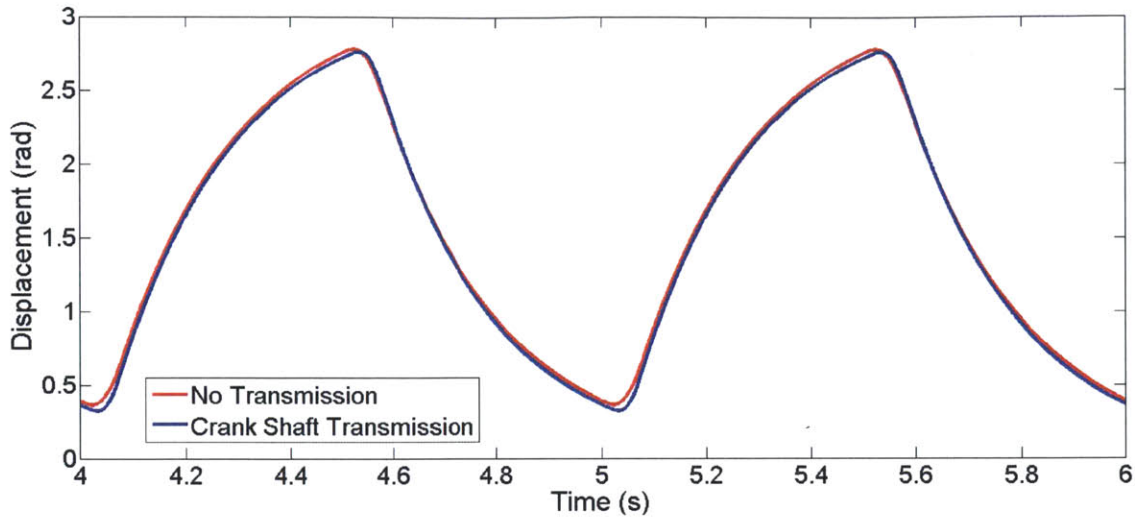
Figure 3-17: Plots of the pulse drive load displacement for the two cases. Similar displacement can be achieved with the addition of the crank-shaft transmission compared to the pulse drive without transmission.
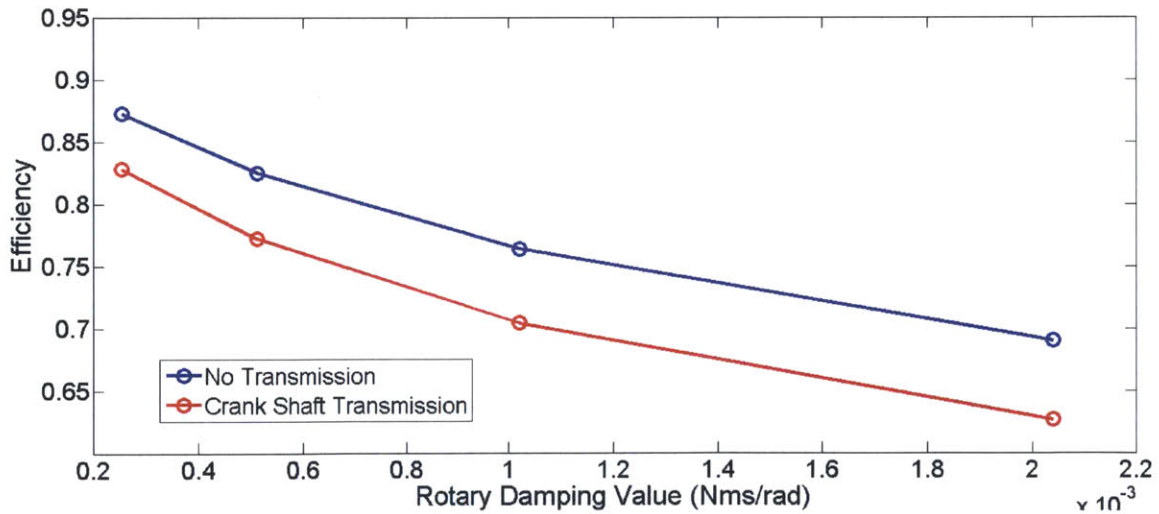
Figure 3-18: Plots of the energy efficiency for the pulse drive with and without a crank-shaft transmission at different loads. The drive without the transmission is consistently more efficient than the drive with transmission for the selected profiles.
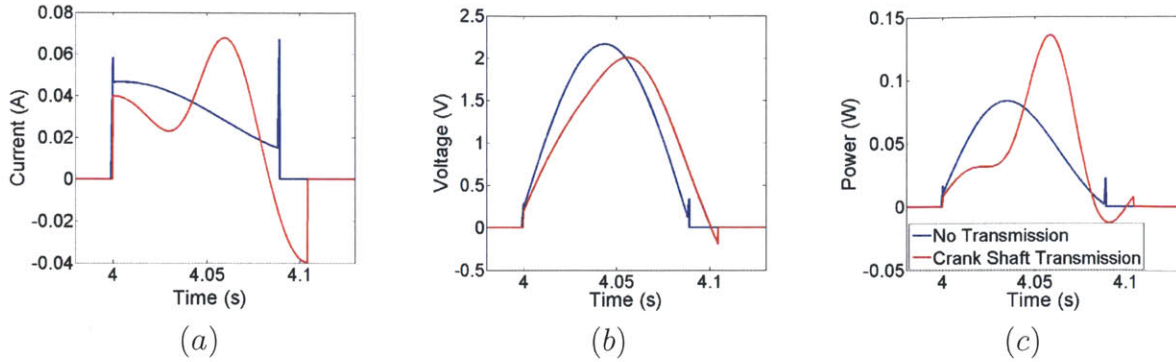
Figure 3-19: Plots of (a) current, (b) voltage and (c) power for the pulse drive with and without a crank-shaft transmission at the same load. The maximum current and voltage are similar for the two drives. However, negative braking current is observed in drive with a crank-shaft transmission which leads to additional energy dissipation. The maximum power of the drive with a crank-shaft transmission is almost twice as high as the drive without the transmission.

the two cases may have equivalent efficiencies. Also, other trajectory profiles may increase the efficiency. However, within the time frame of this thesis, we don't have a chance to construct any hardware demonstration with the crank-shaft transmission.

3.5 Exploration of Different Trajectory/Force Profiles

3.5.1 Overview

In previous sections, we have calculated the efficiency with the assumption that the driver motor is given a half sinusoidal position pulse trajectory. In this section, we briefly explore the effects on efficiencies by using different trajectory and force(torque) profiles to see if a more optimal trajectory might be more efficient.

3.5.2 Pulse Drive with Shorter Pulse Force

In this section, we analyze the simple translational spring-inertia system with the scenario in which a step force F is applied for Δt seconds and then ceases before the inertia reaches its maximum displacement. A quick force and displacement plot is

67
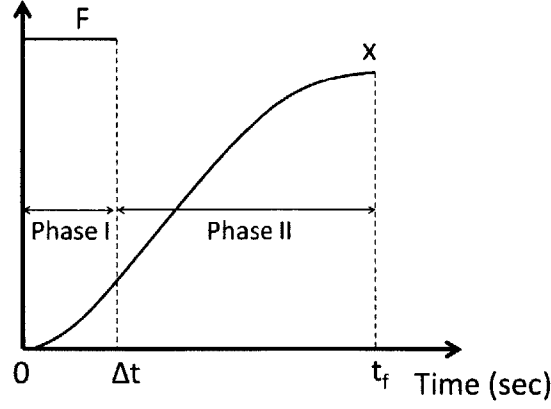
Figure 3-20: Force and displacement trajectory schematic for the pulse drive with shorter pulse torque.

shown in Figure 3-20. The dynamics for Phase I is

$$m\ddot{x} + kx = F, \tag{3.41}$$

and for phase II is

$$m\ddot{x} + kx = 0. \tag{3.42}$$

By applying the continuity of position and velocity, we derive the expression for final time t_f in terms of the force applying period Δt

$$t_f = \Delta t + \frac{1}{w_n} \sin^{-1}\left(\frac{\sin(w_n \Delta t)}{\sqrt{2(1 - \cos(w_n \Delta t))}}\right). \tag{3.43}$$

Here w_n is the natural frequency defined by $\sqrt{k/m}$. The maximum value of t_f is π/w_n with $\Delta t = \pi/w_n$ in which case the inertia goes through a regular half sinusoidal trajectory. The minimum value of t_f is $\pi/2w_n$ with $\Delta t \to 0$ in which case the inertia goes through a quarter sinusoidal trajectory with a pulse velocity input. Thus the total pulse period is bounded between $\pi/2w_n$ and π/w_n. The fractional energy
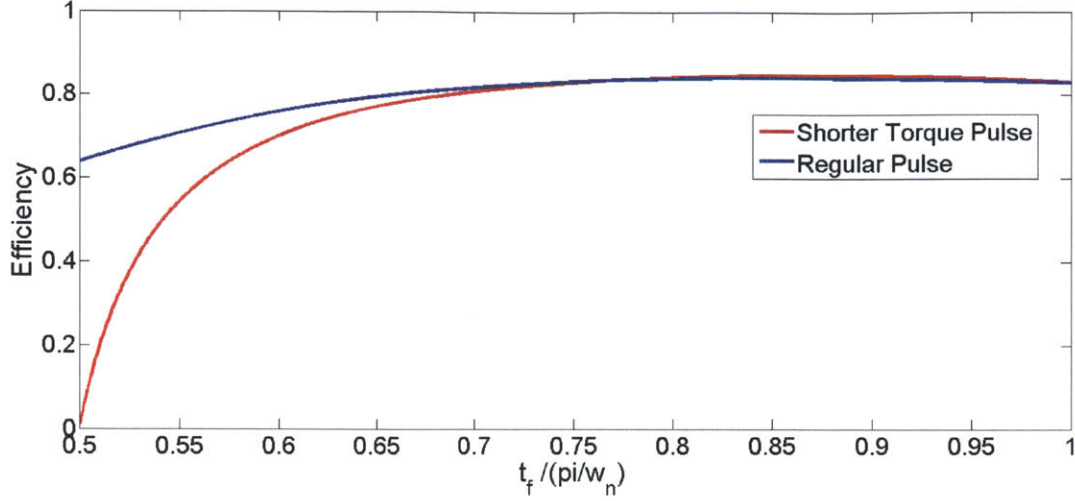
Figure 3-21: Plots of energy efficiency at different normalized pulse period $\frac{t_f}{\pi/w_n}$ for the pulse drive with a shorter pulse force and the pulse drive with a regular displacement pulse. Pulse drive with a shorter pulse force shows no significant improvement on efficiency in which its maximum efficiency is 84.78% at $t_f = 0.87\pi/w_n$ compared to 84.28% at $0.85\pi/w_n$ for the regular pulse drive.

efficiency expression is also derived in terms of Δt

$$\eta = \frac{\frac{1}{2}kA^2}{(\frac{F}{K_f})^2 R\Delta t + \frac{1}{2}kA^2} = \frac{\frac{F^2}{k}(1 - \cos(w_n\Delta t))}{\frac{F^2 R\Delta t}{K_f^2} + \frac{F^2}{k}(1 - \cos(w_n\Delta t))}$$
$$= \frac{1}{\frac{k\Delta t}{\Gamma(1-\cos(w_n\Delta t))} + 1}. \tag{3.44}$$

We compare the efficiency described in (3.44) to the efficiency in (2.22) using the Maxon 118745 DC motor specifications as a reference and plot the efficiency values on the same graph (Figure 3-21). The efficiency with shorter force period reaches a maximum value of 84.78% at $t_f = 0.87\pi/w_n$ and $\Delta t = 0.74\pi/w_n$ while the efficiency with a regular displacement pulse has a maximum value of 84.28% at $0.85\pi/w_n$. As a result, we conclude that the efficiency gain brought by applying a shorter force(torque) period is negligible and the efficiency value is very sensitive to Δt. Thus the regular displacement pulse is preferable.

69
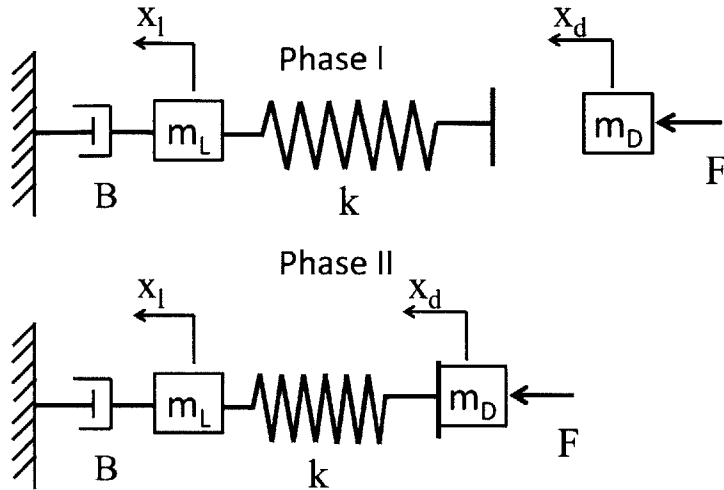
Figure 3-22: Schematic of the deadzone drive. During Phase I, the mass is detached from the spring and accelerated alone. During Phase II, the mass hits the spring and they travel together until the velocity decreases to zero.

3.5.3   Exploration of a Deadzone Pulse Drive

Description of the Deadzone Pulse Drive

In the fundamental tradeoff analysis, we show that it is the inertia that limits the energy transfer efficiency and pulse time. In this section, we provide a solution in theory seeking to break this tradeoff and minimize the effects of inertia. Such a solution is named the *deadzone pulse drive* which we store the energy in the inertia first, then transfer the energy into the spring. As shown in Figure 3-22, during Phase I of the pulse period, the mass is detached from the spring and accelerated alone. During Phase II, the mass hits the spring and they travel together until the velocity decreases to zero. Since the spring is assumed massless, we assume that no energy loss occurs during the collision, although this assumption will be challenging in real hardware. With such a deadzone drive, we are able to improve the efficiency of "charging" the inertia without harming the efficiency of "charging" the spring by accelerating the inertia over a longer period in Phase I.

70

Modeling and Analytical Expressions

We assume that the same constant force $F = K_f i$ is applied to m_d for both Phase I and Phase II. With the assumption of $x_l \approx 0$, the resulting trajectory $x_d(t)$ is parabolic in Phase I and sinusoidal in Phase II

$$x_{d1}(t) = 0.5 \frac{F}{m_d} t^2, \tag{3.45}$$

$$x_{d2}(t) = A \sin(w_n t) + B \cos(w_n t) + C, \tag{3.46}$$

where w_n is the natural frequency defined by $\sqrt{k/m_d}$ and A, B and C are generic constants. We define the following parameters in order to calculate the efficiency

x_1 is the total driver displacement during Phase I,

x_2 is the total driver displacement during Phase II,

t_1 is the pulse time during Phase I,

t_2 is the pulse time during Phase II,

n is the displacement ratio x_{d2}/x_{d1}.

We assume the coil resistive loss is the only source of energy loss and the energy stored in the spring is the useful work

$$W_{loss} = (\frac{F}{K_f})^2 R(t_2 + t_1), \tag{3.47}$$

$$W_{useful} = \frac{1}{2} k x_2^2. \tag{3.48}$$

As a result, the fractional energy efficiency is

$$\eta_{deadzone} = \frac{W_{useful}}{W_{useful} + W_{loss}} = \frac{1}{\frac{2RF(t_1+t_2)}{K_f^2 k x_2^2} + 1} \tag{3.49}$$

Note this equation contains several variables t_1, t_2, F, and x_2. However, we are able to reduce the number of variables and express t_1, t_2 and F in terms of n and x_2 and by taking the following algebraic transformations. Using the trajectory equation in Phase I, t_1 can be expressed as $\sqrt{2x_d m_d/F}$. Since all the work done by F is

71

transferred to spring potential energy $F(x_1 + x_2) = \frac{1}{2}kx_2^2$, F can be written as

$$F = \frac{kn}{2(n+1)}x_2 \tag{3.50}$$

Thus t_1 is further written as

$$t_1 = \sqrt{2x_d m_d / F} = \frac{2}{w_n}\sqrt{\frac{n+1}{n^2}}. \tag{3.51}$$

By applying displacement and velocity continuity at the instant of collision and energy conservation in Phase II

$$x_{d1}(t_1) = 0.5\frac{F}{m_d}t_1^2 = x_{d2}(0) = B + C, \tag{3.52}$$

$$\dot{x}_{d1}(t_1) = \frac{F}{m_d}t_1 = \dot{x}_{d2}(0) = Aw_n, \tag{3.53}$$

$$\frac{1}{2}m_d\dot{x}_{d1}(t_1)^2 = \frac{1}{2}kx_{d2}(t_2)^2 - Fx_{d2}(t_2) = \frac{1}{2}k(A^2 + B^2) - F\sqrt{A^2 + B^2}, \tag{3.54}$$

we are able to solve A, B and C in terms of F, t_1, and t_2, and $x_{d2}(t)$ becomes

$$x_{d2}(t) = \frac{Ft_1}{m_d w_n}\sin w_n t - \frac{F}{k}\cos w_n t + \frac{F}{k} + \frac{Ft_1^2}{2m_d}. \tag{3.55}$$

Next we obtain a relationship between t_1 and t_2 by setting $\dot{x}_{d2}(t_2) = 0$

$$\dot{x}_{d2}(t_2) = \frac{Ft_1}{m_d}\cos w_n t_2 + \frac{F}{k}w_n \sin w_n t_1 = 0. \tag{3.56}$$

By substituting (3.51) into (3.56) and simplifying the equation, we can express t_2 in terms of n

$$t_2 = \frac{1}{w_n}(\pi - \tan^{-1}(2\sqrt{\frac{n+1}{n^2}})). \tag{3.57}$$

72

As a final step, we substitute (3.50), (3.51) and (3.57) into (3.49) and obtain the deadzone drive efficiency with n as the only variable

$$\eta_{deadzone} = \frac{1}{\frac{R\sqrt{km_d}n^2}{2K_f^2(n+1)^2}(\pi - \tan^{-1}(2\sqrt{\frac{n+1}{n^2}}) + 2\sqrt{\frac{n+1}{n^2}}) + 1}. \tag{3.58}$$

We perform three quick validation checks for this complicated efficiency expression. First we set $n \to \infty$ so that Phase I displacement is zero and it becomes the regular pulse drive case. The resulting efficiency expression $\eta = \frac{1}{\frac{\pi R}{2K_f^2}\sqrt{km_d}+1}$ is identical to (2.22) with $w = w_n$. Second we set $n \to 0$ so that $t_1 \to \infty$ and $t_2 \to \pi/2$. We expect a unity efficiency because the mass is accelerated over an infinite amount of time. Indeed, the efficiency expression renders 1 with $n \to 0$. Thirdly we count the order of n and observe that $\eta_{deadzone}$ approximately increases on the order of $1/n$, implying that more displacement in Phase I can result in better efficiency.

For the case with a gearbox transmission, we derive the deadzone pulse drive efficiency in the same approach described above with a gearbox reduction ratio N and a constant gearbox efficiency η_g as

$$\eta_{deadzone,geardrive} = \frac{1}{\frac{R\sqrt{km_d}n^2}{2K_f^2N(n+1)^2(\sqrt{\eta_g})^3}(\pi - \tan^{-1}(2\sqrt{\frac{n+1}{n^2}}) + 2\sqrt{\frac{n+1}{n^2}}) + \frac{1}{\eta_g}}. \tag{3.59}$$

We also check the validity of (3.59). As $n \to \infty$, the efficiency expression is

$$\eta = \frac{1}{\frac{\pi R}{2K_f^2N(\sqrt{\eta_g})^3}\sqrt{km_d} + \frac{1}{\eta_g}}, \tag{3.60}$$

which is identical to (3.20) with $w = w_n$. As $n \to 0$, the efficiency becomes η_g where the energy loss due to actuator coil resistance approaches zero and the efficiency is bounded by the gearbox efficiency.

Case Study on Efficiency Gain

We study the same case described in Section 3.2.4 without any transmission. The theoretical efficiencies and the corresponding pulse time at different n are calculated

73

using (3.59) and plotted in Matlab. As can be seen from Figure 3-23, the efficiency agrees with the regular pulse direct drive efficiency at $n \to \infty$. The efficiency approaches unity and $t_{pulse} \to \infty$ as $n \to 0$. Two specific examples and are given to shown the advantage by implementing the deadzone drive. Within the pulse time constraint of robotic fish tail propulsion $t_{pulse} < 0.2$ s which we define in Section 3.3.5, The efficiency can reach 92.5% at $n = 1$ with $t_{pulse} = 0.14$ s. In addition, we notice from Figure 3-23 that the increase in pulse time is due to the longer mass acceleration phase. If we can design a mechanism that allows the mass to accelerate at the same time when the spring transfers energy to the load, we may have longer pulse period without impacting the achievable cycle time. For example, we achieve an efficiency of 99% at $n = 0.1$ with $t_{pulse} = 0.7$ s.

However, the deadzone drive has several challenges. The biggest challenge is in the design of the catch-and-release mechanism between the inertia and the spring. On one hand, a passive element is preferred in the mechanism to minimize additional energy consumption. On the other hand, the inertia should be kept low because any added inertia at the spring will increase the energy loss during the catch. Another challenge is to properly control the timing of each phase and ensure the reliability of the system. Any deviation from the synchronization, such as the inertia starting to accelerate before being released, could lead to additional energy loss and potential damage to the system.

As a short conclusion, we show through theoretical analysis that deadzone drive can further increase the efficiency. However, due to the time constraint of the thesis, we haven't designed any hardware to demonstrate its feasibility. Nevertheless, we envision the deadzone drive to be a good topic for future work.

3.6   Summary of the Chapter

- A simulation case study on comparing the efficiency of the pulse direct drive and the conventional direct drive shows that the pulse direct drive significantly improves the propulsion efficiency.

74
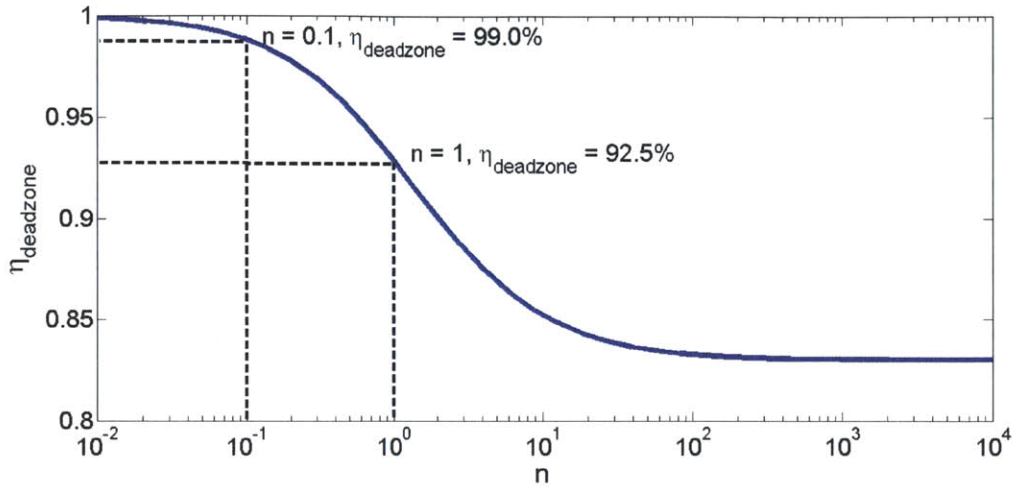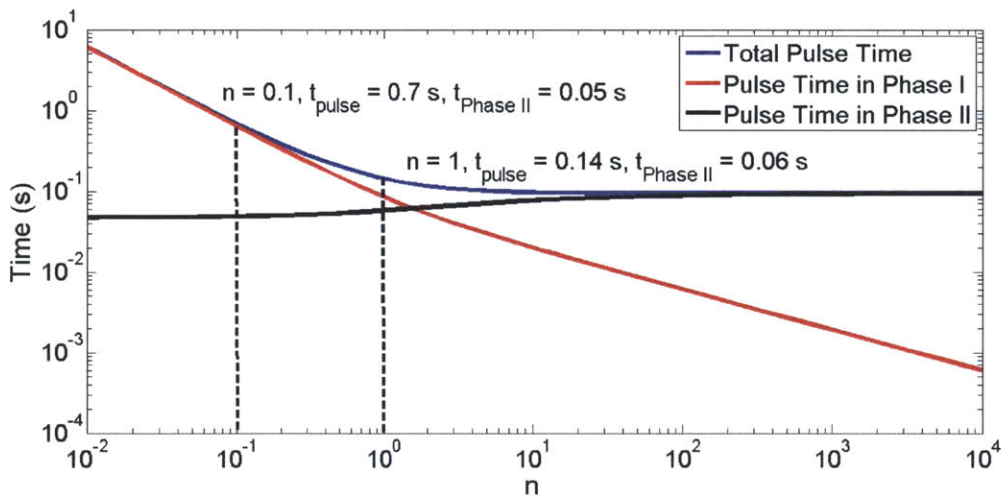
Figure 3-23: Plots of (a) calculated efficiency and (b) pulse time of the deadzone drive. As n, which is the ratio between displacement in Phase II and displacement in Phase I, gets smaller, both the efficiency and the pulse time increase. With $n \to 0$, efficiency approaches unity and pulse time approaches infinity. With $n \to \infty$, efficiency and pulse time agree with the regular pulse drive. The pulse time plots show that the increase in pulse time is due to the increase time in accelerating the mass in Phase I.

- By adding a gearbox transmission to the pulse drive, we conclude from the simulation that a one-stage gearbox transmission is the best option for the pulse drive. The corresponding efficiency is higher than the conventional gear drive even with higher gear reduction ratios.

- We can add a crank-shaft transmission to create a passive latch mechanism. However, such a design slightly lowers the pulse drive efficiency.

- We present a deadzone pulse drive concept and our theoretical analysis shows that the efficiency can be further improved.

Chapter 4

Hardware Demonstration of the Pulse Drive with Direct Connection

4.1 Design Concept

Motivated by the promising simulation results presented in Table 3.3, we constructed a quick hardware demonstration to validate the efficiency results for both the pulse direct drive and the conventional direct drive. The chosen design is a test-stand using two permanent magnet DC brushed motors in which one motor acts as the driver and the other as a viscous load. The driver motor is driven by a linear power amplifier circuit. The driver motor has its electrical terminals shorted and thus acts as a damper. Figure 4-1 shows the schematic of the pulse direct drive configuration with a spring connection and Figure 4-2 shows the schematic of the conventional direct drive configuration with a rigid bar connection. The idea of using DC brushed motor as a viscous load was suggested by Professor Trumper. As the two terminals of a DC brushed motor's are short circuited, turning the motor shaft would generate an opposing damping torque proportional to its angular speed. The damping value is equal to the motor quality factor $\Gamma = \frac{K_t^2}{R}$.
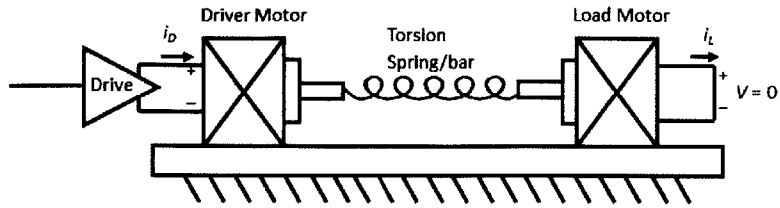
Figure 4-1: Schematic of the pulse drive. Shorted motor is used as a viscous load.
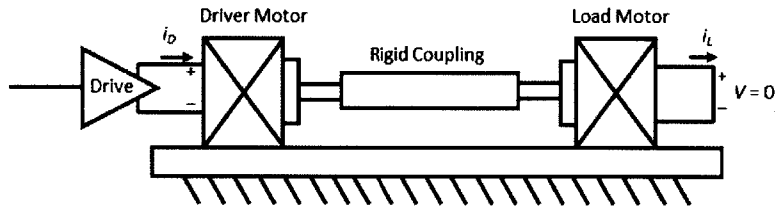
Figure 4-2: Schematic of the conventional direct drive. Spring is replaced with a rigid bar.

4.2   Instrumentation and Measurements

A picture of the constructed two-motor test-stand is shown in Figure 4-3. The two motors are identical Maxon 118745 DC brushed motors. The two motors are mounted on a machined aluminum fixture with their shaft axes aligned. The left motor is the driver motor that is driven by a linear current amplifier. The right motor is the load "damper" motor with its coil short circuited. Both motors are integrated with a optical quadrature encoder of 1024 pulses at the back end of the shaft for position measurement and both motor circuits include a series power resistor of 0.1 Ω for current sensing. A coil spring under tension is connected between the two motor shafts through flexible shaft couplings. The torsional spring constant K_θ in the unit of Nm/rad is calculated from the established equation from the Spring Design Manual by the Society of Automative Engineers [18] (Page 175),

$$K_\theta = \frac{Ed^4}{64Dn} \tag{4.1}$$

Where

E - Young's Modulus of the spring material;

78
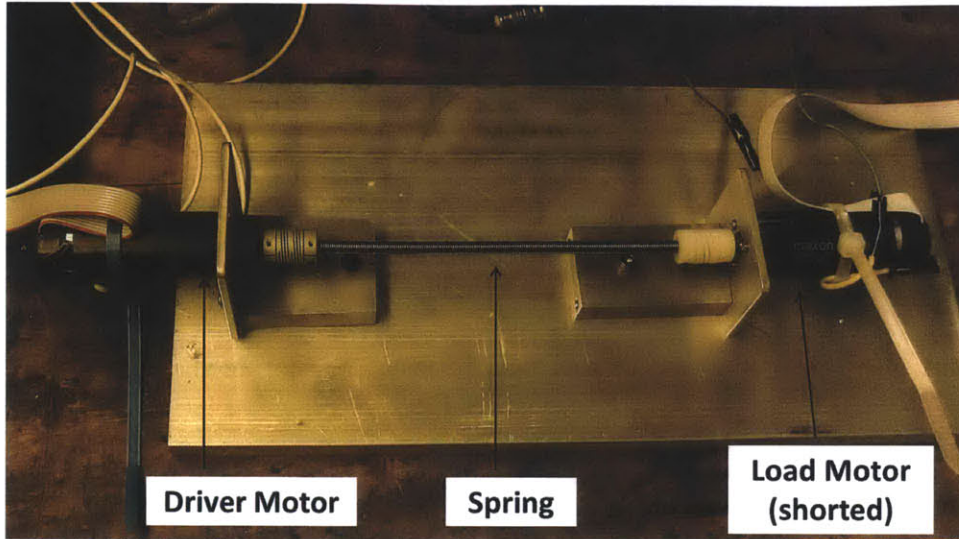
Figure 4-3: Picture of the pulse direct drive hardware demonstration. Two identical Maxon RE 25 permanent magnet motors are used with the left motor being the driver motor and the right motor with terminal short circuited as the viscous load.

d - Coil diameter;

D - Spring diameter;

n - Number of active coils.

In this case, the chosen coil spring has a torsional spring constant of 0.0011 Nm/rad with spring diameter of 4.5 mm, coil diameter of 0.71 mm and 173 active coils. The resulting resonance frequency between the spring and the driver motor shaft is 33 rad/s. The latch mechanism is not designed in this demonstration; instead we simulate the latch by holding the driver motor shaft at a fixed position under closed-loop position control. During this phase, we ignore the resulting power dissipation.

To actuate the driver shaft with the desired displacement trajectory, a position feedback control loop is constructed (Figure 4-4), which consists of a National Instruments PXI Chassis, an analog current control circuit and a linear power amplifier circuit. The digital control task is performed by the National Instruments PXI-8133e real time target with a sampling rate of 10 kHz and the voltage input/output task is carried out by a National Instruments PXI-6259 data acquisition board. The corresponding LabView Virtual Instruments(VI) can be found in Appendix B. By using an HP35665 dynamic signal analyzer, the crossover frequency of the overall position control loop
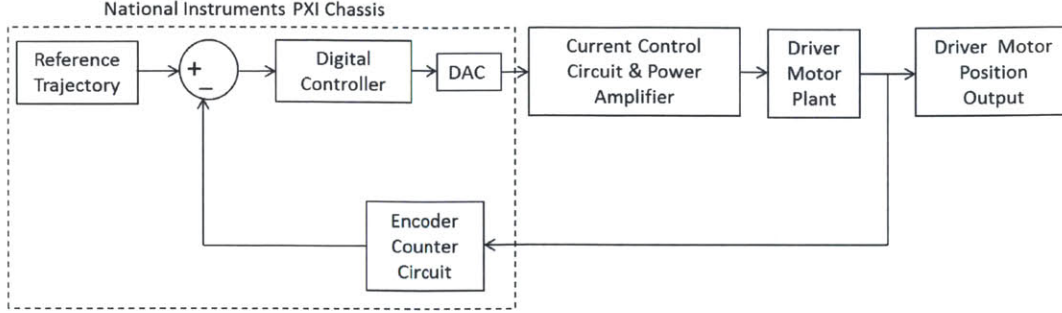
Figure 4-4: Block diagram of the driver motor position feedback control loop.
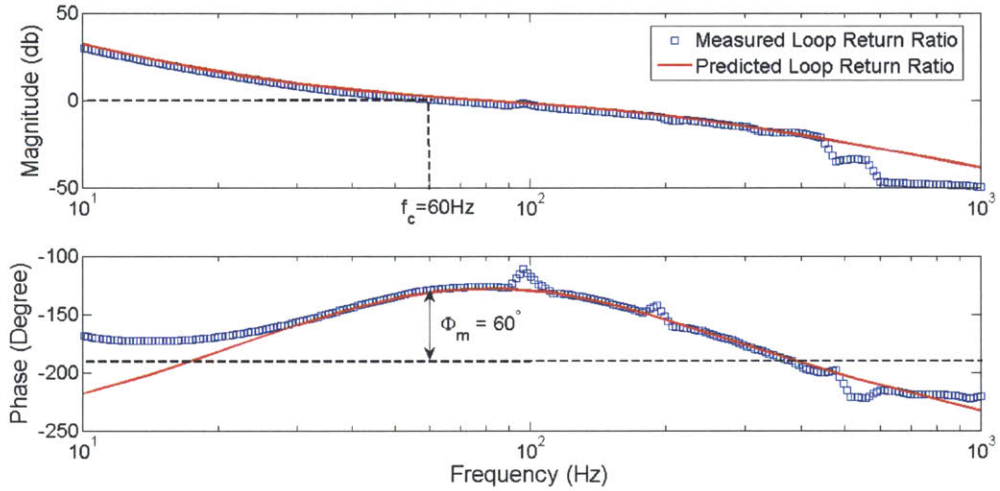
Figure 4-5: Measured and modeled loop return ratio of position control loop of the driver motor. The crossover frequency f_c is 60 Hz and the phase margin ϕ_m is 60 degrees which are sufficient for the pulse drive operation.

return ratio is measured to be approximately 60 Hz with a phase margin of 60 degrees, as shown in Figure 4-5. Note that the crossover frequency is 4 times higher than the natural frequency of the spring and the driver motor's inertia. In order to actuate the DC motor in the torque mode, a current control analog circuit is designed and implemented with a linear power amplifier to follow the voltage command from the digital controller (Figure 4-6). The current is sensed by measuring the voltage across the 0.1 Ω power resistor in series with the motor $V_{sense}/i = 0.1$ V/A. In the diagram, the first operational amplifier circuit is a summing junction for calculating the error between the reference voltage and the measured voltage. The second operational amplifier circuit is an inverting lag filter with a transfer function of $\frac{10000s+1}{5000s}$
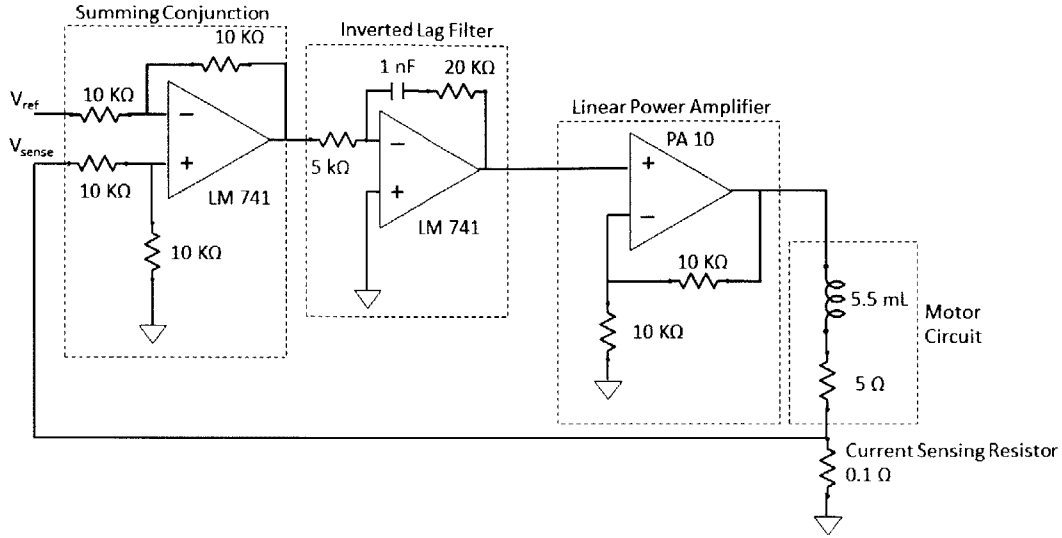
Figure 4-6: Diagram of driver motor current feedback control loop. The first operational amplifier circuit is a summing junction for calculating the error between the reference voltage and the measured voltage. The second operational amplifier circuit is an inverting lag filter implemented to reject disturbances. The linear power amplifier has a closed-loop DC gain of 2 and a bandwidth around 1 MHz to provide sufficient motor power. The current control loop has a crossover frequency of 6800 rad/s and a phase margin of 60 degrees.

implemented to reject disturbances. The linear power amplifier is an existing design by Dr. Imani Nejad of our lab, which has a closed-loop DC gain of 2 and a bandwidth around 1 MHz. The current feedback control loop return ratio achieves a crossover frequency at approximately 6800 rad/s with a phase margin over 60 degrees and a closed-loop DC gain of 0.1 A/V, which is sufficient for the motor operation in this demonstration. The electrical connection diagram is shown in Figure 4-7. The driver motor terminal voltage V_d, driver motor current sensing resistor voltage V_{ds}, load motor current sensing resistor voltage V_{ls} and two encoder signals are monitored by three analog voltage input channels and two digital counters. Thus the instantaneous power consumption on the driver motor is calculated as $P_{driver} = \frac{V_d V_{ds}}{R_{sensor}}$ and power consumption on the load motor is $P_{load} = \frac{V_{ls}^2}{R_{sensor}}$. The energy is then calculated by

81
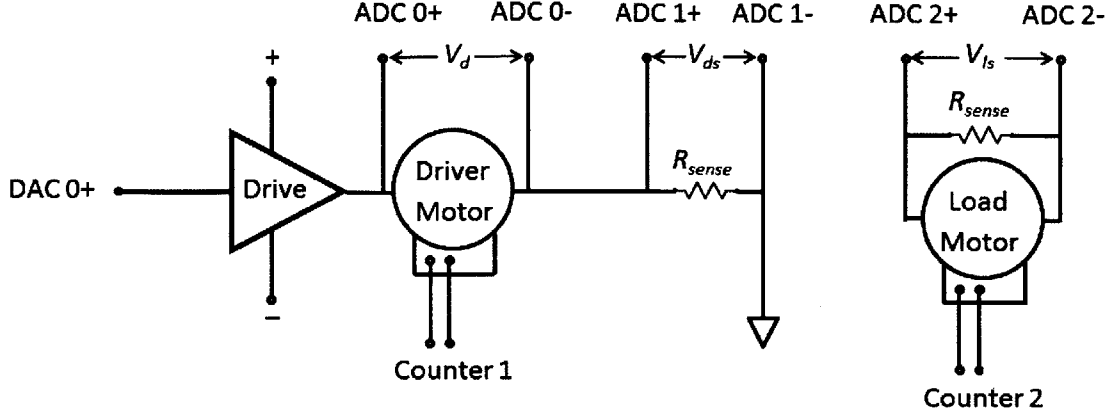
Figure 4-7: Electrical connections for voltage, current and position measurements. The driver motor terminal voltage V_d, driver motor current sensing resistor voltage V_{ds} and load motor current sensing resistor voltage V_{ls} are measured by three differential analog-to-digital converter (ADC) input channels. The position encoder signals of the driver motor and the load motor are read by two digital counters. The control voltage is output from a digital-to-analog converter (DAC) output channel.

numerically integrating the power over time

$$E_{driver} = \int P_{driver}dt = \int \frac{V_d V_{ds}}{R_{sensor}}dt, \tag{4.2}$$

$$E_{load} = \int P_{load}dt = \frac{V_{ls}^2}{R_{sensor}}dt. \tag{4.3}$$

Therefore the fractional energy efficiency is the ratio between the two $\eta_{measured} = \frac{E_{driver}}{E_{Load}}$. However, we purposely exclude the power dissipation on the driver motor when its shaft position is held constant to simulate the latch condition. Thus this portion is not included in the efficiency calculation because we envision that an energy efficient latch mechanism will replace the control current in real applications.

Seven sets of experiments with different driver motor amplitudes are carried out for both the pulse direct drive and the conventional direct drive. The trajectory profiles described in (2.16) and (3.6) are implemented for the two drives, respectively. The details of the experiments are summarized in Table 4.1. In each experiment, measurement data are saved for 10 cycles and the efficiency results are calculated with the total energy on the load and the driver (excluding simulated latch) during

the entire period. For each amplitude level, two experiments are repeated to get an averaged efficiency value.

Experiments	w (rad/s)	A_{driver} (radians)	w_{cycle} (rad/s)
1	38	$\pi/2$	1.1π
2	38	$3\pi/4$	1.1π
3	38	π	1.1π
4	38	$5\pi/4$	1.1π
5	38	$3\pi/2$	1.1π
6	38	$7\pi/4$	1.1π
7	38	2π	1.1π

Table 4.1: Experiment parameters of the hardware demonstration. Seven experiments are carried out with driver amplitudes ranging from $\pi/2$ radians to 2π radians for both the pulse direct drive and the conventional direct drive.

4.3 Results and Discussion

4.3.1 Energy Efficiency Comparison

The efficiency results for the seven sets of experiments are summarized in Figure 4-8 in which the efficiencies are compared in terms of load amplitude and cycle power level. The figure also included the simulation results under the same condition with a dry friction model which we will discuss in Section4.3.3. For all seven sets of experiment, the experiment results agree well with the simulation results in which the efficiencies of the pulse drive are demonstrated to be higher than the conventional direct drive, from 25% higher at the lowest power level to 30% higher at the highest power level. However, the efficiency values for both cases are consistently lower than the theoretical values, believed to be due to the presence of friction in the motor brush. The effects of friction is explored further in section 4.3.3.

4.3.2 Driver Power, Voltage and Current Comparison

Another important factor usually involved in choosing the right motor drives is the instantaneous current, voltage and power level. Thus we compare the three levels
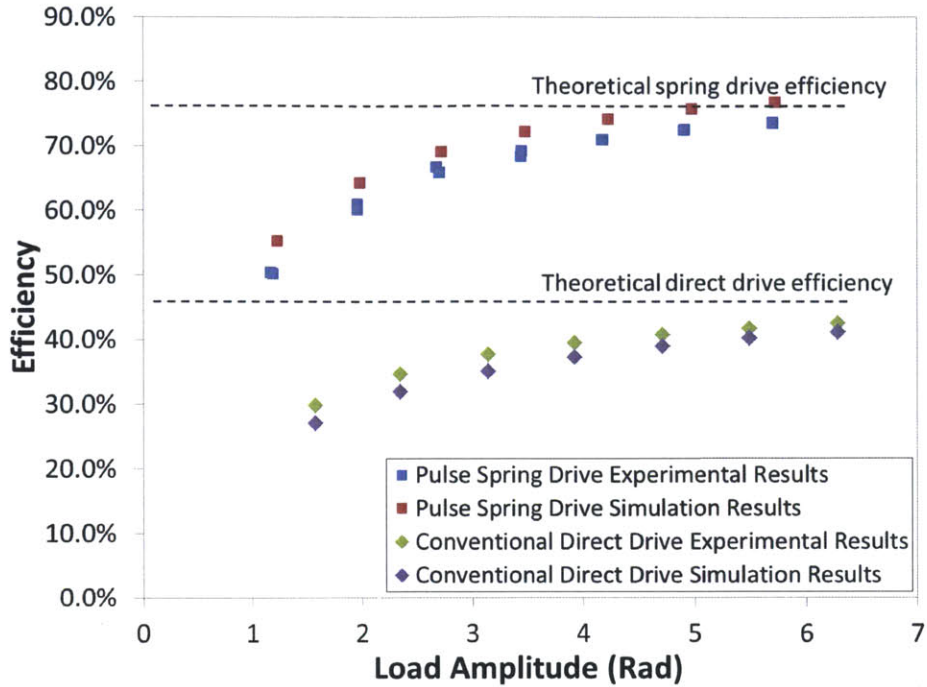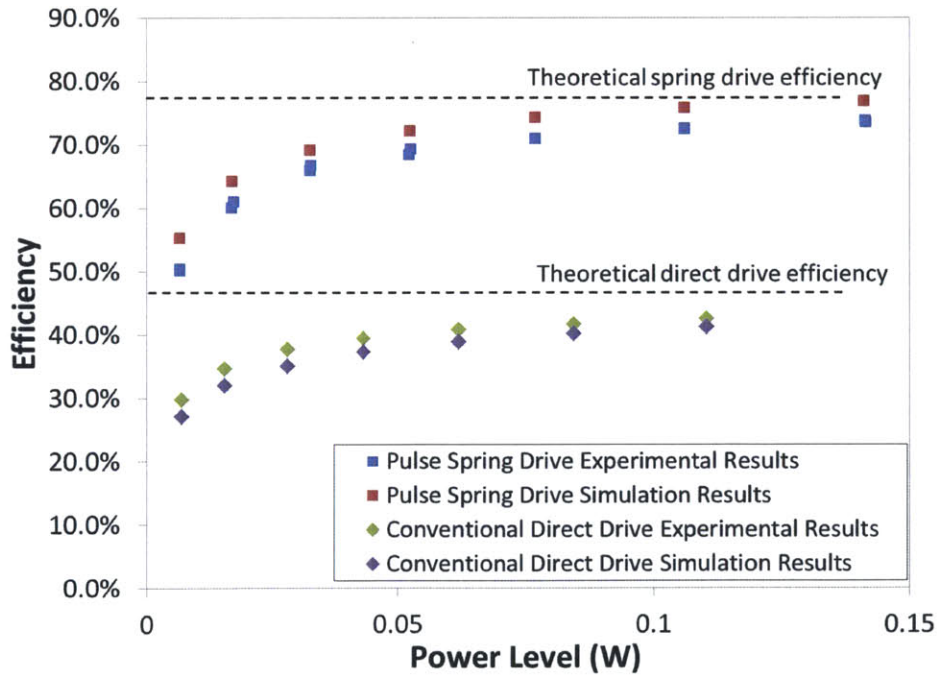
Figure 4-8: Plots of experimental energy efficiencies for the pulse direct drive and the conventional direct drive: (a) plotted versus load amplitude, (b) plotted versus load power level. The efficiency increases with amplitude for both drives, due to the less effect of motor brush friction at higher amplitude. For all scenarios, the efficiencies of the pulse direct drive are from 25% to 30% higher than the efficiencies of the conventional direct drive.

of the two driving methods using data from experiment set 3 where the load power levels are similar. The corresponding plots are shown in Figure 4-9. The maximum instantaneous power levels for both cases are similar, approximately at 1 W. The maximum current level of the pulse drive, which indicates the torque level, is about ten times lower than that of the conventional direct drive while the maximum voltage level, which is dominated by the speed level, is four times higher. Thus the pulse drive is transferring power at a much lower torque level at the expense of higher speed, which is analogous to the functionality of a speed reduction gearbox. Such an operation mode explains the efficiency gain obtained from the pulse drive because the electrical power dissipation in the motor coil resistance is proportional to the square of the current while the mechanical power output is proportional to the product of torque and speed. The ratio between mechanical power output to electrical power dissipation is much higher with high speed and low torque.

4.3.3   Comments on Friction and Other Loss

The major non-ideality in our experiment is the presence of friction which causes additional power loss. The friction comes from two sources, the dry friction of the motor brushes and the rolling element friction of the motor bearings. We model these as Coulomb plus viscous friction. A quick experiment is carried out to estimate the friction level by giving the motor shaft an initial speed and measuring its open circuit velocity decay rate in which the friction is the only opposing force. The open circuit displacement profile is shown in Figure 4-10. Since the motor brush friction is more significant, we assumed a constant dry friction torque $T_{friction}$ as the only reaction torque in the analysis and fit the curve with a second order polynomial so that the coefficient of t^2 term is numerically equal to the value of $\frac{T_{friction}}{2J}$. The resulting polynomial is $\theta = 82.94t^2 - 87.86t - 35.93$ and the calculated friction torque is $T = 1.7 \times 10^{-4}$ Nm. We then incorporate a simple friction model with the calculated dry friction torque in the Simulink simulation and the results are shown in Figure 4-8. The simulation exhibits a similar trend with the measurements that the friction has less effect on the efficiency as the driving torque becomes higher at larger amplitudes.
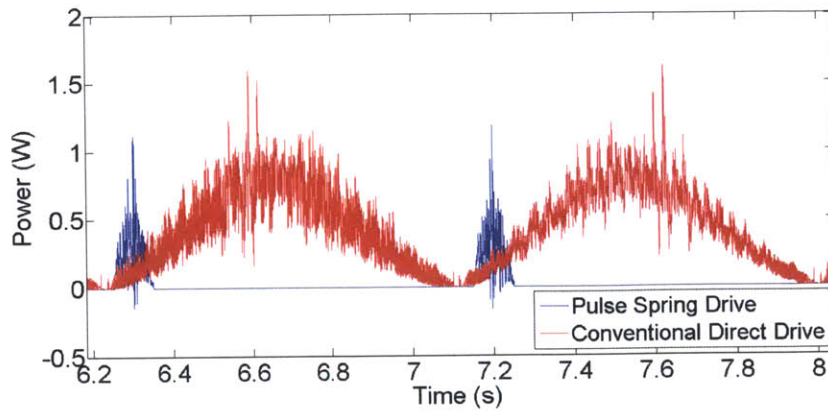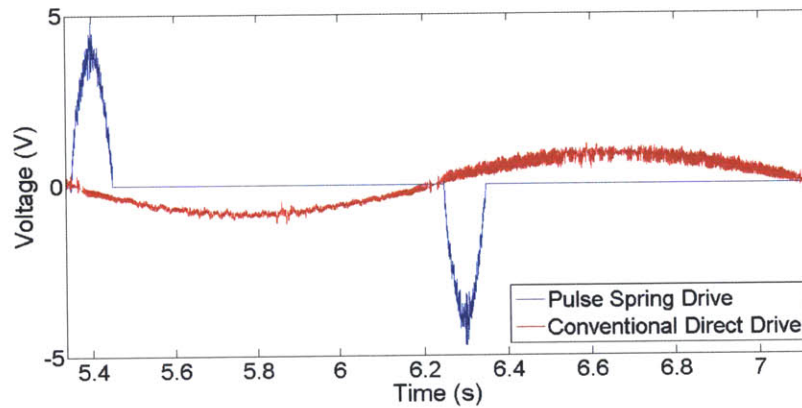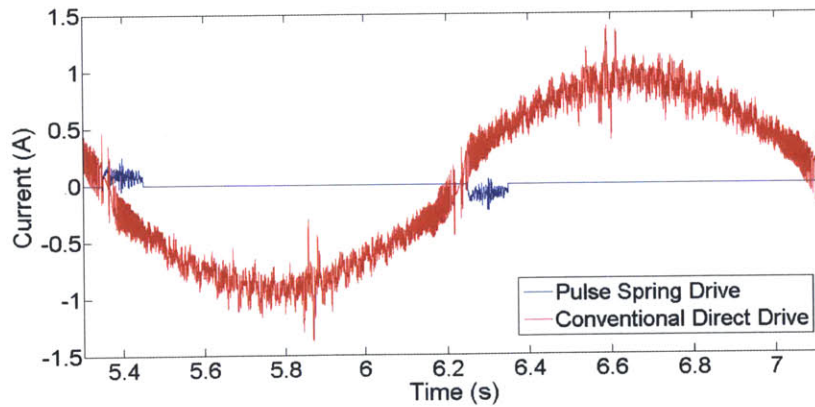
Figure 4-9: Plots of (a) instantaneous power, (b) instantaneous voltage and (c) instantaneous current from experiment set 3 in both drives. The maximum power levels in both drives are similar, approximately at 1 W. The maximum current of the pulse direct drive is 0.1 A, about ten times lower than that of the conventional direct drive while the maximum voltage is 4 V, about four times higher, due to the higher motor velocity.
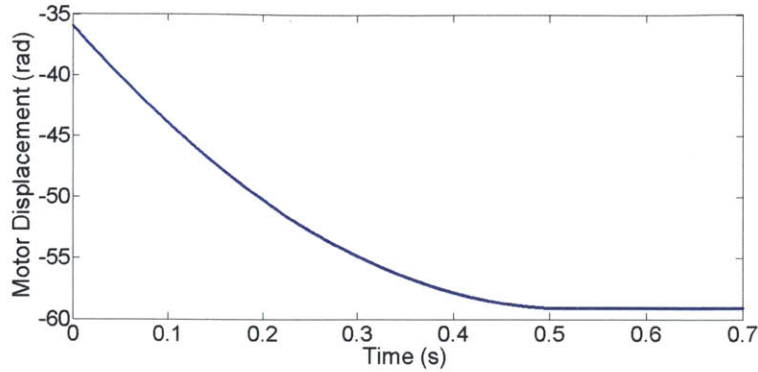
Figure 4-10: Plot of open circuit motor shaft displacement profile with an initial velocity.

However the simulated efficiencies are consistently 2% to 3% higher than the measured ones. We postulate that such discrepancy may result from the following sources: 1) a higher viscous frictional torque at higher speed, 2) other unmodeled loss in the system such as the inductive loss in the motor coil, 3) differences between the modeled parameters and actual parameters and etc.

4.4   Summary of the Chapter

- A two-motor test-stand was constructed to demonstrate the idea of the pulse drive with direct connection and compare its efficiency to the conventional direct drive.

- The measured efficiencies of the pulse drive are demonstrated to be significantly higher than the conventional drive at different power levels in this particular design.

- Through the comparisons of power, current and voltage, we find that the pulse drive is operating at lower torque but higher speed mode, leading to better motor efficiency.

- The motor friction is found to be a major non-ideality. The measured efficiency values agree well with the simulated values after including

a simple friction torque model in the simulation.

Chapter 5

Hardware Demonstration of the Pulse Drive with Gearbox Transmission

5.1   Design Overview

In Section 3.3, we model and simulate the pulse gear drive process and compare its efficiency to a conventional gear drive. Since a lot of assumptions are made to model the gearbox efficiency, it is of interest to experimentally explore the gearbox efficiency and evaluate the potential of the pulse gear drive. Due to its simplicity in design and effectiveness in measurement, we construct another two-motor test-stand with a DC brushed motor with a planetary gearhead as the driver motor and a DC brushed motor as the rotary viscous load to compare the efficiency of the pulse gear drive and the conventional gear drive.

5.2   Instrumentation and Measurements

We construct the two-motor test-stand in the same approach shown in Figure 4-1. Two DC gearmotors manufactured by Faulhaber are implemented as the driver motor. Both of the gearmotors have the same DC brushed motor but one has a one-stage

Model	P_r (W)	K_t (Nm/A)	R (Ω)	J (kgm^3)	Γ (Nms/rad)	N
FB 1724	2.5	0.0143	16.2	1×10^{-7}	1.26×10^{-5}	3.7
FB 1724	2.5	0.0143	16.2	1×10^{-7}	1.26×10^{-5}	14
MX 118745	10	0.0357	5	1×10^{-6}	2.55×10^{-4}	N/A

Table 5.1: Motor specifications for the hardware demonstration with gearbox transmission. P_r stands for the rated output power of the motor. FB is abbreviated for Faulhaber and MX is abbreviated for Maxon. The two Faulhaber brushed motors are the driver motors and the Maxon motor is the load motor.

planetary gearbox and the other one has a two-stage planetary gearbox. The driver motor is driven by the same linear power amplifier used in previous demonstration. The same Maxon 118745 brushed motor is used as the load damper. The damper value is varied electrically by connecting an additional power resistor R_l in series with the current sensing resistor so that the new damping value becomes $B_{eq} = \frac{K_t^2}{R_{motor}+R_l}$ (neglecting the small resistance of the sensing resistor). The specifications of the three motors are summarized in Table 5.1. Both the driver motor and the load motor are integrated with quadrature encoders of 1024 counts for position measurements and series current sensing resistors of 0.1Ω for current measurements. The electrical connection diagram for power and position measurements are identical in Figure 4-7. Coil springs are used in the pulse drive configuration and a rigid bar is in place for the conventional drive configuration. In this demonstration, the latch mechanism is not designed but instead simulated by applying a position holding current. On the driving electronics side, we implement the same position control loop as in Figure 4-4 with different loop tuning parameters for trajectory tracking. The same current control circuit shown in Figure 4-6 is used for current tracking. The measured position control loop return ratio has a crossover frequency of 80 Hz and a phase margin of 60 degrees, as shown in Figure 5-1. We take the same approach described in Section 4.2 to monitor the energy efficiency by measuring the driver motor voltage V_d, the driver current sensing resistor voltage V_{ds} and the load current sensing resistor voltage V_{ls}.

Two sets of experiments are carried out. The first experiment focuses on studying the gearbox loss. However in this case we are unable to separate the gearbox friction
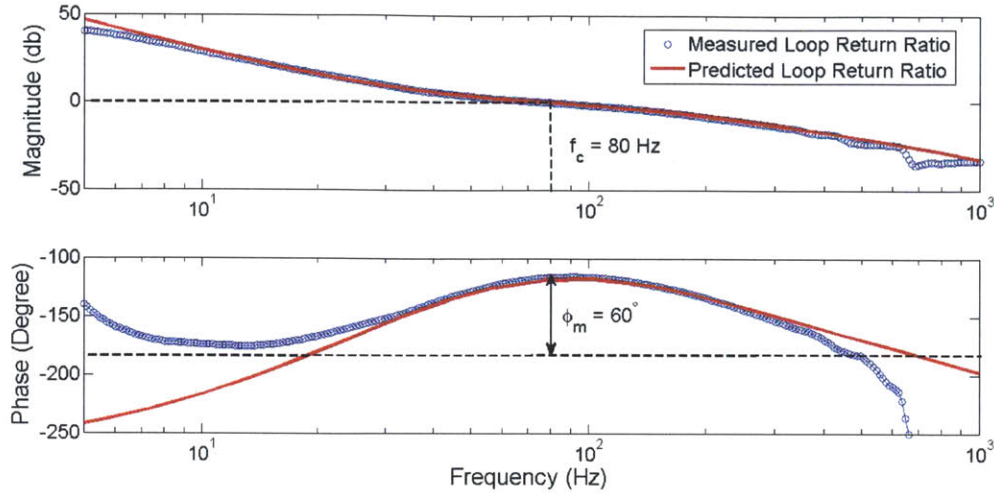
Figure 5-1: Measured and predicted loop return ratio of the position control loop of the driving gearmotor. The crossover frequency f_c is 80 Hz and the phase margin ϕ_m is 60 degrees.

from the DC motor friction so that the measured frictional torque is actually the total gearmotor friction. The frictional torques are measured at different speeds and load levels so that we can gain a better understanding of the frictional loss of the gearbox/gearmotor under different scenarios and incorporate the results into future designs. In each test, the test-stand is configured in a conventional drive mode and the rotational speed of the driver motor w is set to a constant value. The instantaneous total input power P_{total}, load motor power P_{load} and the electrical heat dissipation power $P_{electrical}$ are measured. As a result, the gearmotor frictional torque $T_{gearloss}$ is calculated as

$$T_{gearloss} = \frac{P_{total} - P_{load} - P_{electrical}}{w} \qquad (5.1)$$

The speed is varied from 200 RPM to 5000 RPM at the input end of the gearbox end and four load levels are chosen: no load, load motor open circuited, 0.5 $\Gamma_{load\ motor}$ and 1 $\Gamma_{load\ motor}$. With the obtained frictional torque data, we fit a simple gearmotor frictional torque model $T_{gearlossmodel}$ to the data by assuming that the frictional torque varies linearly with the speed $\dot{\theta}$, and with the load T_{load}, and with an offset Coulomb friction c, as

$$T_{gearlossmodel} = aT_{load} + b\dot{\theta} + c. \qquad (5.2)$$

91

Here the constants a, b and c are denoted as torque coefficient, speed coefficient and Coulomb friction coefficient, respectively. Then we simulate the efficiency of the two drives by incorporating the new frictional torque model in both the existing pulse gear drive Simulink models and in a new conventional gear drive Simulink model as shown in Figure 5-2.

The second set of experiments measures and compares the efficiency of a pulse gear drive with a one-stage gearbox to the conventional gear drive with both one and two-stage gearboxes at two different load damping levels and various amplitudes. The load damping B_{load} is chosen to be $1\Gamma_{load\ motor}$ and $0.5\Gamma_{load\ motor}$. In order to relate the load characteristics to the driver motor, we define Υ as the ratio between load damping and driver motor quality ratio,

$$\Upsilon = \frac{B_{load}}{\Gamma_{driver}} \tag{5.3}$$

In our experiments, with the two load damping values being 2.55×10^{-4} Nms/rad and 1.28×10^{-4} Nms/rad, and the driver motor quality factor being 1.26×10^{-5} Nms/rad, the two resulting Υ are 20 and 10, respectively. The trajectory profiles described in (2.16) and (3.6) are implemented for the pulse gear drive and the conventional gear drive, respectively. The pulse speed is kept at $w_p = 0.95\ w_{eq}$, the optimal pulse speed obtained from simulation, and the overall cycle frequency is chosen to be 1 Hz. In each scenario, the experiment is repeated to get an averaged efficiency result. The details of the experiment are summarized in Table 5.2.

5.3   Results

5.3.1   Results of Gearmotor Frictional Torque Study

Figure 5-3 shows the gearmotor frictional torque at different speed and load levels. In order to directly compare the frictional torque for the two gearmotors, we map the frictional torque to the output end of the gearbox and plot it versus the gearbox output speed. We also perform linear regression for each set of data at different

92

Cases	Method	B (Nms/rad)	A (Degrees)	w_p (rad/s)	w_c (rad/s)	Gearbox
1	P	2.55×10^{-4}	180	31	2π	one
2	P	2.55×10^{-4}	160	31	2π	one
3	P	2.55×10^{-4}	135	31	2π	one
4	P	2.55×10^{-4}	115	31	2π	one
5	P	2.55×10^{-4}	95	31	2π	one
6	C	2.55×10^{-4}	270	N/A	2π	one
7	C	2.55×10^{-4}	225	N/A	2π	one
8	C	2.55×10^{-4}	180	N/A	2π	one
9	C	2.55×10^{-4}	135	N/A	2π	one
10	C	2.55×10^{-4}	90	N/A	2π	two
11	C	2.55×10^{-4}	270	N/A	2π	two
12	C	2.55×10^{-4}	225	N/A	2π	two
13	C	2.55×10^{-4}	180	N/A	2π	two
14	C	2.55×10^{-4}	135	N/A	2π	two
15	C	2.55×10^{-4}	90	N/A	2π	two
16	P	1.28×10^{-4}	195	22	2π	one
17	P	1.28×10^{-4}	175	22	2π	one
18	P	1.28×10^{-4}	155	22	2π	one
19	P	1.28×10^{-4}	130	22	2π	one
20	P	1.28×10^{-4}	110	22	2π	one
21	P	1.28×10^{-4}	90	22	2π	one
22	C	1.28×10^{-4}	270	N/A	2π	one
23	C	1.28×10^{-4}	225	N/A	2π	one
24	C	1.28×10^{-4}	180	N/A	2π	one
25	C	1.28×10^{-4}	135	N/A	2π	one
26	C	1.28×10^{-4}	90	N/A	2π	two
27	C	1.28×10^{-4}	270	N/A	2π	two
28	C	1.28×10^{-4}	225	N/A	2π	two
29	C	1.28×10^{-4}	180	N/A	2π	two
30	C	1.28×10^{-4}	135	N/A	2π	two
31	C	1.28×10^{-4}	90	N/A	2π	two

Table 5.2: Parameters of the pulse gear drive and the conventional gear drive experiments which includes two load levels and several amplitude levels. In the "Method" column, "P" stands for the pulse drive and "C" stands for the conventional drive. In the "Gearbox" column, "one" stands for one-stage gearbox and "two" stands for two-stage gearbox. w_p stands for the pulse frequency and w_c stands for the cycling frequency. The pulse drive experiments are conducted with a one-stage gearbox. The conventional drive experiments are conducted with both the one-stage and two-stage gearboxes.

Figure 5-2: Modified conventional gear drive Simulink model with gearmotor frictional torque model added.

load levels and then fit the model described in (5.1) to the entire sets of data of one gearmotor. The fitted model for the gearmotor with a one-stage gearbox is

$$T_{one\ stage} = 0.17 T_{load} + 3 \times 10^{-6} \dot{\theta}_{output} + 3 \times 10^{-4}, \tag{5.4}$$

and the fitted model for the gearmotor with a two-stage gearbox is

$$T_{two\ stage} = 0.09 T_{load} + 1 \times 10^{-4} \dot{\theta}_{output} + 1.6 \times 10^{-3}. \tag{5.5}$$

Here all torques are in units of Nm. The frictional torques for the two gearmotors are both increasing proportionally to the speed and load levels. However, compared to a one-stage gearbox, the friction torque for a two-stage gearbox is much more dependent on speed than load, as can be observed from the coefficient of the model and the figures. The torque coefficient decreases by a factor of 2 while the speed coefficient increases by a factor of 30 as compared with a one-stage gearbox. Additionally the offset Coulomb friction mapped to the gearbox output end is approximately 5 times as large.

5.3.2 Energy Efficiency Results

The simulated and experimental energy efficiency results for the two driving conditions are summarized in Figure 5-4 in which the simulated efficiency results are

(a)

(b)

Figure 5-3: Plots of measured gearmotor frictional torque versus speed at the output shaft: (a) one-stage Gearbox N = 3.7 and (b) two-stage Gearbox N = 14. The frictional torque for both gearmotors increases with the output speed. For the motor with one-stage gearbox, the frictional torque is also strongly dependent on the load.

obtained with the gearmotor frictional torque model described in Section 5.2. Overall, the experimental results agree well with the simulation results with a maximum of about 3% in difference, indicating the usefulness of the gearmotor model. Even though (3.26) predicts that the efficiency should be independent of the drive amplitude, the measured efficiency rises with the load amplitude due to the relatively smaller effect of dry friction at larger displacements.

The experimental efficiency results demonstrate that with Υ as large as 10 and 20, the pulse gear drive are more efficient than the conventional gear drive at the same load amplitude. Recall that Υ is defined as the ratio between the load impedance to the driver motor quality factor (5.3). At $\Upsilon = 10$, the efficiency of the pulse gear drive is approximately 25% higher than the conventional drive with a one-stage gearbox, and 15% higher than the conventional gear drive with a two-stage gearbox. At $\Upsilon = 20$, the efficiency of the pulse gear drive is approximately 15% higher than the conventional drive with a one-stage gearbox, and 20% higher than the conventional gear drive with a two-stage gearbox. Note that the efficiency results in these experiments are much lower than the efficiency results obtained from the pulse direct drive experiment. Such low efficiency is due to the fact that the load damping is much greater than the driver motor quality factor where in the previous experiment the two values are equal. In addition, the selected driver motor is not the optimal choice because the main purpose of this experiment is to study the effect of adding a gearbox transmission to the pulse drive system and to validate the simulation results, instead of maximizing efficiency.

5.3.3   Driver Power, Voltage and Current Comparison

In addition to the energy efficiency, we also compare the instantaneous power, voltage and current levels of the three different drives at the load amplitude of π for both Υ levels (Figure 5-5 and Figure 5-6). As opposed to the direct drive scenarios in which the power levels are comparable for the two driving modes, at both Υ levels, the maximum power and voltage levels of the pulse gear drive are almost twice as high as both of the conventional gear drive methods, while the current level of the
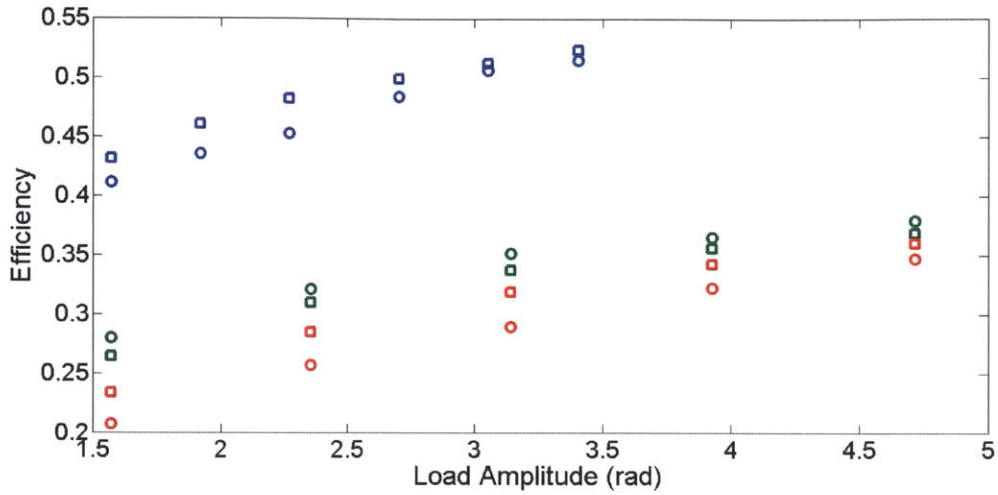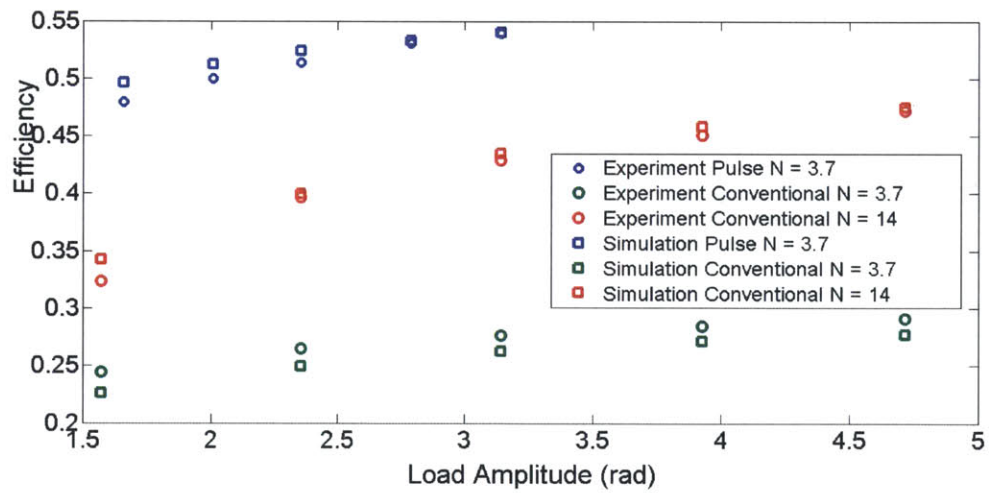
Figure 5-4: Plots of the gear drive energy efficiency at two loads: (a) $\Upsilon = 10$; (b) $\Upsilon = 20$. At $\Upsilon = 10$, the efficiency of the pulse gear drive is approximately 25% higher than the conventional drive with a one-stage gearbox, and 15% higher than the conventional gear drive with a two-stage gearbox. At $\Upsilon = 20$, the efficiency of the pulse gear drive is approximately 15% higher than the conventional drive with a one-stage gearbox, and 20% higher than the conventional gear drive with a two-stage gearbox.

pulse gear drive is comparable to a one-stage gearbox conventional drive but higher than a two-stage gearbox conventional drive. Therefore, the pulse gear drive at large Υ levels places a higher requirements for the actuator, which becomes a tradeoff for their higher energy efficiency.

5.3.4 Comments on Gearmotor Efficiency and Gearbox Efficiency

Even though our analytical derivation predicts that the overall efficiency will decrease at higher load levels for both drive process, we observe in Figure 5-4 that the efficiency results of both the pulse gear drive and the conventional gear drive with two-stage gearbox are actually higher at $\Upsilon = 20$, which we postulate to result from a higher gearmotor efficiency at larger load damping level. The experimental gearmotor efficiency results are summarized in Figure 5-7. In all three driving scenarios, the gearmotor efficiency is higher at larger load levels $\Upsilon = 20$ and it increases slightly with the load amplitude. With the same one-stage gearbox, the conventional drive has higher gearmotor efficiencies than the pulse drive. The conventional drive with a two-stage gearbox has lower gearmotor efficiencies than the two drives with a one-stage gearbox. To calculate the gearmotor efficiency from our simple gearmotor frictional loss model, (5.6) is used

$$
\eta_{gearmotor} = \frac{P_{load}}{P_{load} + P_{gear\ loss}} = \frac{T_{load}\dot{\theta}}{T_{load}\dot{\theta} + aT_{load} + b\dot{\theta} + c}
$$
$$
= \frac{1}{(a+1) + \frac{b\dot{\theta}}{T_{load}} + \frac{c}{T_{load}\dot{\theta}}}.
$$
(5.6)

In the conventional drive, the average load torque is proportional to the product of the damping value and the speed level. The speed level is proportional to the amplitude and the operating frequency. Thus we replace T_{load} with $\alpha B_{load}w_{cycle}A_{load}$ where α is a generic coefficient. The gearmotor efficiency expression for the conventional gear
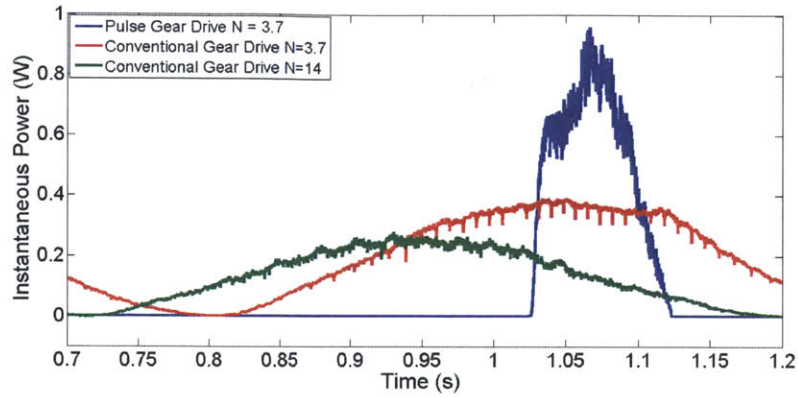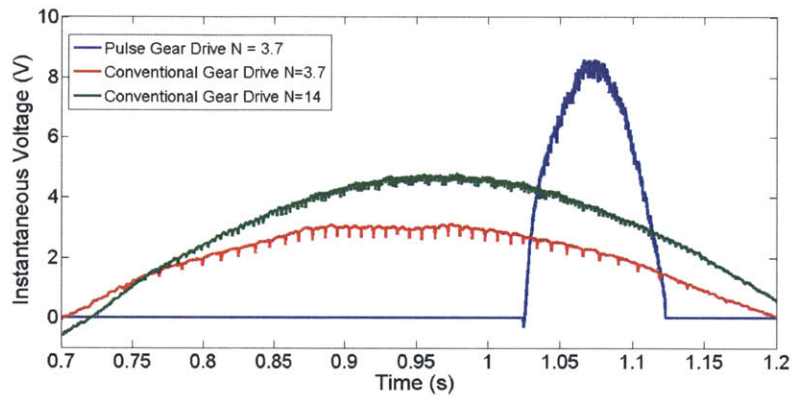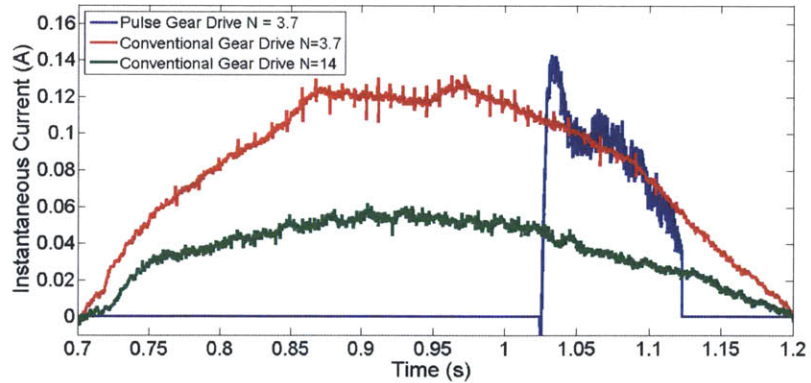
Figure 5-5: Plots of (a) instantaneous power, (b) instantaneous voltage and (c) instantaneous current at load $\Upsilon = 20$. Note that the three plots are not in phase due to the difference in the starting time of data logging. The maximum power and voltage of the pulse gear drive are almost twice as those of the two conventional drives. The maximum current of the pulse gear drive is similar to the conventional drive with one-stage gearbox, and about twice that of the conventional drive with two-stage gearbox.
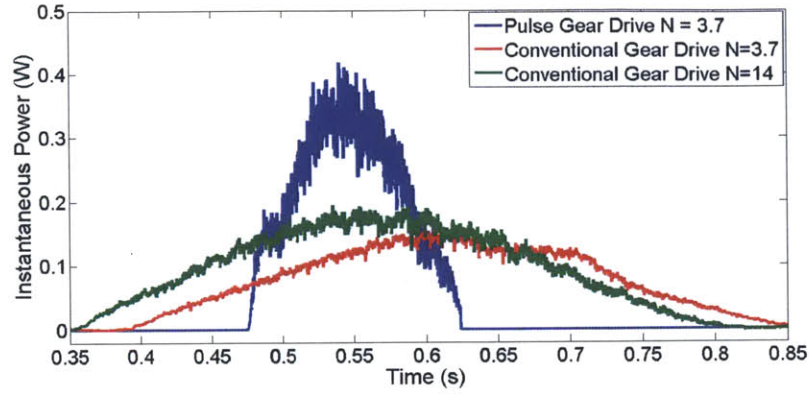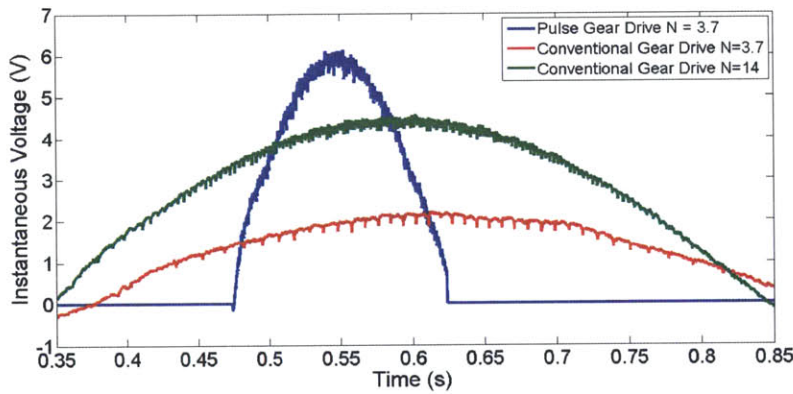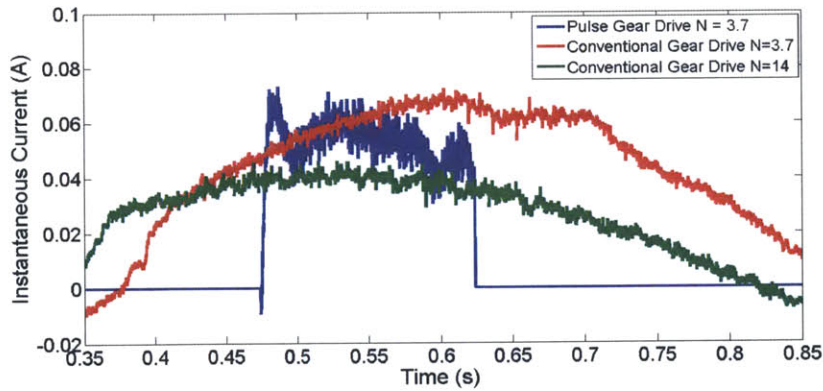
Figure 5-6: Plots of (a) instantaneous power, (b) instantaneous voltage and (c) instantaneous current at load $\Upsilon = 10$. Note that the three plots are not in phase due to the difference in the starting time of data logging. The maximum power of the pulse gear drive is almost twice as that of the two conventional drives. The maximum voltage of the pulse gear drive is 50% higher than that of the conventional drive with two-stage gearbox, and about three times that of the conventional drive with one-stage gearbox. The maximum current of the pulse gear drive is similar to that of the conventional drive with one-stage gearbox, and about 50% higher than of the conventional drive with two-stage gearbox.
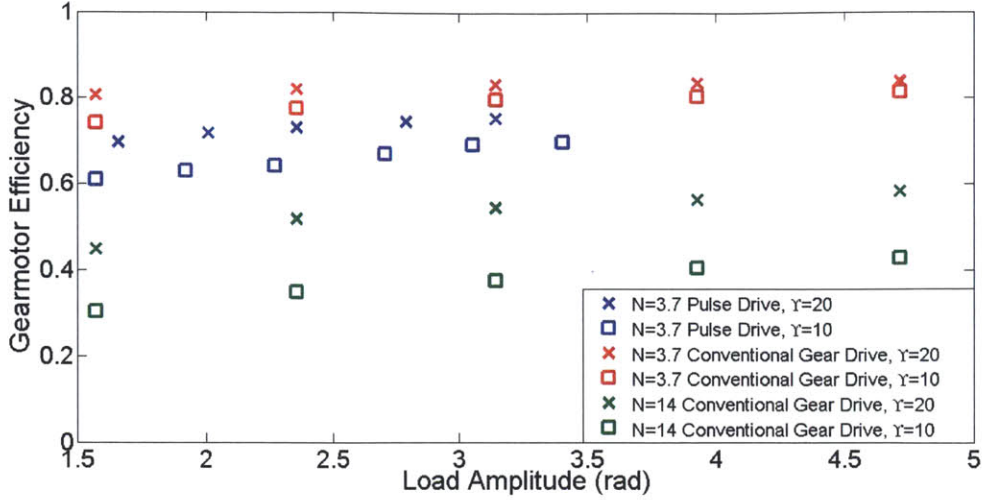
Figure 5-7: Plot of calculated gearmotor efficiency. In all three driving scenarios, the gearmotor efficiency is higher at larger load levels $\Upsilon = 20$ and it increases slightly with the load amplitude. With the same one-stage gearbox, the conventional drive has higher gearmotor efficiency than the pulse drive. The conventional drive with two-stage gearbox has lower gearmotor efficiency than the two drives with one-stage gearbox.

drive then becomes

$$\eta_{gearmotor\ conventional\ drive} = \cfrac{1}{(a+1) + \cfrac{b}{\alpha B_{load}} + \cfrac{c}{\alpha^2 B_{load} w_{cycle}^2 A_{load}^2}}. \tag{5.7}$$

In the pulse drive, the average load torque is proportional to the spring constant and the amplitude. The spring constant is adjusted to be proportional to the load damping value. The average speed level is proportional to the amplitude and the pulse frequency. Thus we replace T_{load} with $\beta B_{load} A_{load}$ and replace $\dot{\theta}$ with $\gamma A_{load}\sqrt{\frac{B_{load}}{J}}$ where β and γ are generic coefficient. The gearmotor efficiency expression for pulse gear drive becomes

$$\eta_{gearmotor\ pulse\ drive} = \cfrac{1}{(a+1) + \cfrac{\gamma b}{\beta\sqrt{B_{load}J}} + \cfrac{c}{\beta\gamma\sqrt{B_{load}^3 J}A_{load}^2}} \tag{5.8}$$

As a result, both efficiency expressions indicate that the gearmotor efficiency will rise with respect to increasing load damping and amplitude levels. A larger damping value will minimize the gearbox loss due to the speed effect introduced by the speed
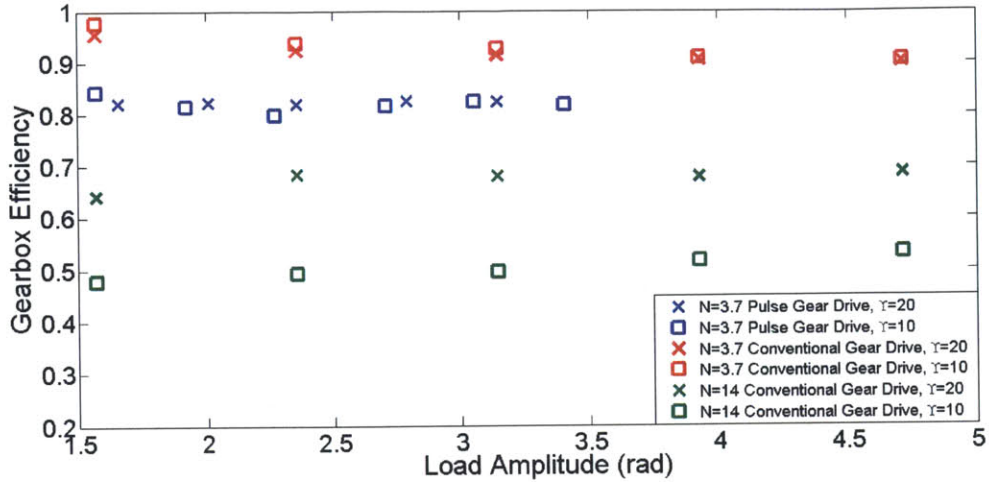
Figure 5-8: Plot of estimated gearbox efficiency. The one-stage gearbox efficiency appears to be independent of load amplitude. It is approximately 90% for the conventional drive and 80% for the pulse drive. The two-stage gearbox efficiency is load dependent, with approximately 70% at $\Upsilon = 20$ and 50% at $\Upsilon = 10$.

coefficient and the Coulomb friction effect while a larger amplitude will minimize the gearbox loss due to the Coulomb friction effect only. It is worth pointing out that if the speed coefficient b and the Coulomb friction c are negligible compared to a, then at a reasonable speed and load, the efficiency of the gearmotor will be approximated by a constant of $\frac{1}{1+a}$. As b and c become larger, the load damping and amplitude levels will affect the gearmotor efficiency more. As observed from the two gearmotor models, the gearmotor with a one-stage gearbox has a much smaller speed coefficient b and Coulomb friction c, resulting in much smaller differences in gearmotor efficiency as shown in Figure 5-7, than the gearmotor with two-stage gearbox.

The gearmotor efficiency analysis above includes the frictional loss of the brushed DC motor itself. However, we can minimize such loss by using a brushless motor. Thus we are further interested to learn the loss introduced by the gearbox only as a reference for future analysis and simulation. As presented in Section 4.3.3, the motor brush friction torque can be approximated by a constant Coulomb friction term. We estimate the motor brush friction torque by assuming that it is equal to the value of the measured Coulomb frictional torque with one-stage gearbox mapped to the gearbox input end, which is 7.5×10^{-5} Nm. We make such assumption because the measured

Coulomb frictional torque is lower than the frictional torque 1.3×10^{-4} Nm stated on the specification sheet so that the motor brush friction is the sole contributor. By separating the motor friction loss, the estimated gearbox efficiency results are shown in Figure 5-8. The one-stage gearbox efficiency stays almost constant for all pulse drive scenarios, approximately 80%, so does in conventional drive with one-stage gearbox, approximately 90%. However, the two-stage gearbox efficiency still exhibits a strong dependency on the load damping levels, with 70% at $\Upsilon = 20$ and 50% at $\Upsilon = 10$. Therefore, we propose that we might use one single efficiency value for the pulse gear drive with a one-stage gearbox, a different single efficiency value for the conventional gear drive with a one-stage gearbox, but use load dependent efficiency values for the conventional gear drive with a two-stage gearbox in future analysis and simulation.

5.4 Summary of the Chapter

- **A second two-motor test-bed using gearmotors as the driver motor shows that the pulse gear drive is more efficient than the conventional drive at all load amplitude levels for two load damping levels $\Upsilon = 10$ and 20, where Υ is ratio between the load damping and the driver motor quality factor.**

- **Study on instantaneous power, current and voltage shows that the power and voltage requirements are higher for pulse gear drive in this experiment which becomes a tradeoff for using the pulse drive.**

- **Experimental data shows that the gearmotor frictional torque is load and speed dependent. We estimate the gearbox efficiency and find that we may use single efficiency values to simulate the pulse gear drive with a one-stage gearbox.**

Chapter 6

Influence of Motor Size

6.1 Motivations of Study

In previous chapters, we presented the tradeoffs of the pulse drive. We demonstrated both in simulation and hardware that the pulse drive can be more energy efficient than the conventional drive. To converge to the goal of this project, we are interested in exploring whether the pulse drive is a good candidate for the robotic fish tail pro-plusion. More specifically, given the fish tail operating load and power requirements, how should we select the right actuator for the pulse drive and whether it is advantageous to implement such drive, with or without any form of transmission?

We have also concluded that for given operating conditions specified by the displacement amplitude A and load damping value B, the efficiency of the pulse gear drive is a function of the chosen spring constant k, actuator quality factor Γ, motor inertia J and the gear ratio N (3.22). If a spring constant k has been chosen for the particular load level, then the efficiency is proportional to Γ and to the inverse square root of J. For similar operating conditions, the efficiency of the conventional drive is proportional to Γ but less dependent on J (3.26). For typical electromechanical actuator designs, both Γ and J increase with motor size. It seems that a larger motor size will always yield higher efficiency for the conventional drive and possibly for the pulse drive. However, on the other hand, using a large motor will bring undesirable consequences, such as adding weight, volume and cost to the robot design.

Therefore, with the foreseen questions and tradeoffs, we focus on studying the effects of motor size on the pulse drive operation and briefly introduce guidelines for selecting the right motor for a given operation.

6.2 Study Methodology

In this study, we use the same simple spring drive electromechanical model described in previous chapters (Figure 3-1). The load conditions, motor specifications and calculated parameters are listed below.

Operating requirements

> According to Professor Barrett, the power level for the robotic tuna fish tail propulsion varies from a fraction of a Watt to several Watts. Thus we set the load damping value B approximately at 0.0125 Nms/rad so that the same power levels is achievable by varying the load amplitudes. The target load maneuver frequency is set as 1 Hz to mimic the expected fish flipping frequency.

Studied motors

> In the two hardware demonstrations, we have observed that the motor brush friction has a considerable effect on overall energy efficiency. To minimize the loss due to brush friction, brushless motors are chosen in this study. We reference the Maxon EC series brushless DC motor specifications for their variety in motor sizes and completeness in specifications. The motor specifications can be found in Table A.1 in Appendix A. A total of 18 motors are studied. To more effectively convey the information, we label the smallest motor as Motor 1 and the largest motor as Motor 18.

Calculated Parameters

> To determine whether a motor is suitable for the application, many parameters need to be taken into consideration besides the energy efficiency, such as the power level and the speed level. Thus for each of the motors studied, we calculated the following parameters using the derived analytical expressions:

- motor size $V = \pi(D_{motor}/2)^2 L_{motor}$ based on motor diameter D_{motor} and length L_{motor}. However, the gearbox volume is not included in the motor size calculation for the purpose of easy comparison. In a real design, the higher the gear ratio, the more volume it will add to the total motor size,

- motor quality factor $\Gamma = K_t^2/R$,

- motor quality factor Γ to square root of J ratio $\Gamma/\sqrt{J}$,

- pulse drive efficiency η_{pulse},

- optimal pulse radian frequency $w_{optimal}$ and corresponding pulse time $t_{pulse} = \pi/w_{optimal}$,

- maximum speed $\dot{\theta}_{max} = w_{optimal} A$ during the pulse phase,

- average pulse power $P_{pulse} \approx W_{useful}/(\eta_{pulse} t_{pulse})$,

- conventional drive efficiency $\eta_{conventional}$.

The pulse drive parameters are calculated with both a direct connection and with a one-stage gearbox transmission. The conventional drive parameters are calculated with the direct connection, a one-stage gearbox transmission and a two-stage gearbox transmissions. We assume a gear ratio of 5 for a one-stage gearbox and a gear ratio of 25 for a two-stage gearbox. We also assume constant gearbox efficiency values of 85%, 90% and 70% for the pulse drive with a one-stage gearbox, the conventional drive with a one-stage gearbox, and the conventional drive with a two-stage gearbox, respectively.

6.3 Results and Discussion

6.3.1 Tradeoff Between Efficiency and Size

As a quick study on parameters Γ and $\Gamma/\sqrt{J}$ which govern the efficiency of the two types of drives, we plot the two parameters versus the motor size on a log-log scale shown in Figure 6-1. Both parameters increase with the motor size, but the change rate of $\Gamma/\sqrt{J}$ is smaller than that of Γ. Therefore we expect the efficiency of the pulse drive to be less sensitive to motor size variations. The calculated efficiency results are

107
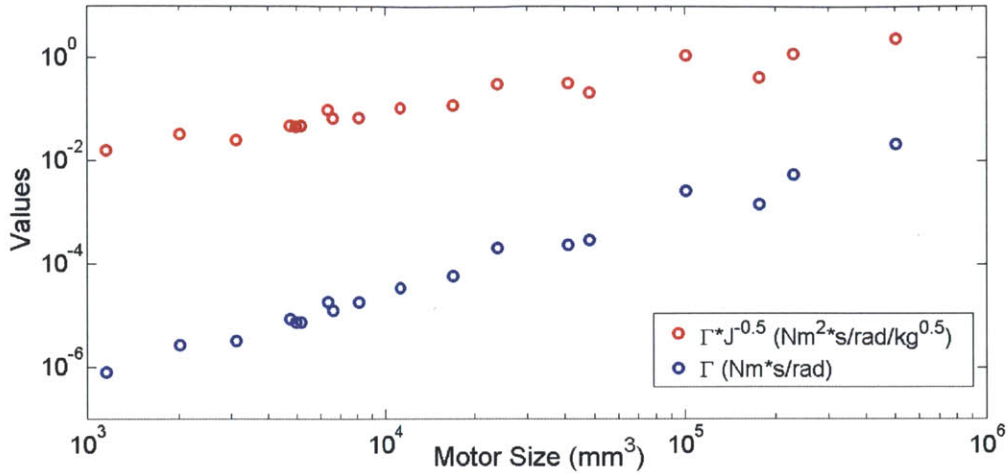
Figure 6-1: Plots of Γ and $\Gamma/\sqrt{J}$ versus motor size for Maxon motor EC series. Γ increases more rapidly with the motor size than $\Gamma/\sqrt{J}$.

shown in Figure 6-2 with the motor number labeled. Overall, the efficiency rises with motor size. Note that due to the acceleration and deceleration of the high reflected inertia at high gear reduction ratio, the efficiency of the conventional gear drive with a two-stage gearbox actually begins to drop with the three largest motors. Among the five drive scenarios, the pulse gear drive appears as the most energy efficient drive whereas the conventional direct drive is the least efficient drive, except for the case with the largest motor. we observe that with smaller motors of V up to 5×10^4 mm^3 (Motor 14), as indicated by the dot line, the pulse gear drive and the pulse direct drive have a distinct efficiency gains over the conventional direct drive and the conventional drive with a one-stage gearbox. Only the efficiency of the conventional drive with a two-stage gearbox is higher than that of the pulse direct drive but it is still lower than that of the pulse gear drive. We also notice that the efficiencies of the conventional direct drive and the conventional gear drive with a one-stage gearbox are near 0% for smaller size motors. Such low efficiency is due to the extremely high B/Γ and $B/(\Gamma N^2)$ ratios that the conventional direct drive efficiency and the conventional gear drive efficiency are respectively inversely proportional to, as indicated by (3.11) for the conventional direct drive and (3.26) for the conventional gear drive. The B/Γ and $B/(\Gamma N^2)$ ratios are plotted in Figure 6-3. The dash line represents the ratio of

108

100. The points above the ratio 100 correspond to an efficiency lower than 1%. For the conventional gear drive with a one-stage gearbox, the efficiencies of the smallest three motors are below 1%. For the conventional direct drive, the efficiencies of the smallest eleven motors are below 1%. Because the growth rate of Γ is higher than $\Gamma/\sqrt{J}$, the efficiency of the conventional gear drive eventually catches up and becomes comparable to the pulse gear drive and the pulse direct drive at the four largest motors. The highest efficiency is 85%, which is obtained from either using the pulse direct drive or the conventional gear drive of Motor 18. Thus by choosing a larger size motor, we can obtain higher efficiency.

However, there is a tradeoff between the motor size and the efficiency gain for two reasons. For an underwater vehicle like the robotic fish, volume may be critical. Adding motor volume, if it makes the fish longer, will raise the required thrust and power level for propulsion. For another reason, we observe that the marginal efficiency gain is diminishing with the increase of the size. For example, by increasing the size ten times from Motor 7 to Motor 13, the highest efficiency, which is the pulse gear efficiency, increases from 50% to 70%. By increasing the same size factor from Motor 13 to Motor 18, the highest efficiency only increases from 70% to 85%. Therefore, with such a tradeoff, the optimal choice would be the smallest motor with acceptable efficiency, depending upon the packaging tradeoffs.

6.3.2   Power and Speed Constraints

Two important criteria in motor selection are to determine if the motor's specifications can meet the required speed and power levels. Thus we calculate and compare the maximum speed level and average pulse power level to the motor rated speed and rated average output power for each pulse drive case. Note that we are conservative on the power comparison because the intermittent power a motor outputs can be higher than the motor's rated average output power. The results are summarized in Figures 6-4 and 6-5. We observe that as the motor size decreases, both the maximum speed and the average pulse power increase. The growth in maximum speed is solely due to the the higher pulse radian frequency brought by a smaller motor inertia as

109
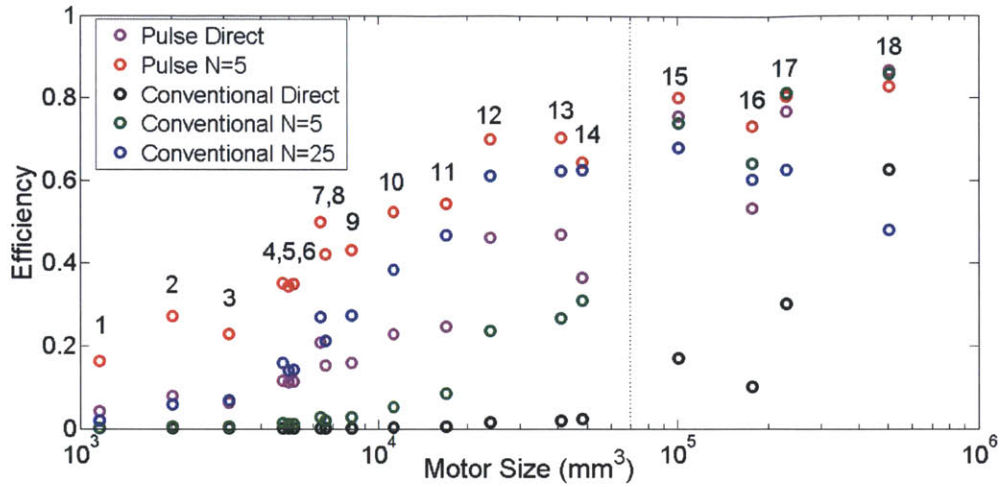
Figure 6-2: Plots of calculated efficiency versus motor sizes for the five drive scenarios. The efficiency increases with motor size. For smaller size motors up to Motor 14, as separated by the dot line, the pulse drive with one-stage gearbox and the pulse direct drive have clear efficiency gains over the conventional drive with a one-stage gearbox and the conventional direct drive. Only the conventional drive with a two-stage gearbox is more efficient than the pulse direct drive. For larger motors (Motor 15 to Motor 18), the efficiency of the two pulse drives and the two conventional gear drives are very close to each other.
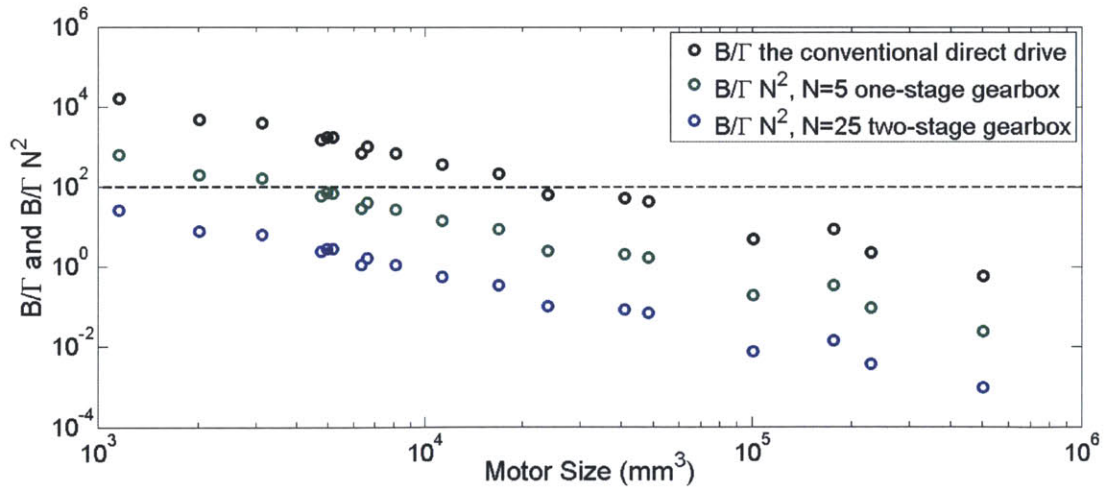
Figure 6-3: Plots of B/Γ and $B/(\Gamma N^2)$ ratios versus motor sizes. The dash line represents the ratio of 100. The points beyond the ratio 100 correspond to an efficiency lower than 1%. For the conventional gear drive with a one-stage gearbox, the efficiencies of the smallest three motors are below 1%. For the conventional direct drive, the efficiencies of the smallest eleven motors are below 1%.

110
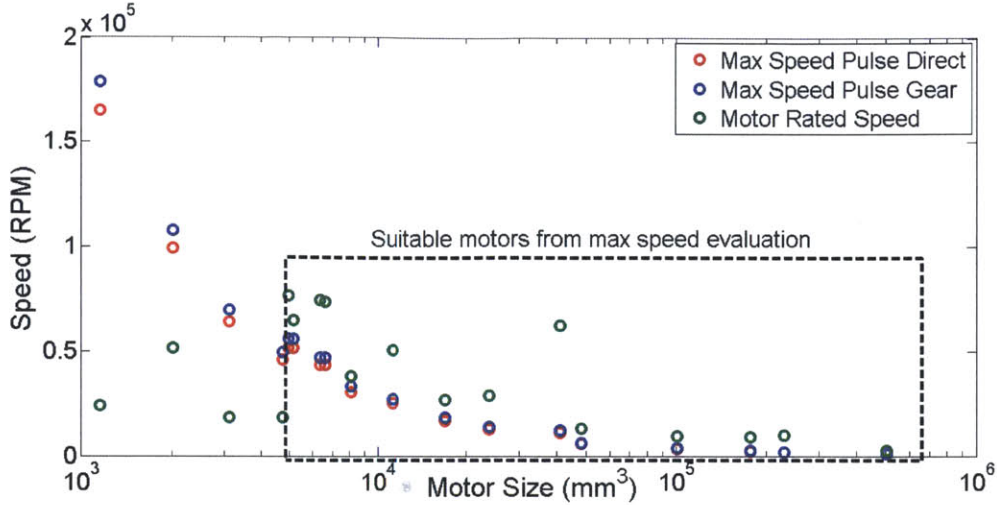
Figure 6-4: Plots of required maximum speed versus motor size for the two pulse drives. The maximum speed decreases with motor size. The smallest four motors are not suitable for the pulse drive as the maximum speed exceeds the rated motor speed.

$w_{optimal} = \sqrt{k/J}$. The rise in average pulse power is a combined effect of higher pulse radian frequency and declining energy efficiency. As a result, the two parameters exceed the motor's ratings for smaller motors. The maximum pulse speed exceeds the motor's speed rating for the smallest four motors while the average pulse power goes beyond the motor power capacity for the smallest eleven motors. Combining the two results, we conclude that the smallest eight motors don't meet the requirement and thus they are not suitable for the pulse drive operation at this load level.

6.3.3 Pulse Period Constraint

The third constraint for the pulse drive is that the pulse period needs to be smaller than the overall maneuver period. We consider 0.2 s, which is 1/5 of the overall period, as the upper time limit for each pulse. Figure 6-6 shows the calculated pulse time. Overall the pulse time increases with motor size due to the increase in motor inertia. Since the trajectory radian frequency of the pulse gear drive w_{eq} is scaled down by the gear ratio $N = 5$, $w_{eq} = 1.15 \frac{1}{N}\sqrt{k/J}$, it is expected to see that the pulse time for the pulse gear drive $t_{pulse} = \pi/w_{eq}$ is approximately five times as large as the pulse time for the pulse direct drive of the same motor. As a result of the longer

111
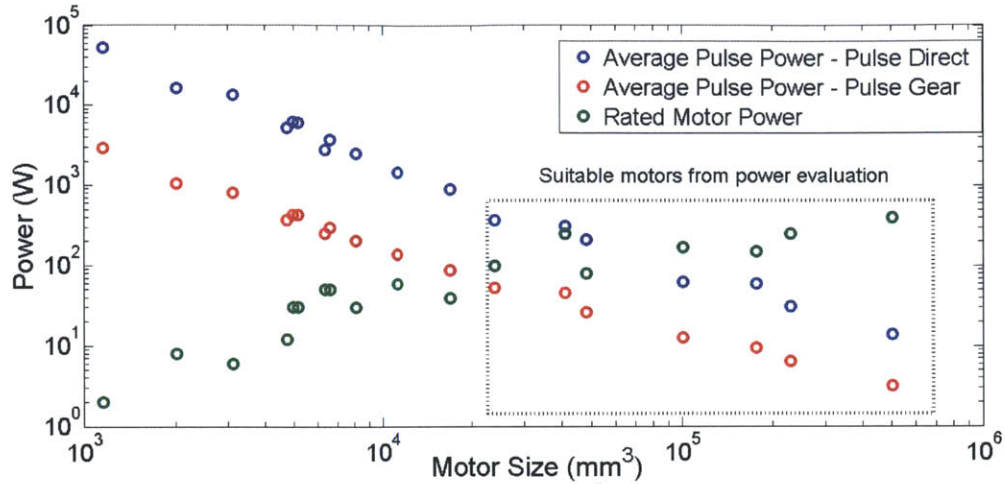
Figure 6-5: Plots of average pulse power versus motor size for the two pulse drives. The average pulse power decreases with motor size. The smallest eleven motors are not suitable for the pulse drive as the average pulse power exceeds the rated motor average output power.

pulse time, we find that the two largest motors are not suitable for pulse gear drive.

6.3.4 Selected Motor

By filtering out the motors that don't meet the constraint, we show the efficiency of suitable motors in Figure 6-7. Overall in our studied case, if the robotic design is not constrained by volume, weight and cost, the largest suitable motor (Motor 18) should be selected either in the pulse direct drive mode or in the conventional drive mode with a one-stage gearbox to achieve a highest efficiency of 85%. However, with the tradeoff of added volume in a practical design as discussed in Section 6.3.1, the optimal actuator would be the smallest suitable motor (Motor 13) in the pulse gear drive mode. Although the resulting efficiency is 70%, which is 15% lower than the highest efficiency, the corresponding volume is one tenth and the cost is one third [5]. With this motor, the efficiency of the pulse gear drive is 10% higher than the conventional gear drive with two-stage gearbox and 25% higher than the conventional gear drive with one-stage gearbox. Alternatively, if the real design imposes a constraint of no gearbox usage, Motor 15 can be selected in direct spring drive mode to achieve a comparably high efficiency of 75%. On the other hand, the optimal scenario for the

112
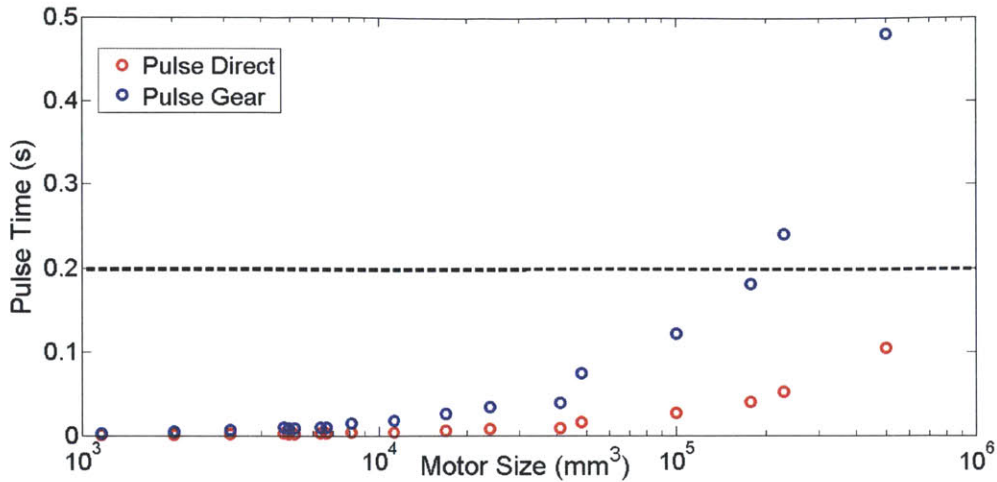
Figure 6-6: Plots of pulse time versus motor size for the two pulse drives. The pulse time increases with motor size due to the increase in motor inertia. The pulse time of the pulse gear drive for the two largest motors exceeds the time constraint of 0.2 *s*.

conventional drive is to choose Motor 15 with a one-stage gearbox to achieve an efficiency of 73%. Note that with this motor, an efficiency gain of 7% can still be achieved by using the pulse gear drive.

Moreover, as discussed in Section 3.5.3, we can achieve better efficiency with the deadzone drive. Thus we calculate the deadzone drive efficiency using Motor 12 with a one-stage gearbox. The efficiency and the corresponding pulse time is shown in Figure 6-8. The maximum efficiency as $n \to 0$ is 85% which is the estimated gearbox efficiency. In such case, the pulse time also approaches infinity. With a reasonable pulse time, such as $t_{pulse} = 0.15$ s shown on the figure, an efficiency of 82.5% can be reached. This efficiency is almost as high as the efficiency with the largest motor in our study.

6.4 Summary of Study Results and General Guidelines for the Pulse Drive Motor Selection

In this study, we set a target load and power level and calculated the motor energy efficiency of both the pulse drive and the conventional drive of the Maxon EC brushless
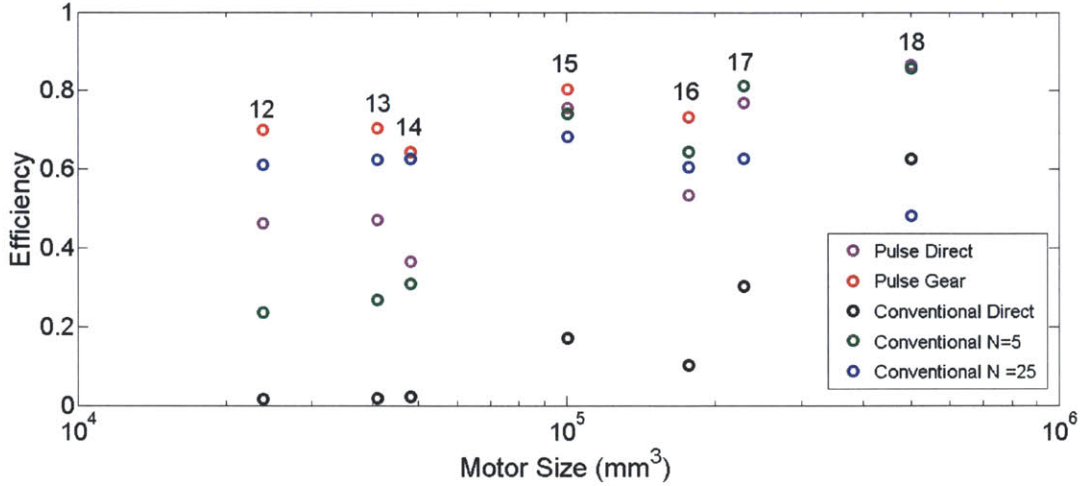
Figure 6-7: Plots of pulse drive efficiency for suitable motors. Note that the pulse gear drive is no longer applicable for Motor 17 and 18 because the pulse time exceeds the constraint.

motor series. The efficiency results show that the pulse drives are more efficient than the conventional drives for smaller motors. For larger motors, the efficiencies are comparable. Moreover, we observe that larger motors in general yield better efficiency. However, by taking into account constraints on power, speed and pulse time, and tradeoffs of volume and cost, we conclude that the optimal drive mode for this particular operation may be the pulse drive with the smallest motor that meets the power and speed requirements. As the motor becomes larger, the volume and cost may outweigh the efficiency gain. In addition, if a gearbox is not available, a slightly larger motor can be used to provide comparable efficiency in the pulse direct drive mode. Moreover, we find that the deadzone drive can achieve even better efficiency if it can be implemented.

Therefore, we summarize the general guidelines for pulse drive motor selection in the following steps.

1. Determine target operating requirements, such as load value, power level and cycle period, and estimate the corresponding spring constant by matching the spring-damper time constant.

2. Screen motors by calculating the pulse gear drive efficiency with (3.26) and the

114
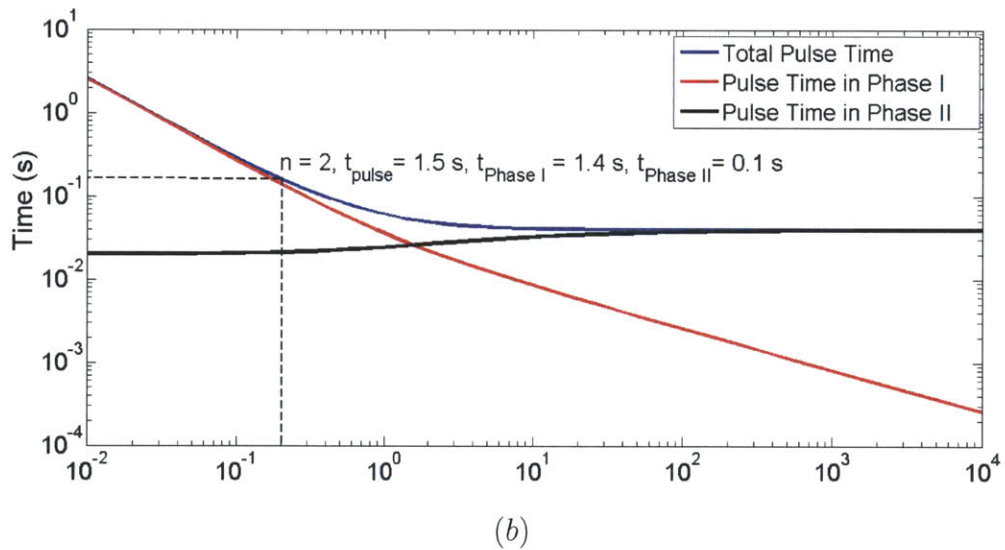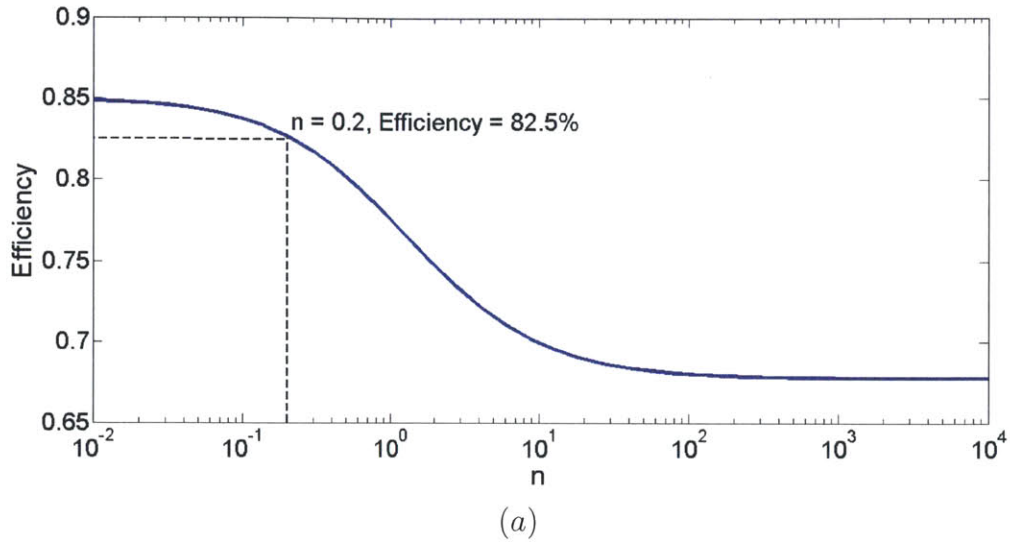
Figure 6-8: Plots of (a) efficiency, and (b) pulse time of the deadzone drive using Motor 12 with a one-stage gearbox. The maximum efficiency as $n \to 0$ is 85% which is the estimated gearbox efficiency. In such case, the pulse time also approaches infinity. With a reasonable pulse time, such as $t_{pulse} = 0.15$ s shown on the figure, an efficiency of 82.5% can be reached. This efficiency is almost as high as the efficiency with the largest motor in our study.

pulse direct drive efficiency with (2.26) and narrow down the motor list with an acceptable efficiency range.

3. Estimate the average pulse power by $P_{pulse} \approx W_{useful}/(\eta_{pulse}t_{pulse})$ and maximum speed by $\dot{\theta}_{max} = w_{optimal}A$. Compare the value with motor specifications and filter out unqualified motors.

4. Calculate the pulse period and compare it to the overall cycle time scale. We recommend the pulse period to be below one fifth of the overall cycle period. Filter out any additional unqualified motors.

5. Calculate the conventional drive efficiency, both the direct drive and the gear drive, and compare the results to the pulse drive to see if the pulse drive is still advantageous.

6. With the list of suitable motors, you need to weigh the efficiency relative to other factors such as the volume, weight and cost, depending on your own design constraint and budget. In the end the optimal motor might not necessarily be the most efficient one.

Chapter 7

Hardware Demonstration at 1 W Power Level

7.1 Overview

In this chapter, we present a simple hardware demonstration with an actual viscous load in which the load power level (1 W) resembles the operation requirements of a small robotic fish that are described in Chapter 6. The selected optimal brushless DC motor from Chapter 6 with a one-stage planetary gearbox is implemented. Both the pulse gear drive efficiency and the conventional gear drive efficiency are experimentally measured and compared. Towards the end of the chapter, we present several design ideas for more efficient packaging as well as latch mechanisms for the real fish design purposes.

7.2 Selected Design and Results

7.2.1 Operating Conditions

As a summary of Chapter 6, the target power level varies from a fraction of a Watt to several Watts. As a result, we meet the requirement by choosing the load damping in the range of 0.005 Nms/rad to 0.02 Nms/rad and load amplitude in the range of

$\pi/4$ radians to $\pi/2$ radians. The load maneuver frequency is set at 1 Hz.

7.2.2 Instrumentation and Measurements

A picture of the mechanical design is shown in Figure 7-1 and the corresponding two dimensional schematic is shown in Figure 7-2. The driver actuator, the spring and the load, are connected in series. A Maxon 386674 brushless motor is implemented as the driver motor. To simulate the fish tail propulsion, a glass syringe is used to provide a viscous damping load. The small gap between the barrel and the piston, which is approximately 7 μm, is filled with glycerin as indicated by the solid black area in Figure 7-2 The relative rotation between the syringe barrel and the piston shears the glycerin fluid and create a viscous torque proportional to the rotating speed. In this design, the piston is held fixed and the outside barrel is the rotating element. A double shaft encoder in the center measures the load position and provides bearing support for both the spring and the syringe. A beam load cell is implemented to provide torque readings by constraining the syringe piston in the axial and the rotational directions, and measuring the reaction force at a known distance. A coil spring, which can be deflected in the rotational direction to act as a rotary spring, is under tension and stretched between the motor and the shaft of the encoder. The purpose of stretching the spring is to keep the coils out of contact. Three rigid shaft couplings are used to connect between the motor shaft and the spring, the spring and the encoder shaft, and the encoder shaft and the syringe barrel. In the conventional drive configuration, a flexible shaft coupling replaces the spring to connect the driver motor shaft to the load encoder shaft, as shown in Figure 7-3. We choose this design because all motions are strictly rotational and the mechanical construction is simple. The detailed design of each of the components is described below.

Actuator

Based on the study results from Chapter 6, the Maxon EC 22 brushless DC motor with a one-stage planetary gearbox of gear ratio $N = 4.4$ is selected as the driving actuator for this load level. Its specifications are summarized in
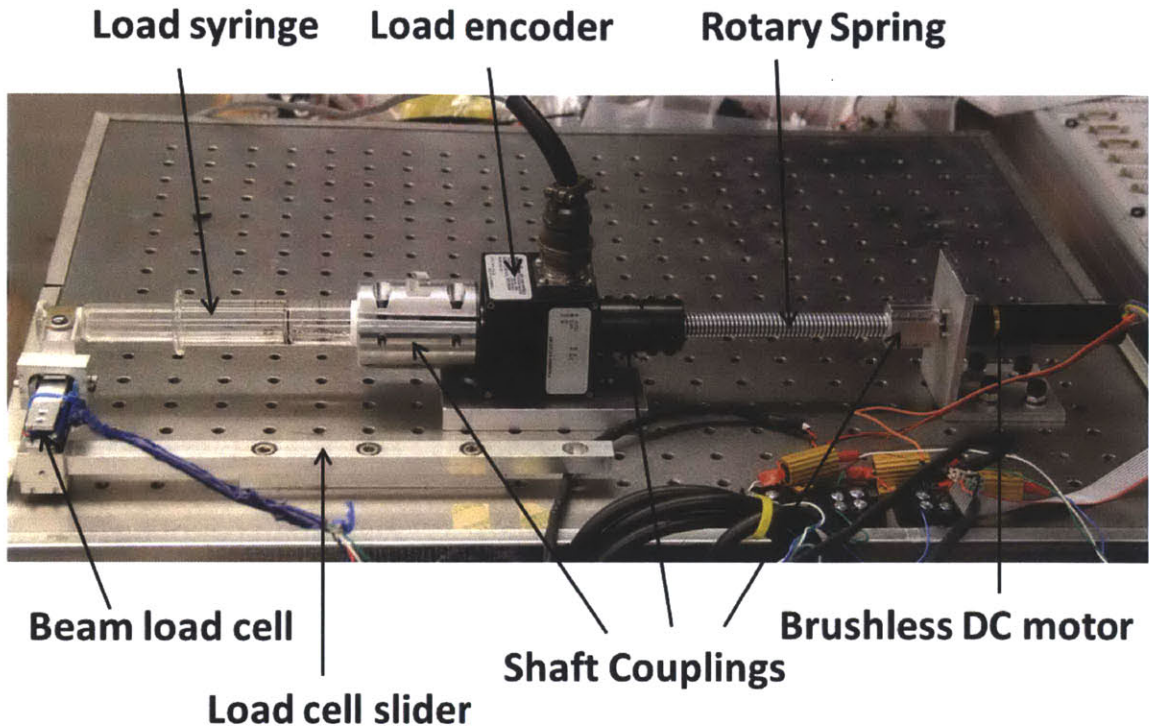
Figure 7-1: Picture of hardware demonstration at 1 W power level.

Diameter (mm)	Length (mm)	Weight (g)	P_r (W)	K_t (Nm/A)
22	62.7	128	100	7.75×10^{-3}
R (Ω)	Γ (Nms/rad)	J (kgm^2)	N	Winding
0.27	2.22×10^{-4}	4.06×10^{-7}	4.4	Y type

Table 7.1: Maxon EC-22 386674 motor specifications.

Table 7.1. The brushless motor is chosen over the brushed motor because of the advantages of no brush friction and higher power density. A optical quadrature encoder with 512 counts per revolution is integrated at the back end of the motor for motor shaft position feedback.

Spring

We choose an extension coil spring as the rotary spring for this application because of its compact volume and because it is available as a standard part. The requirements for the spring are: (1) the torsional spring constant is calculated to be approximately 0.07 Nm/rad, (2) an elastic range greater than 2π radians, (3) minimal axial spring constant for low pre-load force and (4) minimal

119
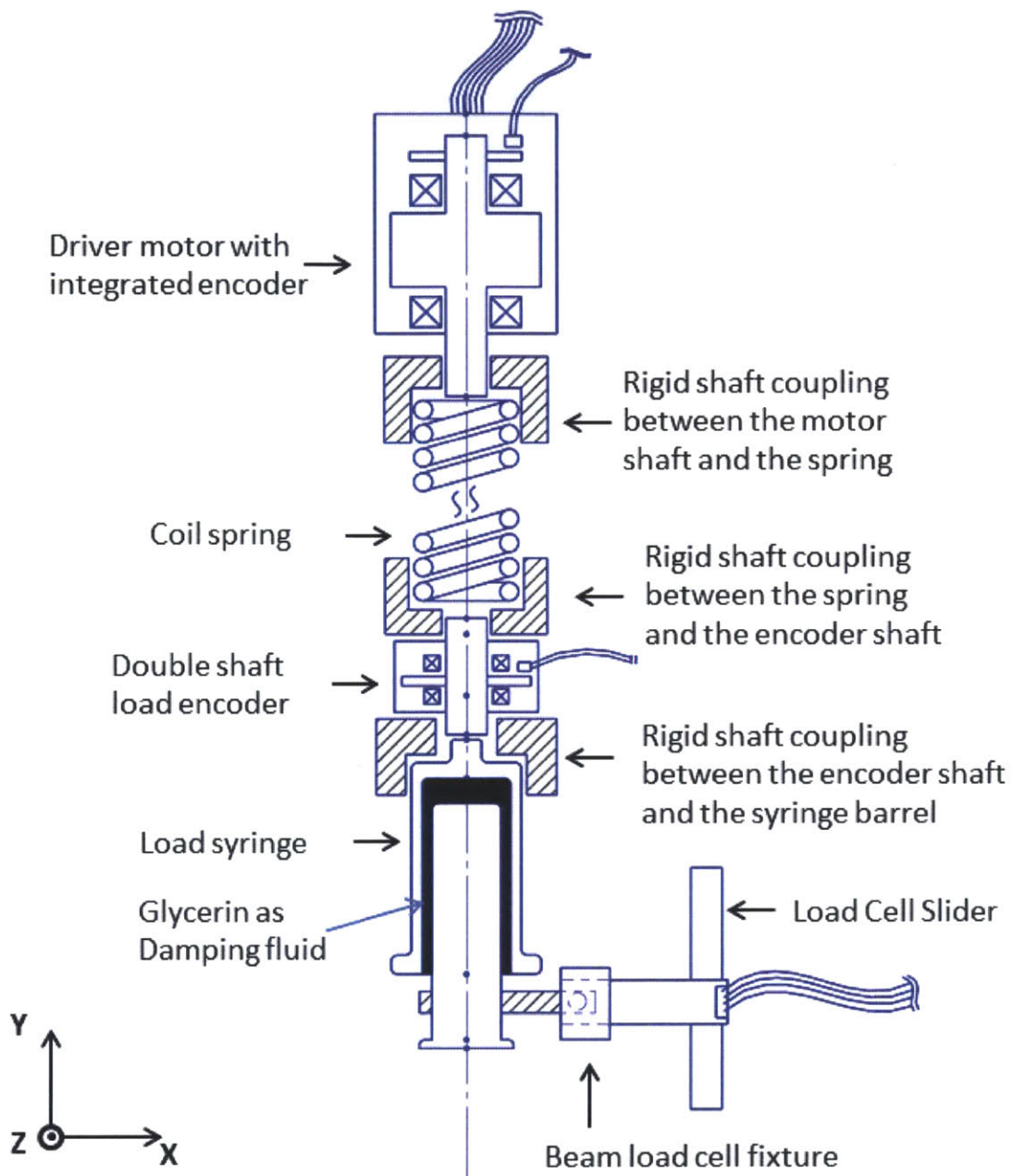
Figure 7-2: Cross-sectional schematic view of the hardware setup, not to scale. The solid black area indicates that the small gap between the syringe's barrel and piston, which is approximately 7 μm, is filled with glycerin as the damping fluid.

Flexible Shaft Coupling
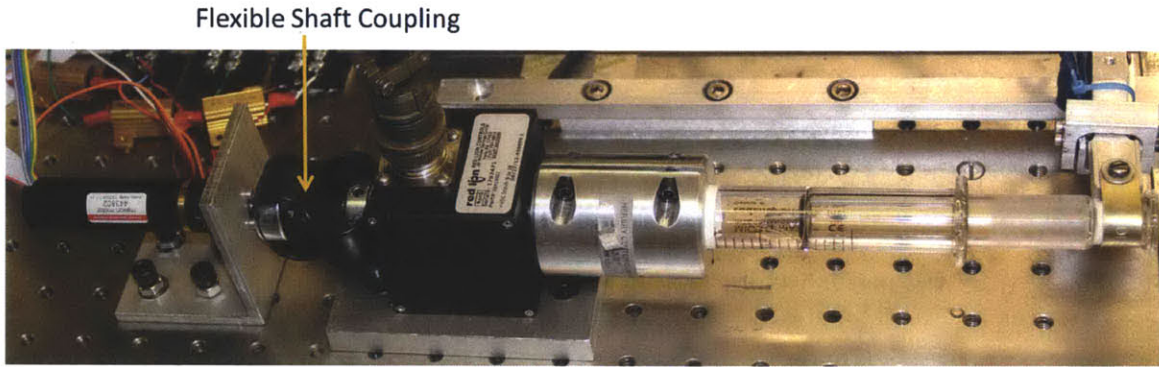
Figure 7-3: The hardware demonstration in the conventional gear drive configuration. The spring is replaced by a flexible shaft coupling.
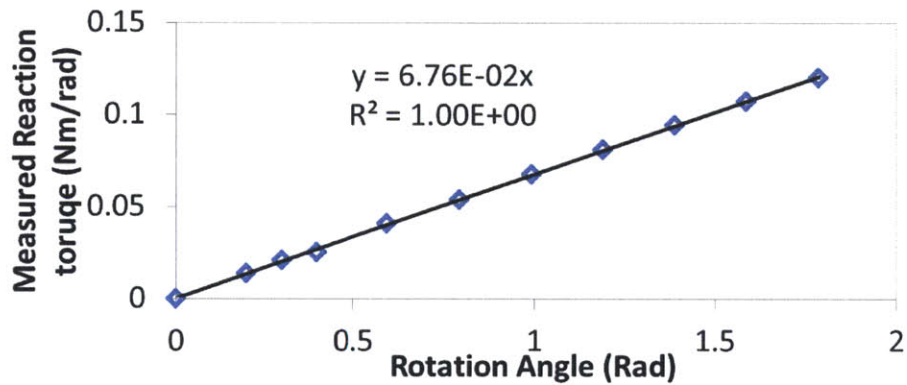
Figure 7-4: Spring calibration curve. The measured torque varies linearly with the angle of rotation. The slope indicates the calibrated spring constant to be 0.067 Nm/rad.

coil diameter to reduce rotary inertia. To find the right spring, we utilize the torsion spring calculator tool provided by Acxess Spring [3] and use common spring dimensions from the McMaster Catalog [6]. For each spring outer diameter, we vary the coil diameter and the active number of coils and calculate the spring constants and its maximum elastic range. With several iterations, we determine the optimal spring to have a mean diameter of 7.9 mm, a coil diameter of 1.6 mm and an active coil number of 40. We also experimentally calibrate the spring constant by rotating one end of the spring to a known angle and measuring the reaction torque on the other end with the beam load cell. The calibrated spring constant is 0.067 Nm/rad, as indicated by the slope of the linear fit in Figure 7-4.

Figure 7-5: Interchangeable borosilicate glass syringe.

Viscous Load

The rotary viscous load damper is made out of an interchangeable borosilicate glass syringe, manufactured by Ace Glass, part number 13680-20. The space between the barrel and the piston is filled with viscous glycerin fluid. A picture of such an interchangeable glass syringe is shown in Figure 7-5. The barrel inner diameter, piston outer diameter and length of the glass syringe used are specified as 20.407 mm, 20.393 mm and 90 mm, respectively. Thus the fluid filled gap is 7 μm. The viscous damping value can be estimated from the following equation

$$B_{load} = 4\pi\mu \frac{r_1{}^2 r_2{}^2}{r_1{}^2 - r_2{}^2} L \qquad (7.1)$$

in which μ is the dynamic viscosity of the filled fluid, r_1 is the inner radius of the barrel, r_2 is the outer radius of the piston and L is the contact length of between the piston and the barrel [10]. As indicated by the equation, the torque generated by the fluid is linear with the rotational speed, so that the damping value is only dependent on properties of the syringe and the fluid. Moreover, with such a design, the damping value can be varied by changing the filled fluid or by inserting the piston to different positions of the barrel. After some preliminary experiments with water, olive oil and glycerin, the target damping value is achieved by using glycerin and half inserting the piston ($L = 90$ mm).

Load Encoder

We use a double shaft quadrature encoder manufactured by Red Lion Controls Inc. part number ZBH10002, with a resolution of 1000 counts per revolution
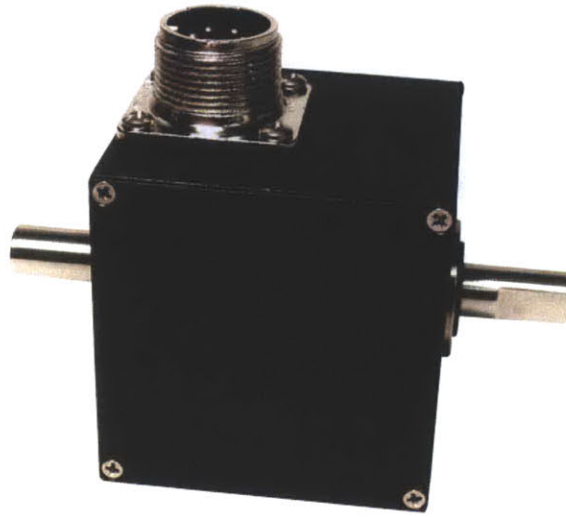
Figure 7-6: Double shaft quadrature encoder manufactured by Red Lion Controls [7]. The encoder has a resolution of 1000 counts per revolution. One end of the shaft is connected to the spring and the other end is connected to the syringe barrel.

to provide load position feedback, as shown in Figure 7-6 [7]. The double shaft mounting is chosen over other types of mounting options, such as through hole mounting or tape mounting, because a pair of bearings is required to carry the axial and radial load at the spring-syringe connection and the bearings of the encoder minimize the design work by eliminating the need for a separate bearing housing. This design also simplifies the connection between the spring and the syringe by using rigid shaft couplings on both sides of the shaft.

Beam Load Cell for Torque Measurement

There are several ways to measure the reaction torque T_{load} generated by the relative rotation between the outer barrel and the piston of the syringe. The easiest way is to measure the torque directly by clamping the stationary part of the syringe, i.e. the piston, to a reaction torque sensor. However, such method is not cost effective due to the high prices of commercial torque sensors. As a more economical alternative, we designed a bending beam load cell fixture placed at a known distance L_{load} in the radial direction from the center of the piston to measure the reaction force F_{load} so that the torque is the product of

123

Figure 7-7: A bending beam load cell product by Transducer Techniques [8].

the force and the moment arm, $T_{load} = F_{load}L_{load}$. Bending beam load cells are commonly used sensors for force measurement. For example, they are used in digital scales to measure weight. Figure 7-7 shows a picture of a bending beam load cell product by Transducer Techniques [8]. In such a load cell, four strain gages are attached to the beam so that the change of strain gage's resistance is proportional to the beam strain at the sensor location. A Wheatstone bridge circuit using the four strain gages produces a voltage signal proportional to the change of strain gage's resistance. Thus the output voltage is proportional to the applied force. Our sensing beam was extracted from a consumer scale, since this was less expensive than buying the bare element.

In our design, a 2 mm thick aluminum beam is used to bridge the piston to the load cell, with one end rigidly clamped to the glass piston through a metal loop clamp and the other end in contact with the beam load cell with a ball joint, as shown in Figure 7-8. Note that the upper contact is removed in this picture for the purpose of showing the ball joint. The ball joint is created by press fitting a 5 mm diameter ball bearing into the bridge beam. The purpose of the ball joint is to transfer reaction force to the load cell while properly constraining the six degrees of freedom of the piston. To more effectively convey our design idea, we define the horizontal radial direction of the piston as the x axis, the axial direction of the piston as the y axis and the vertical radial direction of the piston as the z axis. Such coordinate notation can be seen on Figures 7-2, 7-8 and 7-9. As shown in Figure 7-8, four degrees of freedom of the piston, x, z, θ_x and θ_z, are constrained by the barrel cylinder as rigidly connected

to the encoder, leaving only y and θ_y to be constrained by the load fixture. Figure 7-9 shows a CAD view of the load cell fixture design integrated with the ball joint and the bridge beam. The ball joint constrains θ_y as it is in point contact with the upper and lower surfaces. To constrain the movement in the y direction, a groove is milled in the x direction with 0.5 mm in depth and 1.5 mm in width on the lower surface of the upper connection piece, so that the ball joint has two point contacts with the upper connection piece and slipping in the y direction is prevented. Such contacts can be seen clearly in the cross-sectional view of the fixture assembly in Figure 7-10. An alternative design using flexures could be considered if higher accuracy was required. A slider is also designed to easily move the load cell to different y positions and thereby adjust the insert length of the piston. The output voltage from the Wheatstone bridge circuit of the bending beam load cell is amplified through an instrumentation amplifier INA 128 circuit with a gain of 50, and is read by the analog-to-digital voltage input Channel ADC 4. The connection diagram is shown in Figure 7-11. The amplified sensor signal is calibrated with dead weights of known values spanning the entire measurement range. As shown in Figure 7-12, the voltage-force relationship is linear with a slope of 0.04328 V/N.

Linear Servo Amplifier and Power Supply

The brushless DC motor is driven by a linear servo amplifier manufactured by Trust Automation, model number TA310. The power supply to the servo amplifier is manufactured by Lambda, model number LK-343-A-FM. The connection diagram of the linear servo amplifier is shown in Figure 7-13. The linear servo amplifier receives reference voltage/current signals from the digital-to-analog output channel DAC 0 of the National Instruments data acquisition board, and feeds the corresponding three-phase voltages into the brushless motor with six-step commutation. Even though PWM servo amplifiers are more commonly used due to their lower cost and higher power efficiency, we choose the linear
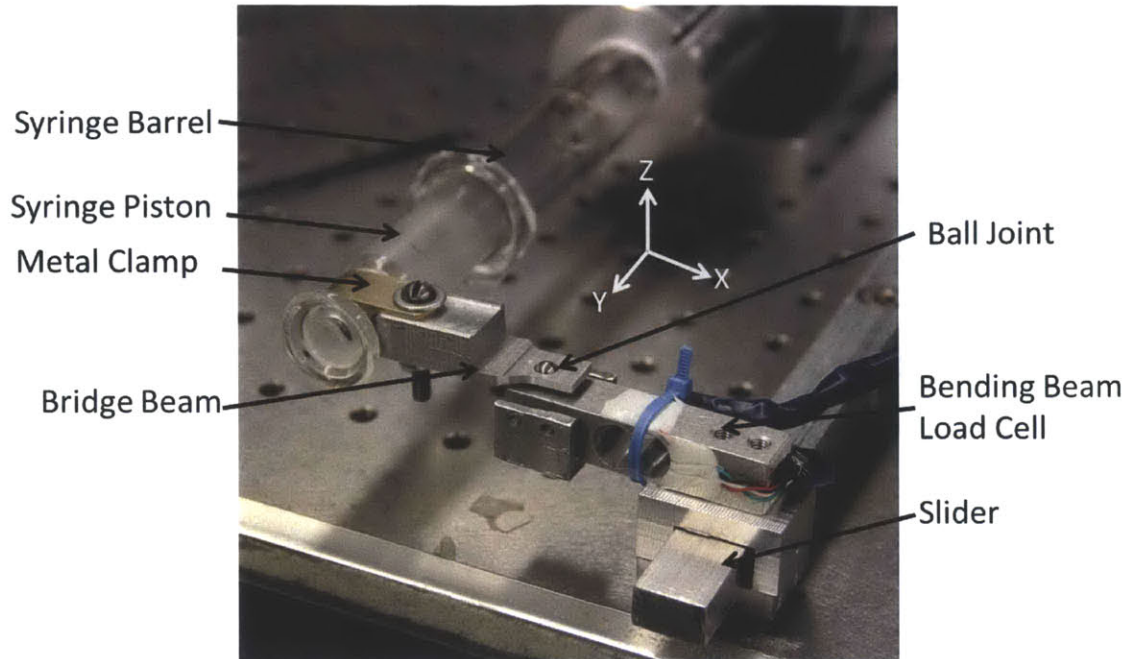
Figure 7-8: Picture of the bridge beam of the bending beam fixture design. One end of the bridge beam is rigidly clamped to the glass piston through a metal loop clamp, and the other end in contact with the beam load cell with a ball joint. The upper contact is removed in this picture for the purpose of showing the ball joint.
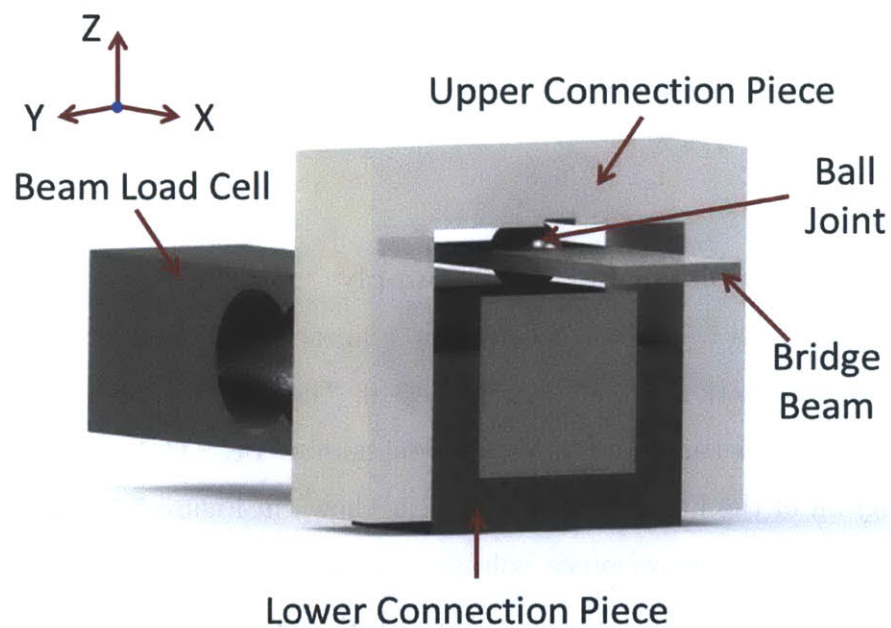
Figure 7-9: Ball joint fixture design. With the groove in the upper connection piece and the ball joint, the fixture constrains only the motions in the y and θ_y directions.

SECTION C-C

SECTION E-E

Four Strain Gages
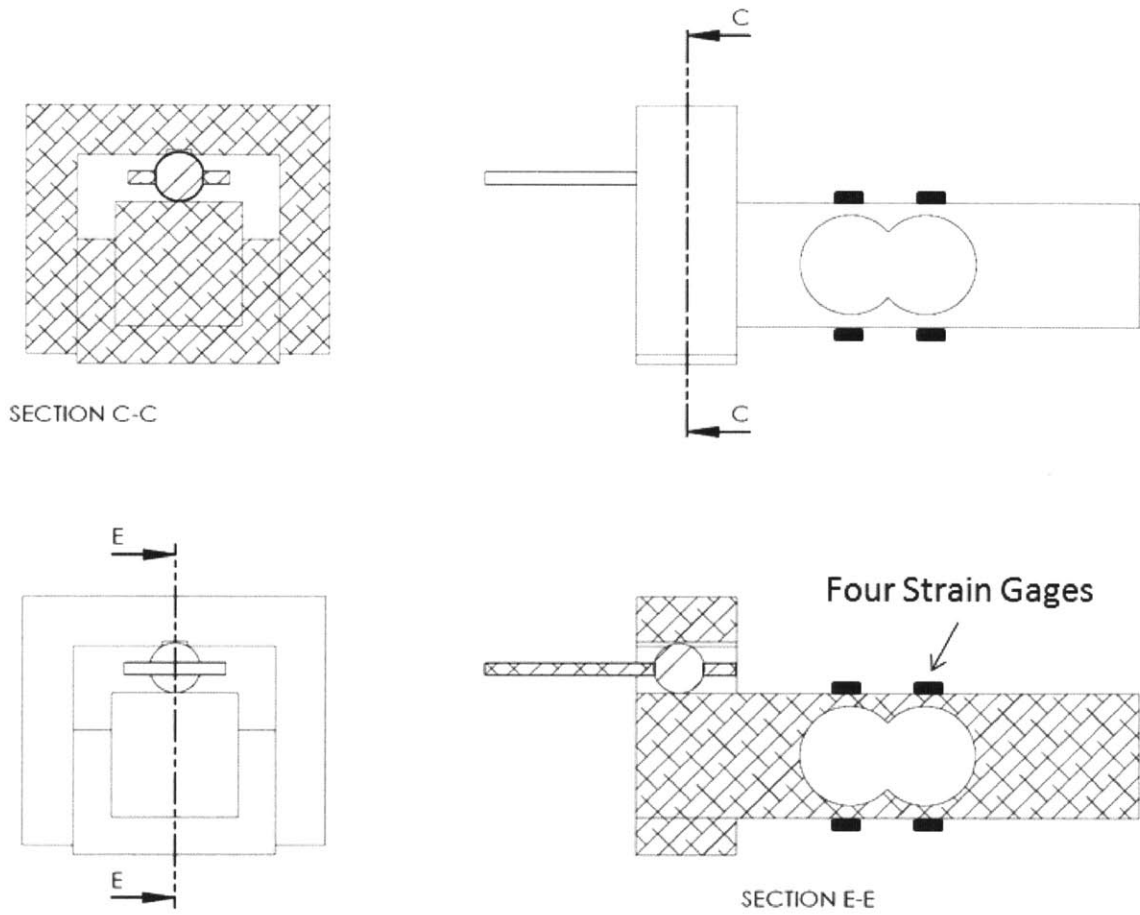
Figure 7-10: cross-sectional view of the load cell and ball joint assembly. The ball joint has one point contact to the lower surface and two point contacts to the upper surface.
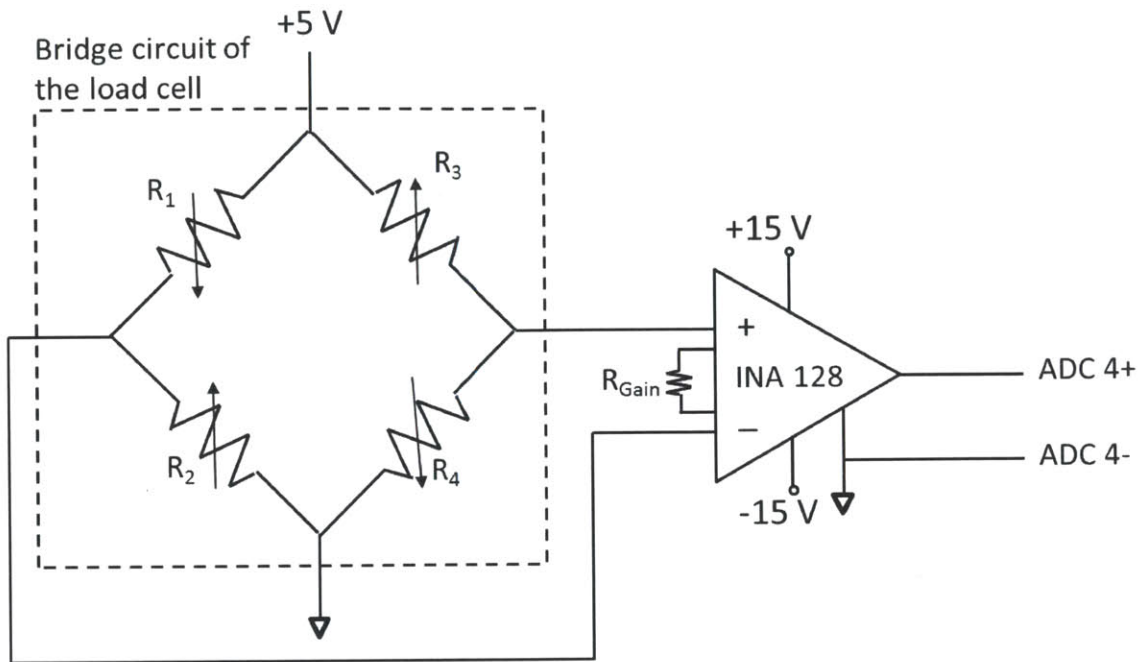
Figure 7-11: Connection diagram for the bending beam load cell voltage measurement. The bridge circuit is excited with a 5V supply voltage. With $R_{Gain} = 1$ kΩ, the differential voltage is amplified by the instrumentation amplifier with a gain of 50. The amplified signal is then read by the analog-to-digital voltage input channel ADC 4 of the National Instruments data acquisition board. At zero strain, nominally $R_1 = R_2 = R_3 = R_4$.
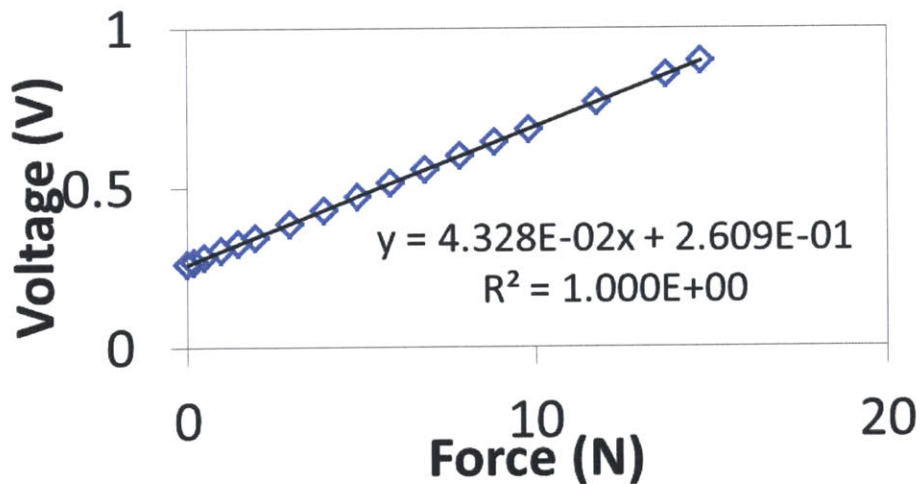
Figure 7-12: Beam load cell voltage-force calibration. The measured voltage varies linearly with the applied force. The measured slope is 0.04328 V/N.
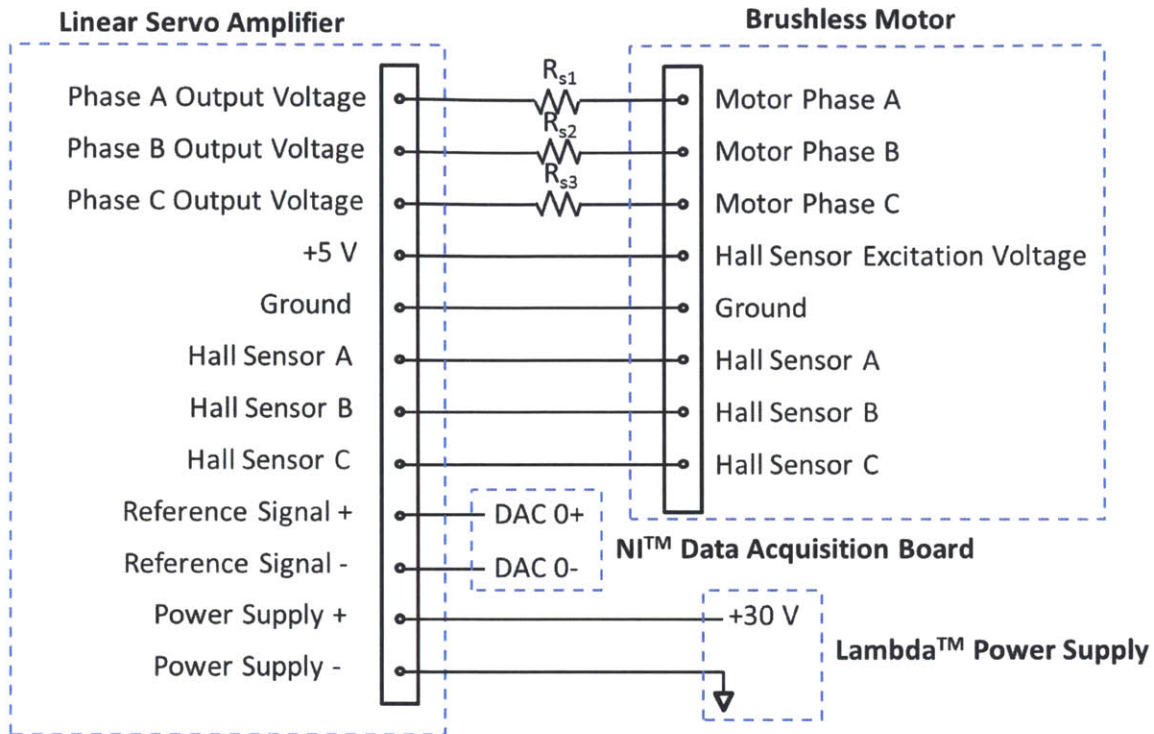
Figure 7-13: Connection diagram for the linear servo amplifier. Resistors R_{s1}, R_{s2}, and R_{s3} are used for phase current sensing.

servo amplifier over a PWM servo amplifier in our demonstration for more accurate measurements. With a PWM servo amplifier, the ADC sampling rate needs to be at least twice as the PWM pulse frequency in order to capture every pulse without aliasing, which raises the requirements for data acquisition card. In addition, such measurements are subject to high frequency noise introduced by the PWM pulses. However, for actual robotic fish design, we recommend a PWM servo amplifier to reduce the power electronics energy consumption.

Input Motor Power Measurement Circuit

Since the driver motor is a balanced three-phase brushless motor, the input motor power can be monitored by measuring the phase-to-phase voltages and currents of two of the three phases. Figure 7-14 shows a schematic of the motor circuit. The motor has a Y connected winding with A,B, and C being the three terminals. Each leg is connected with a series 0.1 Ω power resistor $(R_{s1} = R_{s2} = R_{s3} = 0.1\ \Omega)$ for current sensing. The input power to the motor

is the sum of the powers of the three legs

$$P_{input} = P_A + P_B + P_C = V_{AO}I_A + V_{BO}I_B + V_{CO}I_C. \tag{7.2}$$

By recognizing that $I_A + I_B + I_C = 0$ at the junction O and replacing $V_{AO} = V_{AC} - V_{OC}$ and $V_{BO} = V_{BC} - V_{OC}$, the power equation above can be rewritten as

$$\begin{aligned} P_{input} &= (V_{AC} - V_{OC})I_A + (V_{BO} + V_{BC} - V_{OC})I_B + V_{CO}(-I_A - I_B) \\ &= V_{AC}I_A + V_{BC}I_B. \end{aligned} \tag{7.3}$$

Therefore, by measuring the differential voltage of V_{AC}, V_{BC}, and the sense resistor voltages $V_{A'A}$ and $V_{B'B}$ such that $I_A = V_{A'A}/R_{s1}$ and $I_B = V_{B'B}/R_{s2}$, we are able to obtain the instantaneous input motor power using (7.3). Figure 7-15 shows the schematic of the measurement circuit and the connection interface with the National Instruments hardware. In our experiment, with the power supply voltage of the linear servo amplifier being 30 V, the voltage levels of V_{AC} and V_{BC}, and the common-mode voltages of $V_{A'A}$ and $V_{B'B}$ exceed the allowable voltage measurement levels of the data acquisition board, which is 10 V. In order to resolve this issue, we used three resistive voltage divider circuits to scale down V_{AC} and V_{BC} so that the voltages at A'', B'' and C'' are scaled down by a factor of $\frac{R_1}{R_1+R_2}$ from the voltages at A, B and C, respectively. Thus, the differential voltage measurements of $V_{A''C''}$ at the analog-to-digital input voltage channel ADC 0, and $V_{B''C''}$ at the analog-to-digital input voltage channel ADC 1 have the following relationship with the target voltages V_{AC} and V_{BC},

$$V_{AC} = \frac{R_1 + R_2}{R_1} V_{A''C''}, \tag{7.4}$$

$$V_{BC} = \frac{R_1 + R_2}{R_1} V_{B''C''}. \tag{7.5}$$

Here the chosen R_1 and R_2 are 1000 Ω and 2000 Ω. We also constructed two difference amplifier circuits using two unity gain difference amplifiers AD-629
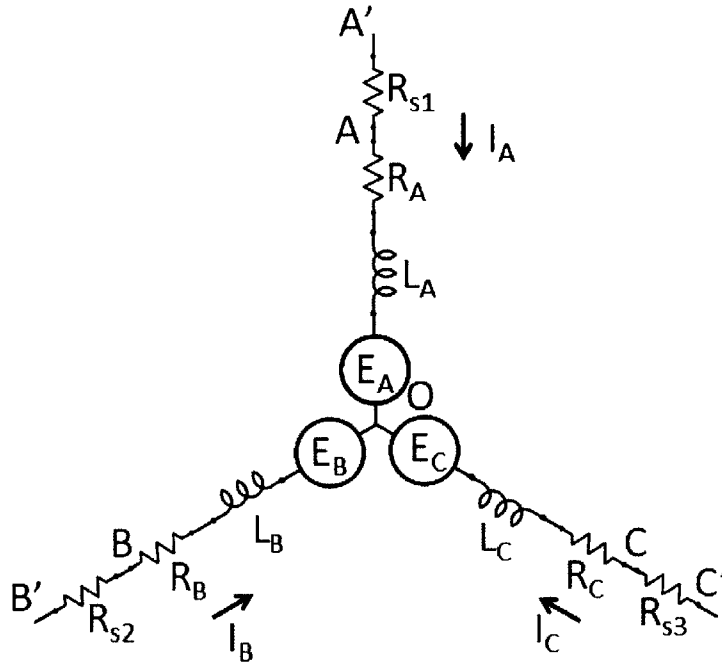
Figure 7-14: Schematic of Maxon brushless DC motor Y connected three phase windings. A current sensing resistor is connected to the end of each phase.

by Analog Devices to reject the high common-mode voltages of $V_{A'A}$ and $V_{B'B}$. Thus the measured voltages $V_{A'''}$ at input channel ADC 2, and $V_{B'''}$ at input channel ADC 3 are equal to the target voltages $V_{A'A}$ and $V_{B'B}$. The currents I_A and I_B are interpreted as

$$I_A = \frac{V_{A'''}}{R_{s1}}, \tag{7.6}$$

$$I_B = \frac{V_{B'''}}{R_{s2}}. \tag{7.7}$$

All the resistors used in the circuit are experimentally measured, and the measured value are used in calculations to ensure accuracy.

Digital Controller and Data Acquisition Module

As in previous chapters, the control and data acquisition tasks are performed by a National Instruments PXI-8133e real-time target and PXI-6259 data acquisition board in a PXI-1071e chassis. A LabView VI is written in LabView 2011 to implement the digital control algorithm, communicate with all the in-
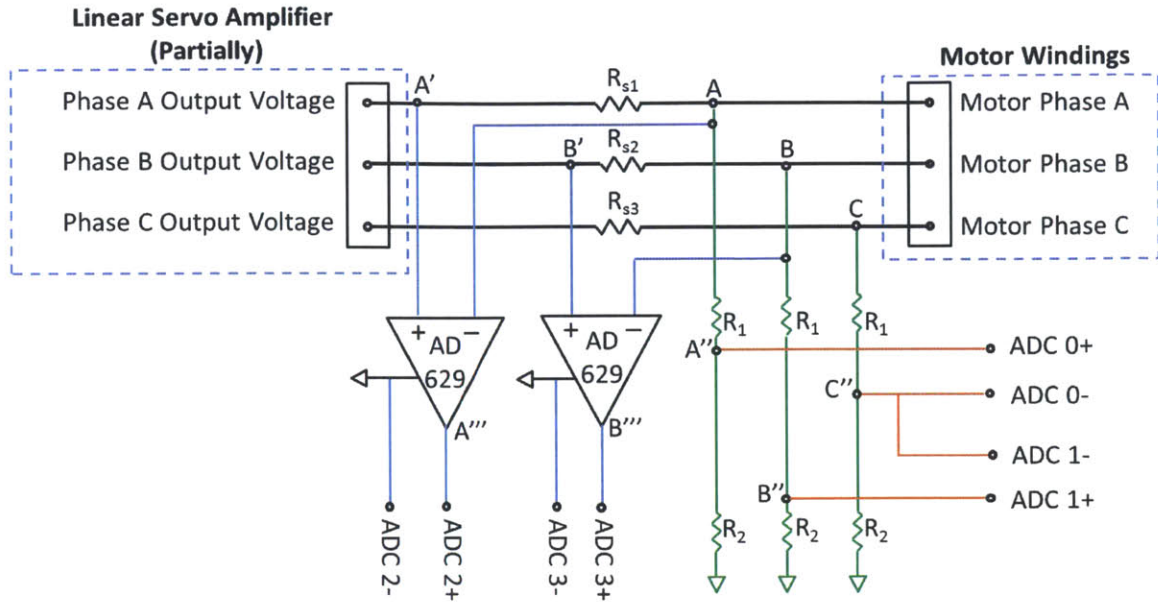
Figure 7-15: Connection diagram for input motor power measurement.

put/output channels and record data. Five analog-to-digital input channels ADC 0 to ADC 4 are assigned to measure the brushless motor phase-to-phase voltages and currents as well as the voltage from the beam load cell, as can been seen from previous sections. Two digital counters are configured for reading the two position encoder inputs. One digital-to-analog output channel DAC 0 is dedicated to output the current control command to the linear servo amplifier.

The experiments of both the pulse gear drive and the conventional gear drive are performed at five load angle amplitude levels ranging from $\pi/4$ radians to $\pi/2$ radians. In the conventional gear drive configuration, the same driver motor with the same gearbox is used while the spring is replaced with a flexible shaft coupling, as shown in Figure 7-3. The total input energy and useful work are calculated by numerically integrating the instantaneous total input power and load power over one cycle. Thus the energy efficiency is calculated as the useful work divided by the total input energy. We again make the assumption that an ideal clamp can be designed and thus that power dissipation can be ignored in the "clamp" portion of the cycle. Each measurement is repeated twice to get an average efficiency value. The simulation is run at the same amplitudes with an estimated viscous damping value of 0.015 Nms/rad

from (7.1). In addition, a single gearbox efficiency value of 0.85 is used for the pulse gear drive simulation and 0.9 is used for the conventional gear drive simulation. The lower gearbox efficiency for the pulse drive simulation accounts for the added viscous loss due to the higher motor speed.

7.2.3 Results and Discussion

Energy Efficiency Results

The measured, simulations and analytical calculated energy efficiency results are plotted in Figure 7-16. The analytical results are obtained using (3.22) for the pulse drive and (3.26) for the conventional drive. The power levels are labeled with each efficiency value. At each load amplitude, the power dissipation on the load of the pulse drive and the conventional drive are similar. Significant efficiency gain of the pulse drive over the conventional drive is observed in both simulation and experimental results. The measured pulse drive energy efficiencies are scattered around 70 % at all amplitude levels while the measured conventional drive energy efficiencies increases from 10% at the lowest amplitude to 15% at the highest amplitude.

Instantaneous Power, Voltage and Current Comparison

We also compare the power, voltage and current levels for the two types of operations. Figure 7-17 shows the instantaneous power, the instantaneous phase-to-phase voltages V_{AC} and V_{BC}, and the instantaneous phase-to-phase currents I_A and I_B during a half work cycle for the case of $\pi/2$ load amplitude. We observe that the maximum input power for the pulse drive is 20 W, approximately 5 W higher than the maximum input power required for the conventional drive. The maximum current for the pulse drive is approximately one half of the conventional drive while the maximum voltage is almost three times higher. Therefore in this demonstration, the high efficiency of the pulse drive is obtained by operating the motor at a low torque and high speed mode as well as shorter duration, while the low efficiency of the conventional drive is a result of operating in a high torque and low speed mode.
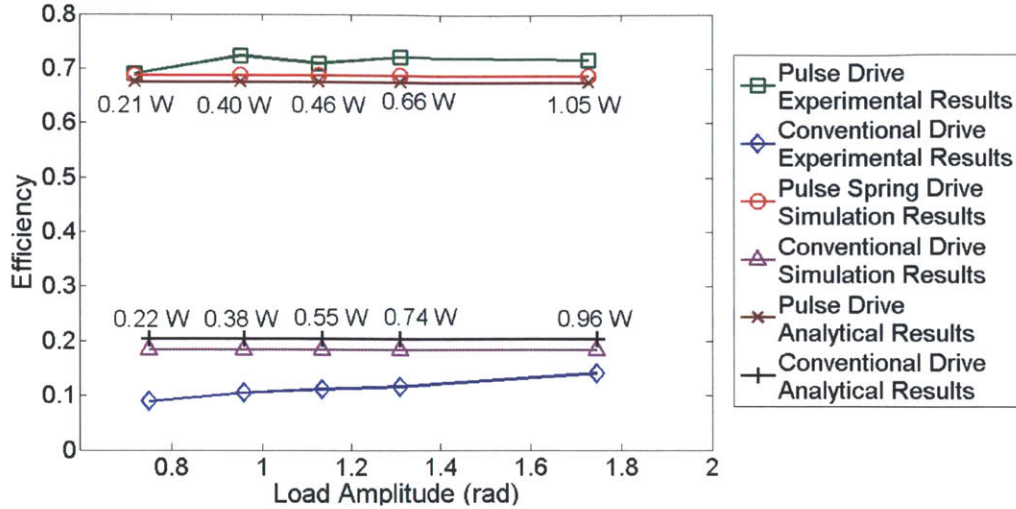
133

Figure 7-16: Plots of energy efficiency for both the pulse gear drive and the conventional gear drive. A single stage gearbox with a ratio of 4.4 is used for both the pulse drive and the conventional drive. The measured pulse gear drive achieves approximately 70% energy efficiency while the measured energy efficiency of the conventional drive ranges from 10% to 15%.

Comments on Gearbox Efficiency and Other Losses

Similar to Chapter 5, we find using single gearbox efficiency values a reasonable approximation in the simulation when we compare the simulation results to the measured results. The maximum efficiency difference in between the simulation and measurement are 3 % for the pulse drive and 10 % for the conventional drive. There are three factors contributing to the difference. One is that the load damping value in simulation is only an estimate based on the viscosity of glycerin at 25° C which can change with temperature variations. The power dissipated in the syringe will raise the fluid temperature thus decrease the viscosity of the fluid. The second factor is that the experimental gearbox efficiency differs from the simulated ones. A third factor could be other unmodeled losses. First we assume the gearbox loss to be the only loss besides the coil resistive heat loss and estimate the gearbox efficiency. As a result, the gearbox efficiency is calculated as $(Useful\ Work)/(Total\ Energy - Coil\ Heat\ Loss)$. As shown in Figure 7-18, the calculated efficiencies all fall in a reasonable range bounded by 70% and 95%. In contrast to the gearbox efficiency results obtained in Chapter 5, the pulse drive actually results in a better gearbox efficiency, approximately 90% for

134
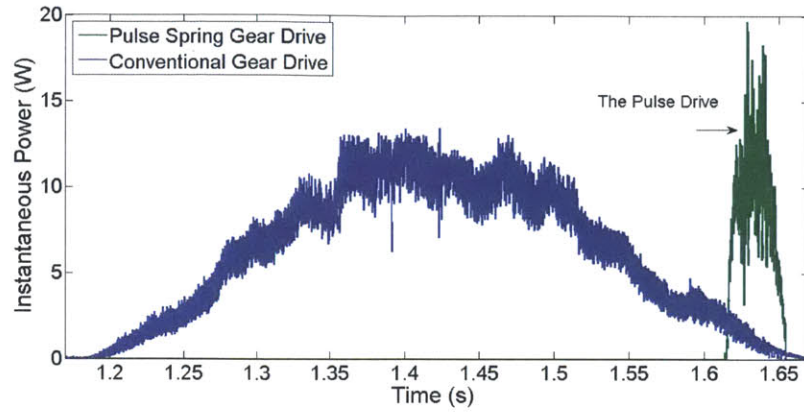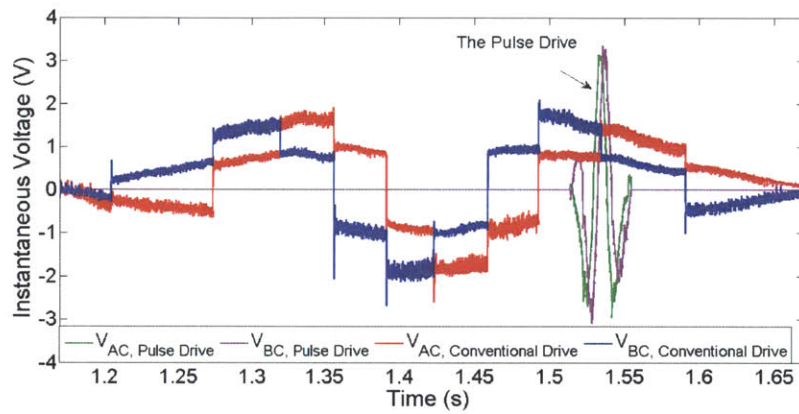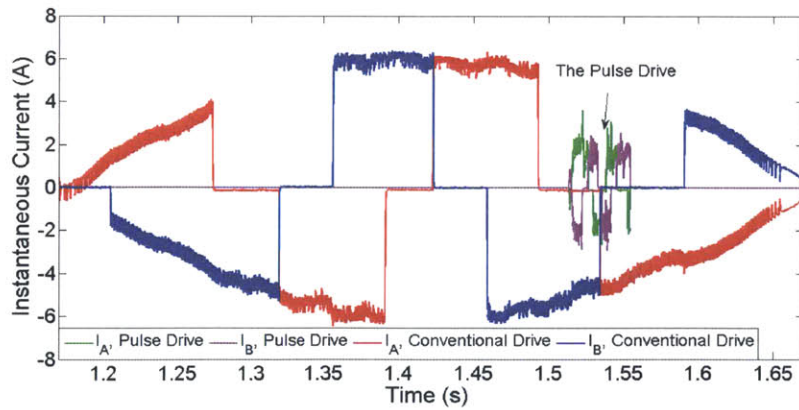
Figure 7-17: Plots of driver motor operating conditions: (a) instantaneous power, (b) instantaneous phase-to-phase voltages and (c) instantaneous phase-to-phase currents for the two drives. Note that the plots of the two drives in each figure are not time synchronized due to the difference in the starting time of data logging. The sudden switches in the voltage and current plots are the results of the six-step commutation. The maximum power levels are similar in the two drives. However, the pulse gear drive has lower current levels but higher voltage levels than the conventional gear drive indicating it is operating in a low torque and high speed mode.
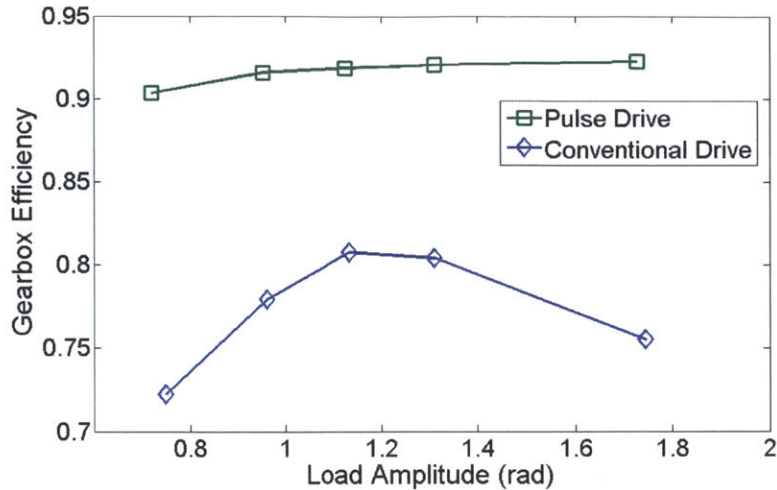
Figure 7-18: Plots of estimated experimental gearbox efficiency. The gearbox efficiency is above 90% for the pulse drive and in between 70% and 80% for the conventional drive.

all load levels, than those of the conventional drive, which range from 72% to 80%. As seen from the previous section, the torque level for the pulse drive is lower but the speed level is higher. Since both higher torque and speed can increase the gearbox loss, we postulate that the torque might have a much larger effect than the speed in this case.

We also examine possible frictional losses in the load fixture, i.e. the load encoder, syringe and the torque measurement fixture, by comparing the averaged work delivered by the spring and the averaged useful work done by the viscous damper in one cycle. The instantaneous torque on the spring is calculated as the measured torsional spring constant multiplied by the instantaneous deflected angle. Thus the work delivered by the spring is calculated by numerically integrating the instantaneous spring torque over the load displacement. As shown in Figure 7-19, the difference between the spring work and the damper work are within 2% with the spring work being consistently higher. The possible source of loss, we believe, comes from the load encoder bearings frictional loss. Since viscous friction increases with speed, the loss increases with the load amplitude.
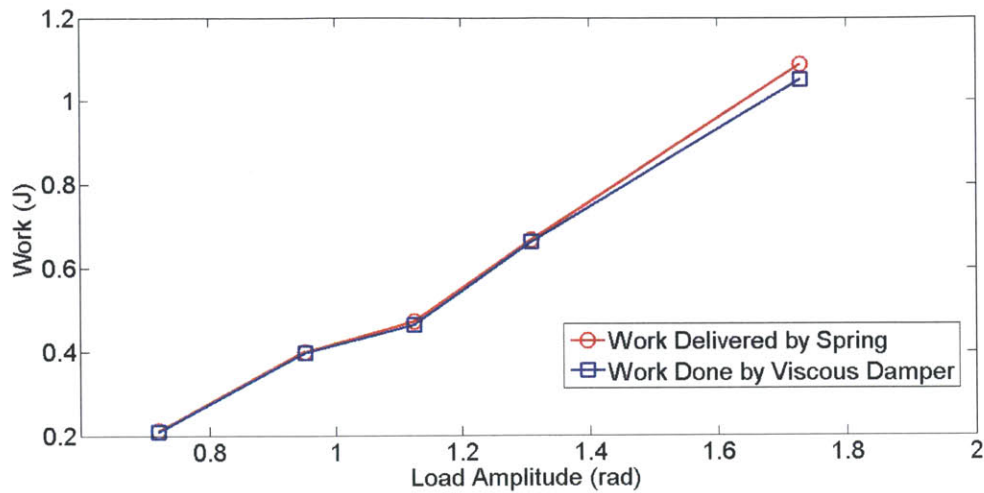
Figure 7-19: Plots of energy delivered by the spring and the useful work done by the load damper. The two sets of data agree well indicating that the loss in the load fixture is negligible.

7.2.4 Discussion

In this hardware demonstration in which a viscous rotary damper is used to simulate the robotic fish tail propulsion, we achieve high efficiency of 70% with the pulse gear drive by using a brushless DC motor with one-stage planetary gearbox. The efficiency of the corresponding conventional drive with the same gearbox is 15% at maximum. By comparing the power, voltage and current levels, we conclude that the much higher efficiency of the pulse drive is achieved by operating the driver motor in a low torque and high speed mode. The results have several implications.

First, the experimental efficiency results verify the analytical predictions and simulation results, as shown in Figure 7-16. Therefore, both the analytical derivations and the corresponding simulations presented in Chapter 3 are demonstrated to be useful design tools to estimate the energy efficiencies as well as the corresponding voltage, current and power levels. In the same sense, the results also validate the motor selection approach by using the analytical calculations in Chapter 6. It would be costly and time consuming to construct the hardware demonstration for each of the motors in Figure 6-7. By demonstrating the efficiency for one motor, it is sufficient to conclude that the calculated efficiency holds true for all the motors.

Second, we demonstrate that the pulse drive can be scaled to different power levels. In our first demonstration, the lowest power level is 0.01 W and the highest power level in the third demonstration is over 1 W. Depending on the power requirements of the application, a suitable actuator can be selected by following the guideline presented in Chapter 6. We also show that high efficiency can be achieved by the pulse drive with a direct connected configuration or with a one-stage gearbox. Thus a major advantage introduced by the pulse drive is that the system is back-drivable because the reflected impedance of the motor is low. In addition, the deadzone drive we presented in Section 3.5.3 has the potential to achieve even higher efficiency than the pulse drive with sinusoidal displacement trajectory. This remains a subject for future work.

One missing piece in the hardware demonstration is the lack of a latch mechanism because of the time constraints on this project. We present two preliminary designs for the latch mechanism in the next section. We also foresee a design challenge of efficiently packaging the spring when integrating the pulse drive to actual robotic designs. In our simple demonstration, the actuator and the spring are unwrapped in series. Although the total volume is small, it is by no means a compact design. Therefore, we include several preliminary ideas for packaging springs as a final note of this chapter. These are future design challenges.

7.3 Preliminary Latch Design

There are several ways to design a latch mechanism. The crank-shaft transmission described in Chapter 3 is one design concept that doesn't require energy dissipation during the latch phase. In this section, we provide some testing ideas for the pulse drive with a crank-shaft transmission, and two additional latch mechanism design ideas with hand-sketched drawings.

- Figure 7-20 shows a pulse drive fish tail concept with a double-shaft motor and crank-shaft transmissions. The crank-shaft transmissions are installed on both sides of the motor on a common through shaft and thus rotating together. Both
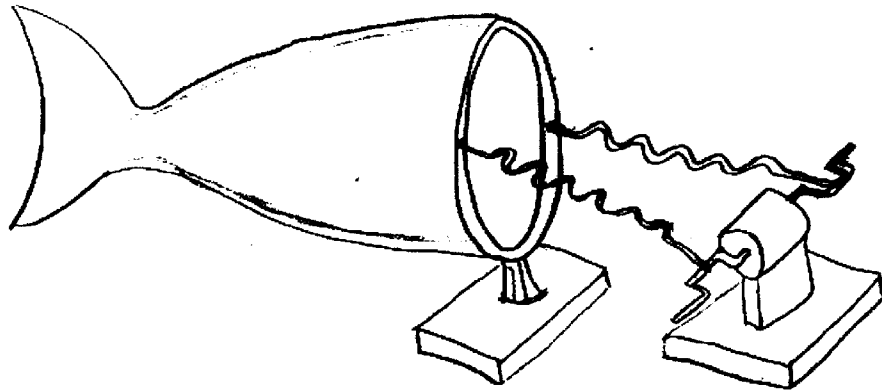
Figure 7-20: A pulse drive fish tail testing set up with a double-shaft motor and crank-shaft transmissions. The crank-shaft transmissions are installed on both sides of the motor. Both coil spring are preloaded in tension at the neutral position. In operation, the two cranks are pulsed to rotate 180° out of phase. After the pulse is applied, as shown in the figure, the tension in one spring is greater than the other, thus applying a net moment to the fish tail. The kinematics supply the latching function.

coil spring are preloaded in tension at the neutral position. When the set-up is in operation, the two cranks are 180° out of phase. When the two springs reach latch position after the pulse is applied, as shown in the figure, the tension in one spring is greater than the other, thus applying a net moment to the fish tail. The kinematics supply the latching function.

- Figure 7-21 shows a similar set up with a single shaft motor. The two crank-shaft transmissions are installed on the same side of the motor. The operation principle is the same as the previous one. Compared to the previous design idea, this design is more compact and doesn't require a double shaft motor. However, the drawbacks are that the rotation is limited to half a revolution, and that at the latch position shown in the figure, the moment of the spring force to the motor is not exactly zero which requires additional position holding current.

- Figure 7-22 shows a latch mechanism which uses friction. A non-magnetic flywheel is attached to the driver motor shaft. A solenoid and a permanent magnet attached with an extension spring form the latch and release mechanism.
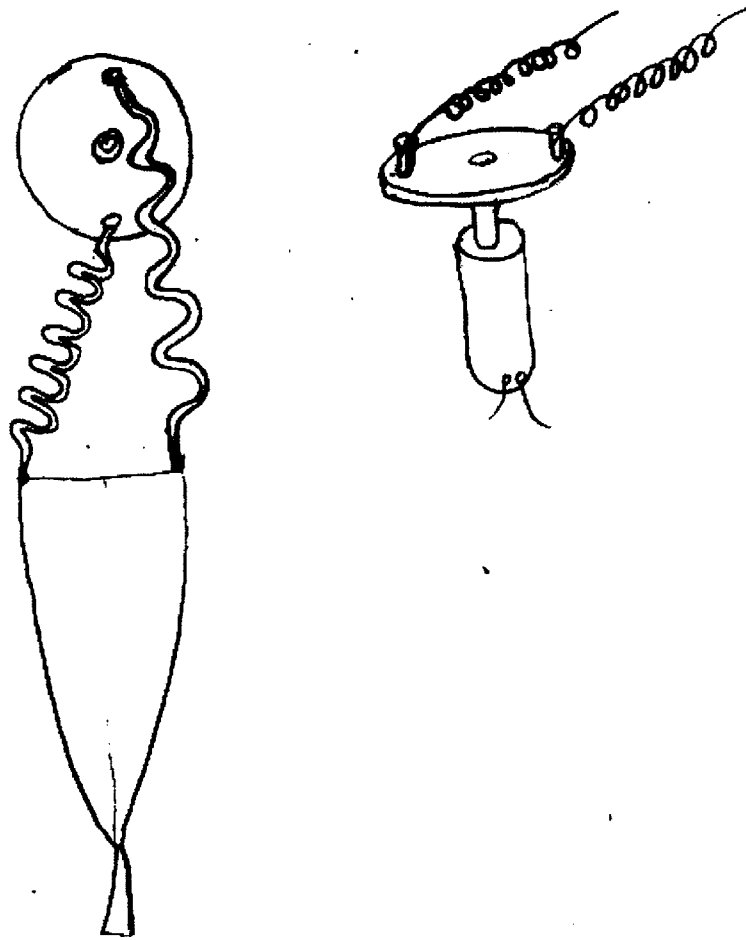
139

Figure 7-21: The crank-shaft transmissions are installed on the same side of the motor. The operation principle is the same as the previous one. Compared to the previous design idea, this design is more compact and doesn't require a double shaft motor.
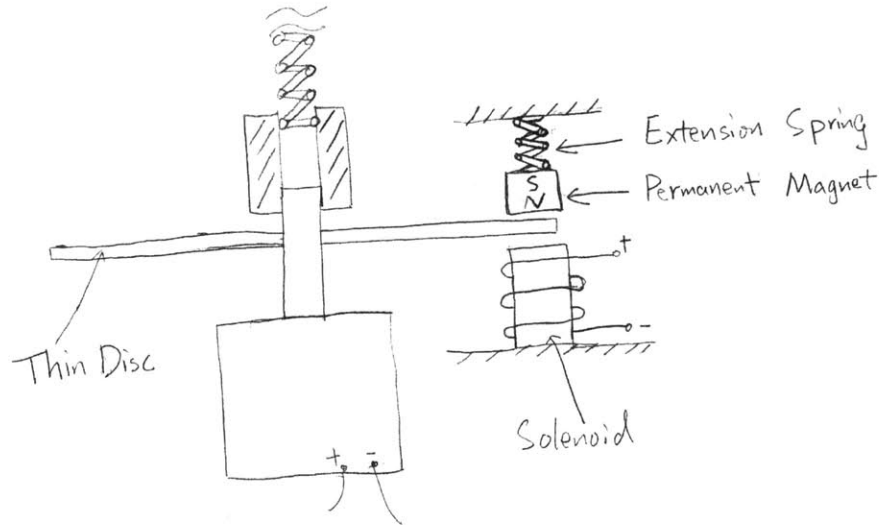
Figure 7-22: Latch by friction. A non-magnetic flywheel is attached to the driver motor shaft. A solenoid and a permanent magnet attached with an extension spring form the latch and release mechanism.

During the latch phase, current in the solenoid flows from the positive terminal to the negative terminal and attracts the permanent magnet thus locking the flywheel in between with static friction. During the release phase, the current is stopped or reversed so that the extension spring pulls the magnet back to release the flying wheel.

- Figure 7-23 shows a third latch idea with gear meshing. A gear is attached to the motor shaft and a partial gear with the same pitch is attached to a torsion spring and a permanent magnet. A similar solenoid-magnet-spring configuration is implemented to perform latch and release alternation. During the latch, all the torque on the motor is counter balanced by the torsion spring in the tangential direction with the tensile/compression stress of the spring material.

7.4 Preliminary Spring Packaging Design

In this section, we present four preliminary concepts with hand sketches for efficiently packaging the energy storage spring. The first concept is to package the spring in parallel with the motor, as shown in Figure 7-24. A gear pair can be used to connect
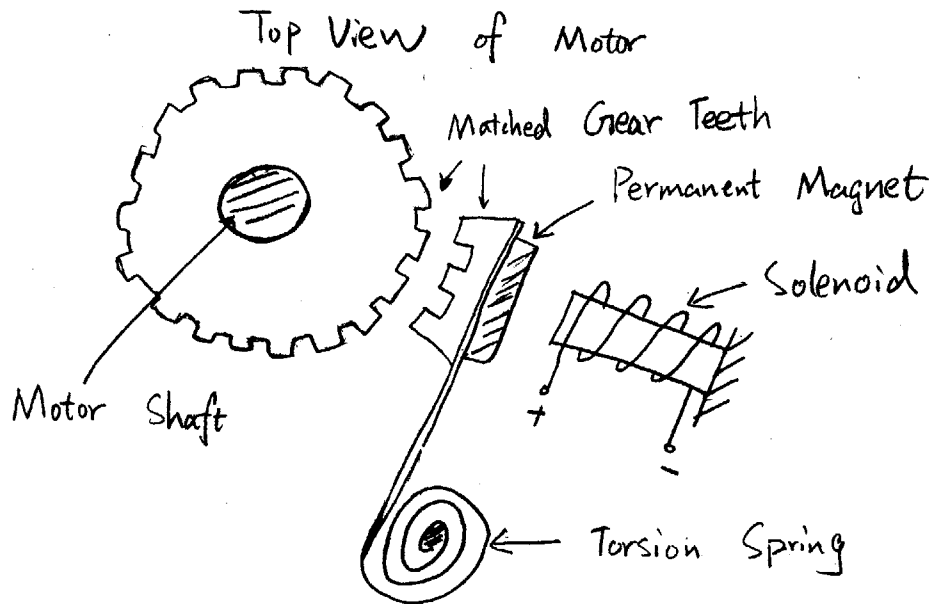
141

Figure 7-23: Latch by gear teeth. A gear is attached to the motor shaft and a partial gear with the same meshing is attached to a torsion spring and a permanent magnet.

between the motor and the spring. Such design reduces the aspect ratio (ratio of axial length to diametrical width) of the motor-spring pair. It is suitable when there is limited space in the motor axial direction but abundant space in the diametrical direction. It also integrates the gears as part of its packaging. The second idea is to package the coil spring over the motor package, as shown in Figure 7-25. This design concept eliminates the space of the spring thus it is suitable for a tight space. It can also change the direction of motion. However, bearing support at the output end of the spring is needed. The third idea is to package multiple springs with different diameters concentrically, as shown in Figure 7-26. This design reduces the the axial length without changing the direction of motion. It is useful when the robotic application requires the actuator, spring and the load to be aligned in the same axial direction.

Figure 7-27 shows a design concept where we envision the fish rib to be fabricated out of elastic materials, thus the spring element is integrated as part of the fish structure. The front view and the top view show one link of the rib with the center as the pivot point. By bending one end of the rib to one direction, and the other end to the other
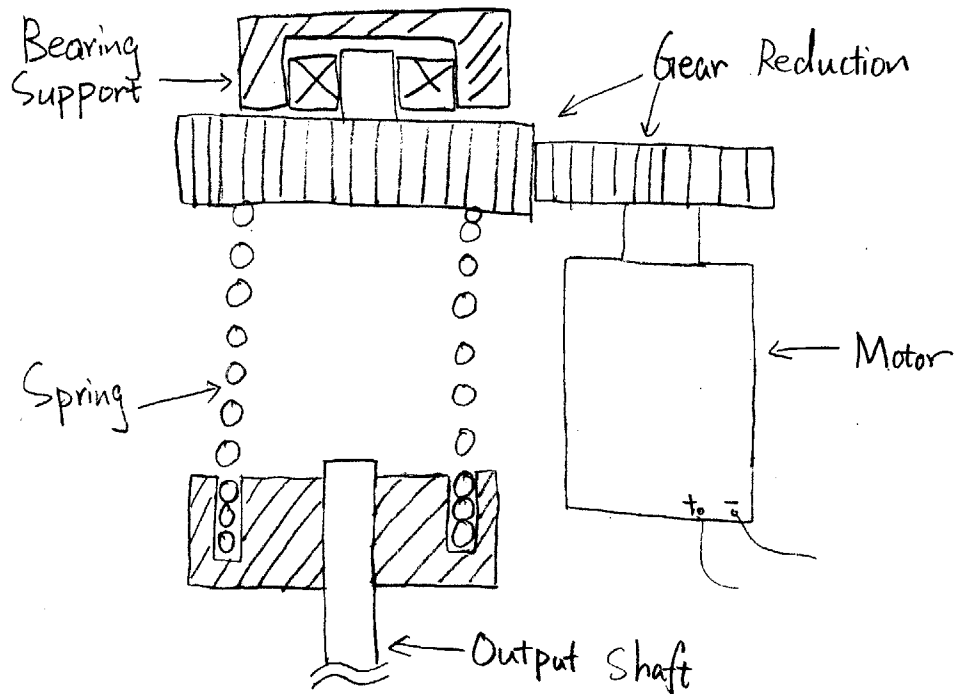
Figure 7-24: Spring packaging design concept 1: spring in parallel with the driver motor. A gear pair is used to connect between the motor and the spring.

direction, a net moment can be applied to the link. Such a fish rib design can be also integrated with a crank-shaft transmission using a double-shaft motor, as shown in the top view. With the two cranks rotating 180° out of phase, the two ends of the ribs can be bent to the opposite direction to create the net moment on the link.

7.5 Summary of the Chapter

- We designed and constructed a pulse gear drive hardware demonstration that simulates the robotic fish tail propulsion.

- The experimentally measured pulse drive efficiency is significantly higher than the efficiency of the conventional drive with the same driver motor and the same gearbox.

- Studies on power, voltage and current show that the drive motor is operating in a low torque and high speed mode, resulting in relatively
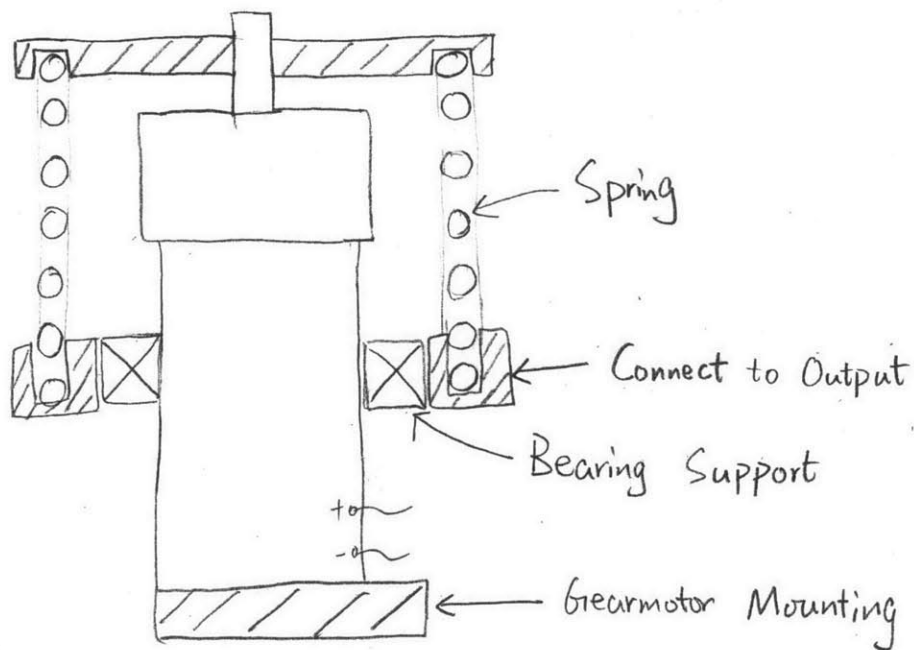
Figure 7-25: Spring packaging design concept 2: spring packaged over the driver motor. This design concept eliminates the separate space of the spring thus it is suitable for tight packaging.
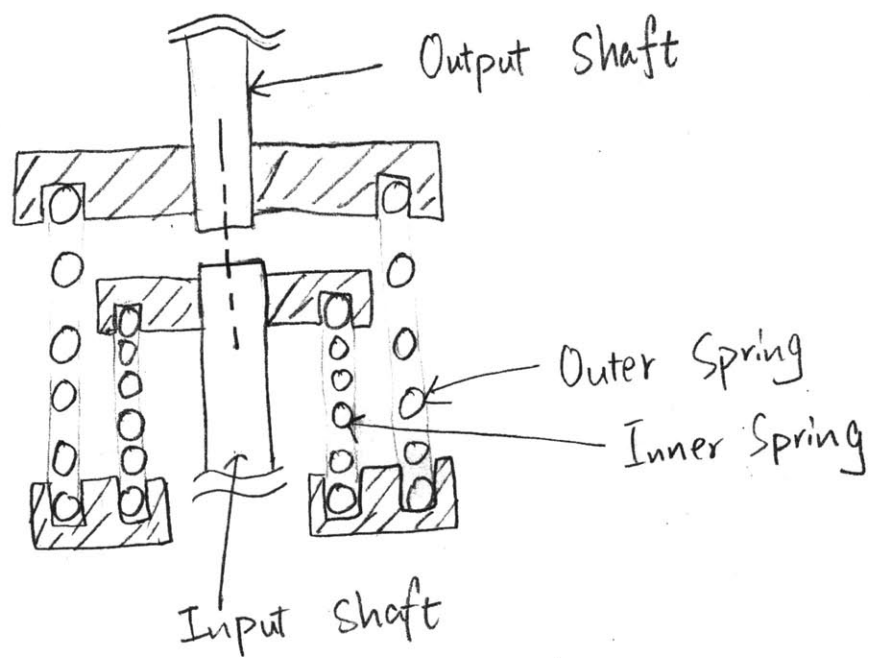
Figure 7-26: Spring packaging design concept 3: springs with different diameters packaged concentrically. This design reduces the the axial length without changing the direction of motion.

Front View   Top View
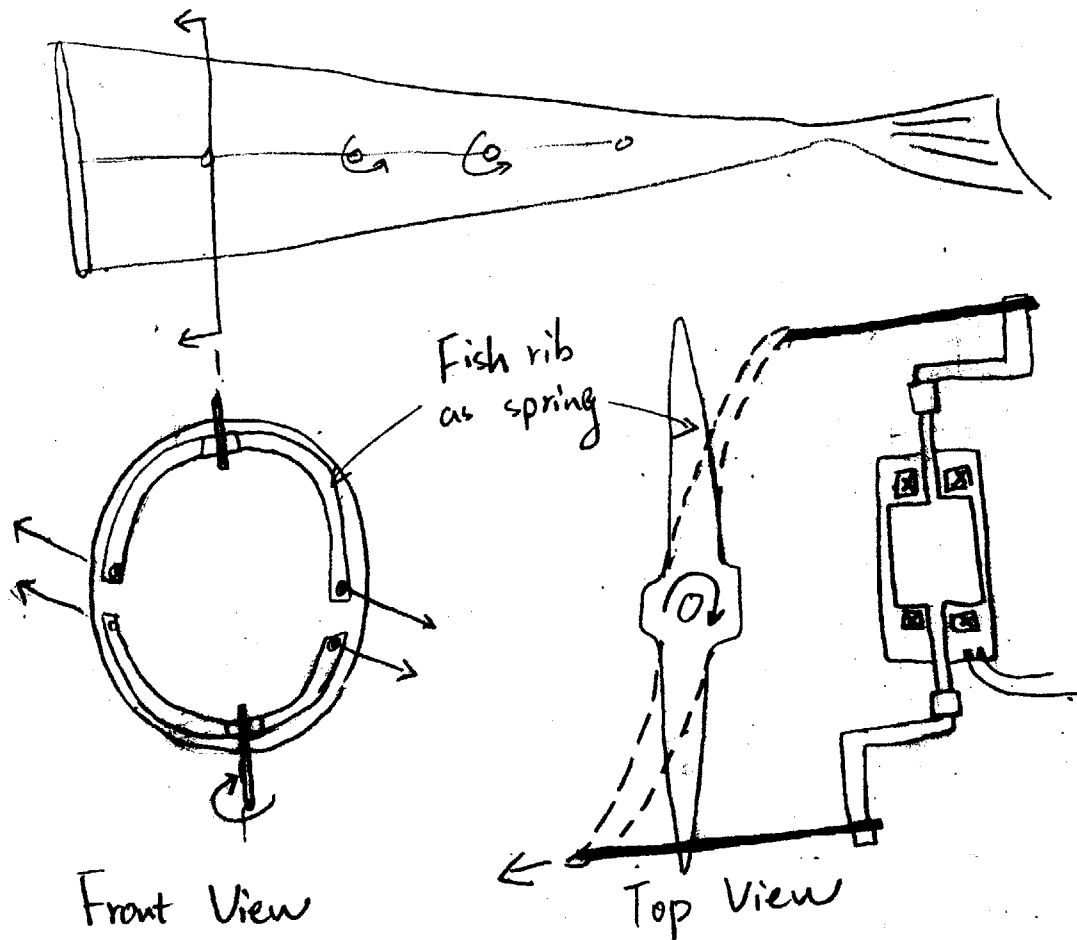
Figure 7-27: A pulse drive fish tail design concept where the spring element is integrated as part of the fish structure. This configuration uses a double-shaft motor with a crank transmission. With the two cranks rotating 180° out of phase, the two ends of the ribs are bent to the opposite direction, applying a net moment on the link.

high energy efficiency.

- Several preliminary latch design ideas and spring packaging ideas are included at the end of this chapter.

7.6 Conclusion of this Thesis and Future Work

In this thesis, we have designed a new pulse drive type series elastic actuator aiming to improve the robotic propulsion efficiency. The idea of the pulse drive is to rapidly store the energy in a intermediate spring by pulse actuating the driver shaft, and then lock the driver shaft and let the spring slowly transfer the energy into the load. Such design is analogous to a mechanical transformer which allows the motor to operate in a high speed and low torque mode. As demonstrated in a stand alone unit, the pulse drive is significantly more efficient than the conventional drive at a power level similar to a robotic fish tail propulsion with the same driver motor. Thus this drive train design has the potential to improve the energy efficiency in actual robotic fish tail propulsion.

One of the most important pieces of work left to be done is to integrate this pulse drive to the robotic fish and test the efficiency in an actual underwater environment. In particular, the crank-shaft transmission design is a good candidate for the latch mechanism because it does not dissipate any additional power, and it can be integrated with the "fish rib as spring" design. However, better trajectories need to be designed to mitigate the loss due to braking current. One possible solution is to start the driver inertia trajectory slightly before the begin latch point, and end the trajectory slightly past the end latch point, as shown in Figure 7-28, so that the current needed to accelerate the inertia at the start and decelerate the inertia in the end may be reduced. Since the angle between the spring and shaft are very small at the new starting and ending points, the torque due to the spring is quite small so that the spring is still considered latched. Currently, Professor Barrett and his team at Olin College already have a complete design of the robotic tuna fish [1] [11]. We suggest that the integration can be divided into four steps. The first step is to design

a motor-spring module that can fit in the robotic tuna tail. This step will involve selecting the proper motor and packing the spring. The second step is to test the propulsion efficiency with only one tail joint in water. The third step is to integrate the motor-spring module to each joint of the fish tail and measure the efficiency. The final step is to evaluate the efficiency of the fish in the open water, and compare the performance to the same fish with the existing drive train design.

We have laid out the theoretical background for the deadzone pulse drive in the thesis, but we haven't constructed any swimming hardware to validate the concept. Thus a good topic for subsequential work of this thesis can be designing and constructing the corresponding hardware. Although these are challenging works, a successful design can lead to applying such drive train designs to many robotic applications, and also inspire related work.

A third direction for future work can be designing the optimal electromechanical actuator for the pulse drive. In this thesis, we have used commercially available motors in our simulation and hardware to achieve high efficiency. However, we believe that those commercially available motors may be not the best option. Most of the commercial motor designs are targeted to maximize the motor quality factor Γ, which is K_t^2/R, per unit volume or just to maximize either the torque density or the power density. As pointed out in Chapter 3, we need to maximize the motor quality factor Γ to the square root of motor inertia $\sqrt{J}$ ratio $\Gamma/\sqrt{J}$ in order to achieve higher pulse drive efficiency. Therefore, future work can involve designing such an optimized actuator specifically for the pulse drive application. In addition, the motor design can also integrate a spring as part of the package to formulate a modular actuator unit. This thesis provides the foundation for such future work.
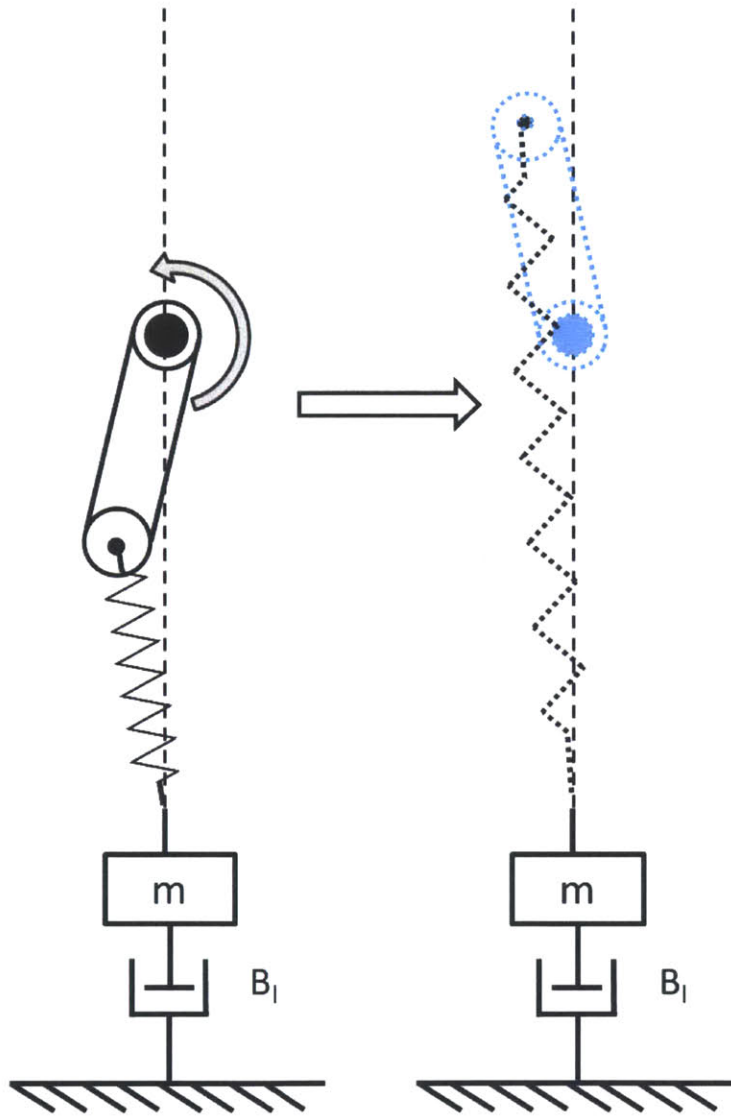
Figure 7-28: Modified beginning and ending points of the pulse drive with the crank-shaft transmission. The starting point is slightly before the lower latch point and the ending point is slightly past the upper latch point, such that the current needed to accelerate the inertia at the start and decelerate the inertia at the end may be reduced.

Appendix A

Tables

No.	D (mm)	L (mm)	K_t (Nm/A)	R (Ω)	J (kgm^2)	P_r (W)	V_r (V)	I_r (A)	$\dot{\theta}_r$ (RPM)
1	8	23	0.00154	3.02	2.5×10^{-9}	2	6	0.691	24000
2	10	25.7	0.00297	3.42	6.9×10^{-9}	8	18	0.558	51400
3	12.7	39.12	0.055	4.22	2.55×10^{-8}	30	48	0.787	76400
4	12.7	50.11	0.00576	1.86	3.60×10^{-8}	50	48	1.37	74500
5	13	23.6	0.00426	5.82	1.65×10^{-8}	6	12	0.646	18300
6	13	35.8	0.00233	0.644	3.25×10^{-8}	12	6	2.28	18400
7	13	39	0.0016	0.348	2.55×10^{-8}	30	12	2.85	64700
8	13	50	0.00144	0.168	3.60×10^{-8}	50	12	4.56	73800
9	16	40.2	0.00529	1.53	7.25×10^{-8}	30	24	1.7	38000
10	16	56	0.00413	0.491	1.07×10^{-7}	60	24	3.52	50900
11	22	44.5	0.00375	0.244	2.39×10^{-7}	40	12	5.36	26900
12	22	62.7	0.00553	0.155	4.09×10^{-7}	100	18	7.64	28700
13	25	83.5	0.00536	0.122	5.45×10^{-7}	250	36	6.16	62300
14	32	60	0.0231	1.83	2.00×10^{-6}	80	36	2.06	13200
15	40	80	0.0396	0.608	5.38×10^{-6}	170	42	4.2	9390
16	45	111.2	0.0165	0.193	1.19×10^{-5}	150	18	10.8	9050
17	45	144	0.0427	0.336	2.09×10^{-5}	250	48	7.94	10000
18	60	177.3	0.147	1.03	8.31×10^{-5}	400	48	5.85	2680

Table A.1: Maxon EC series brushless DC motors specifications. In the table, D represents the motor diameter. L represents the motor length. The subscript r represents for "rated".
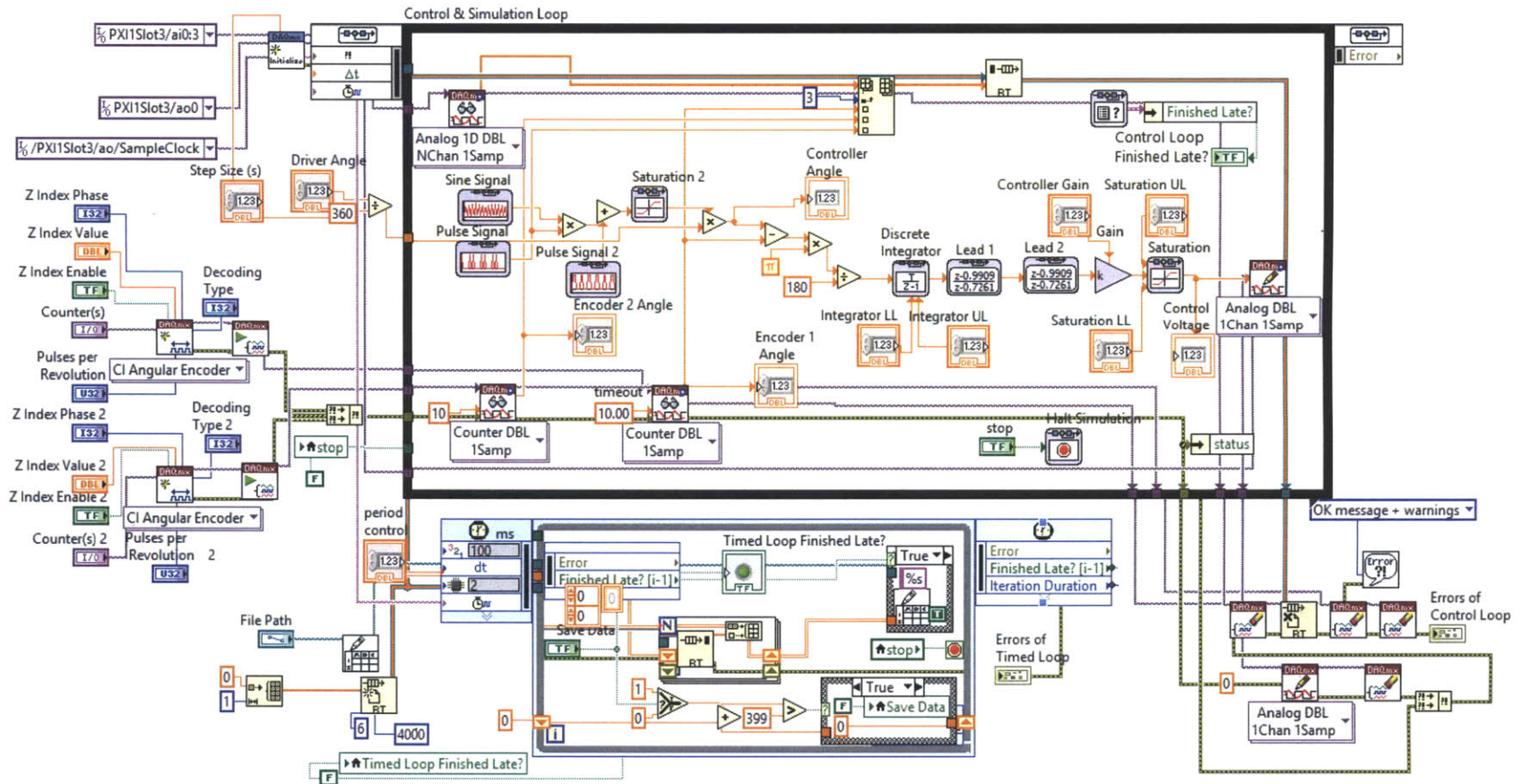
Appendix B

LabView Codes

Figure B-1: LabView VI for the first hardware demonstration. The Upper loop is the control loop and the lower loop is the data saving loop.

Bibliography

[1] Robotuna. http://web.mit.edu/towtank/www-new/Tuna/tuna.html.

[2] Neugart gearbox efficiency, 2011. http://http://neugartusa.com/Service/faq/.

[3] Acxess spring, 2013. http://www.acxesspring.com/spring-calculator.html.

[4] Faulhaber motor, 2013. http://www.faulhaber.com/.

[5] Maxon motor, 2013. http://www.maxonmotorusa.com/maxon/view/catalog/.

[6] Mcmaster-carr, 2013. http://www.mcmaster.com/.

[7] Red lion controls inc., 2013. http://www.redlion.net/Products/DigitalandAnalog/Sensors/ShaftEncoders/ZBGZBHZHG.html.

[8] Transducer techniques, 2013. http://www.transducertechniques.com/ebb-load-cell.aspx.

[9] Kevin B. Albert. Efficient control of series elastic actuators through the exploitation of resonant modes. Master's thesis, Massachusetts Institute of Technology, 2007.

[10] George Keith Bacthelor. *An Introduction to Fluid Dynamics*. Cambridge University Press, 1999.

[11] David S. Barrett. *Propulsive efficiency of a flexible hull underwater vehicle*. PhD thesis, Massachusetts Institute of Technology, 1996.

[12] G. A. Cavagna, N. C. Heglund, and C. R. Taylor. Mechanical work in terrestrial locomotion: two basic mechanisms for minimizing energy expenditure. *American Journal of Physiology - Regulatory, Integrative and Comparative Physiology.*, 233(5):243–261, 1977.

[13] G. J. C. ETTEMA. Mechanical efficiency and efficiency of storage and release of series elastic energy in skeletal muscle during stretch-shorten cycles. *The Journal of Experimental Biology*, 199:1983–1997, 1996.

[14] Fritz Faulhaber. A second look at gearbox efficiencies, 2002. http://www.micromo.com/Data/Sites/1/technical-library-pdf.

[15] Kevin W. Hollander, Robert Ilg, Thomas G. Sugar, and Donald Herring. An efficient robotic tendon for gait assistance. *Journal of Biomechanical Engineering*, 128(5):788–791, 2006.

[16] Benjamin T. Krupp. Design and control of a planar robot to study quadrupedal locomotion. Master's thesis, Massachusetts Institute of Technology, 2000.

[17] Klaus Michaelis, Bernd-Robert Höhn, and Michael Hinterstoier. Influence factors on gearbox power loss. *Industrial Lubrication and Tribology*, 63(1):46–55, 2011.

[18] Society ofAutomotive Engineers. Spring Committe. *Spring Design Manual*. Society of Automotive Engineers, Inc., second edition, 1990.

[19] Daniel Paluska and Hugh Herr. Series elasticity and actuator power output. In *Proceedings of the 2006 IEEE International Conference on Robotics and Automation*, pages 1830–1833, 2006.

[20] G.A. Pratt and M.M. Williamson. Series elastic actuators. In *Proceedings of IEEE/RSJ International Conference on Intelligent Robots and Systems. Human Robot Interaction and Cooperative Robots*, volume 5, pages 399–406, 1995.

[21] Jeery E. Pratt, Benjamin T. Krupp, and Christopher J. Morse. The roboknee: An exoskeleton for enhancing strength and endurance during walking. In *Proceedings of the IEEE International Conference on Robotics and Automation*, volume 3, pages 2430–2435, 2004.

[22] Jerry E. Pratt and Benjamin T. Krupp. Series elastic actuators for legged robots. In *Proceedings of SPIE*, volume 5422, 2004.

[23] David W. Robinson. *Design and Analysis of Series Elasticity in Closed-Loop Actuator Force Control*. PhD thesis, Massachusetts Institute of Technology, 2000.

[24] Umberto Scarfogliero, Cesare Stefanini, and Paolo Dario. A bioinspired concept for high efficiency locomotion in micro robots: the jumping robot grillo. In *Proceedings of the 2006 IEEE International Conference on Robotics and Automation*, pages 4037–4042, 2006.

[25] Dennis P. Townsend. *Dudley's Gear Handbook*. McGRAW-HILL, INC, second edition, 1991.

[26] Matthew M. Williamson. *Robot Arm Control Exploiting Natual Dynamics*. PhD thesis, Massachusetts Institute of Technology, 1999.